2008

A study of jet energy loss in heavy-ion collisions at PHENIX-RHIC, via 2-particle and "2+1" correlations, and future upgrade

Hua Pei
Iowa State University

A study of jet energy loss in heavy-ion collisions at PHENIX-RHIC, via 2-particle and "2+1" correlations, and future upgrade

by

Hua Pei

A dissertation submitted to the graduate faculty

in partial fulfillment of the requirements for the degree of

DOCTOR OF PHILOSOPHY

Major: Nuclear Physics

Program of Study Committee:
Craig Ogilvie, Major Professor
John Hill,
Jianwei Qiu,
James Cochran,
Steven Mickelson

Iowa State University

Ames, Iowa

2008

UMI Number: 3307107

UMI Microform 3307107

ProQuest Information and Learning Company
300 North Zeeb Road
P.O. Box 1346
Ann Arbor, MI 48106-1346

DEDICATION

I would like to dedicate this thesis to my advisor Dr. Ogilvie without whose support I would not have been able to complete this work.

I would like to thank my group member, who gave me many valuable advices during the data analysis.

And great thanks to the whole PHENIX collaboration. I enjoy so much to work in this inspiring big collaboration.

I would also like to thank my friends and family for their loving guidance and emotional assistance during the writing of this work.

TABLE OF CONTENTS

LIST OF FIGURES

CHAPTER 1. Introduction of Jets in Heavy Ion Collisions and Our Basic Methods

1.1 Basic Physics

In this section we review the physical concepts relative to our analysis. We will explain the main physics being studied in our experimental collaboration, and what measurements have been done. Many physics discussions in this chapter come from the PHENIX white paper.(1) A few PHENIX published plots are also quoted in this introduction chapter.

1.1.1 Phase Transition

Lattice QCD has predicted that at a high temperature and energy density, the phase transition will happen (2), so that the quarks and gluons are no longer confined. At such an extreme condition, we cannot treat the medium as the hadron matter as what we did in vacuum. Instead, Shuryak in 1980 (3) proposed the phrase "quark-gluon plasma" (QGP) to describe the de-confined state.

When the energy density " exceeds some typical hadronic value ($\approx$ 1 GeV/fm^3), matter no longer consists of separate hadrons (protons, neutrons, etc.), but as their fundamental constituents, quarks and gluons. Because of the apparent analogy with similar phenomena in atomic physics we may call this phase of matter the QCD (or quark-gluon) plasma.

If hadron gas disappears because of deconfined quarks and gluons above critical temperature and energy density, the perturbative QCD may still not work. This is due to the fact that low momentum transfer between partons approaches the order of T, and the coupling constant approaches the order of unity.

The lattice QCD predicts (4) $\epsilon_C \approx 1$ GeV$/fm^3$ and $T_C \approx 170MeV \sim 10^{12}K$, as we show in Fig. 1.1.

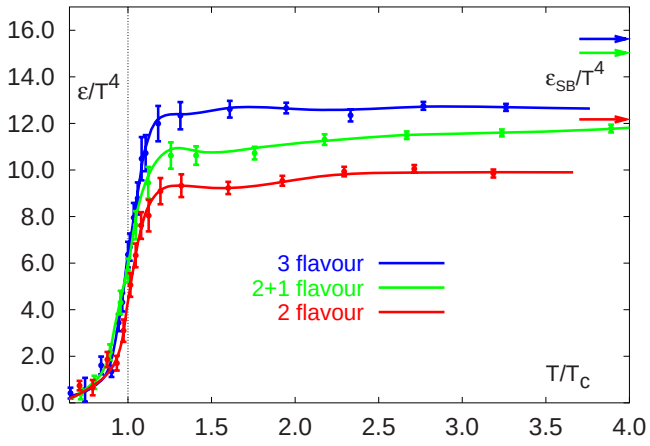

Figure 1.1 Lattice QCD results (4) for the energy density / T^4 as a function of the temperature scaled by the critical temperature T^C. Note the arrows on the right side indicating the values for the Stefan-Boltzmann limit.

This is right where the RHIC physics (Relativistic Heavy-Ion Collider) locates, as in the top-left regime in Fig.1.2. At this region, of high temperature and net baryon density, the form of medium is predicted to be "quark-gluon-plasma", or QGP as usually mentioned. Because of the chiral symmetry restoration at this region, the individual particles in this QGP are now quarks and gluons, as the name of QGP indicates. Thus the dominant interaction within the medium, especially at the early stage, is of the parton-level. All bulk properties of this medium will then be studied by treating this medium as a statistical ensemble of color-neutral partons (q & g) instead of hadrons in vacuum.

Originally at $T \gg T_c$ the quark-gluon plasma was thought to act as a weakly interacting gas of quarks and gluons. But recent experimental result has shown a much stronger interaction among partons in this matter created in heavy-ion collisions at RHIC. This is particularly true in the transition region near T_c, where the fundamental degrees of freedom may be considerably more complex. A few dynamics models have been applied to better describe the degrees of

freedom with this scheme of stronger interaction. We will compare the calculation results of such models on system properties, including temperature, chemical potential and flow velocity, to the actual RHIC measurement.

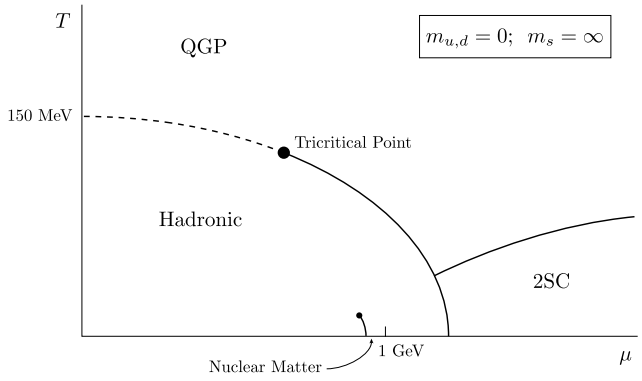

Figure 1.2 Theoretical phase diagram of nuclear matter for two massless quarks as a function of temperature T and baryon chemical potential μ (5).

1.1.2 Spectra and Flow

To study the medium properties in experiments and test the theories above, the first step is to measure the bulk properties. This means we measure the medium using physical observables that cover a wide dynamic range, such as momentum and initial energy/baryon densities. The advantage of measuring bulk properties is that there have been mature theoretical calculations on them. And by looking at a wide dynamical range, we can compare among data from other experiments, together with the theories as the references.

It is believed that the fragmentation of partons into hadrons happen at the late stage of reaction. Thus the hadron spectrum includes both information of original parton distribution function in the nuclei, and the integrated parton-level interaction later with the expanding medium. Since the first parton distribution function can be well measured in p+p where we consider it to be within vacuum, while the medium effects is available mainly in AA collision, we

shall be able to disentangle the medium information from the hadron spectrum by comparing AA collision data to the p+p reference. That's how the single hadron spectrum becomes the first important tool.

Fig.1.3 shows the pT distributions measured at PHENIX-RHIC, for pions, kaons, protons, and their anti-particles, in both central (top panel) and peripheral collisions (bottom panel) (6). In each spectrum, a power-law shape will agree with the direct fragmentation from partons, while the exponential shape indicates a thermal expansion. There are also contributions from the decay of resonances, especially at low pT of pion spectra where a concave shape is visible. At above $pT > 2GeV/c$ in the most central collisions, the production of proton/anti-proton shows an enhancement relative to pions, which is abnormal comparing to the peripheral collisions. This also shows clearly the medium effect. Models such as recombination have been given to explain this enhancement, and they will be checked by more physical observables as in next few sections.

If the identified charged hadron spectra represent the bulk medium effect, a primary assumption is that these hadrons go through the same period of medium thermal expansion and freeze-out at the same stage. Hence the expansion speed $< \beta_T >$ and the temperature at freeze out, T_{fo}, are calculated by a simultaneous fitting (7; 8). This fitting required a few assumptions, including a linear velocity profile and the Woods-Saxon density profile in Eqn.1.1.

$$n_A(r) = \frac{n_0}{1 + exp[(r - R)/d]} \tag{1.1}$$

Being required to reproduce the hadron spectra, this fitting achieves a $< \beta_T > \sim 0.45$ at AGS energies (9; 10), which increases to $< \beta_T > \sim 0.5$ at the SPS (11; 12; 13) and RHIC (7; 14). The fitting result is shown in Fig.1.4. The increase in $< \beta_T >$ as a function of beam energy indicates that the hadron spectra, especially at low pT, is produced by the thermal source. But no stronger conclusion was drawn currently, because $< \beta_T >$ and T_{fo} are strongly anti-correlated and their values depend on fit ranges and treatment of decays.

With the information hadron spectra provides us such as temperature, we need further study their medium geometry dependence. To confirm that RHIC-physics is above the lo-

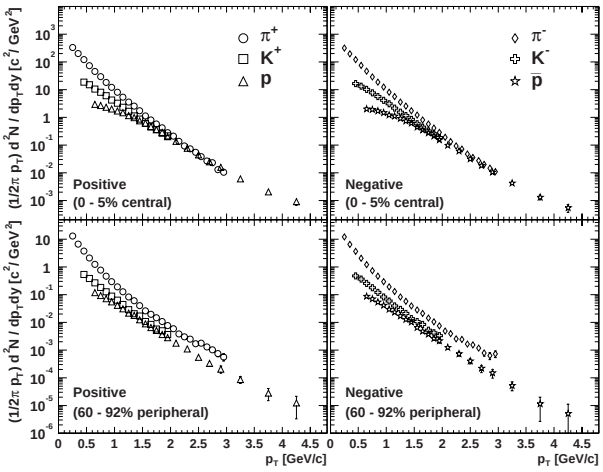

Figure 1.3 Transverse momentum distributions for pions, kaons, protons, and their anti-particles in Au+Au collisions at $\sqrt{s_{NN}}$ =200 GeV
.

cation of the critical point, it is important to find a physical observable that scale with the initial colliding conditions. If measurements of this observable, taking such a "scaling-factor" into consideration, still shows any changes in its trend, we shall have more confidence in the happening of phase transition.

At the beginning of a heavy-ion AA collision, the spatial distribution of the colliding matter resembles an ellipsoid, due to the incomplete overlap of the two colliding nuclei. If strong scattering is sufficient to establish local thermal equilibrium before the spatial anisotropy be erased, then the locally equilibrated hydrodynamics requires the pressure gradient is largest in the shortest direction of the ellipsoid. Hence the spatial anisotropy is converted by the pressure gradient to a momentum anisotropy, which is observable as an asymmetric momentum distribution of the emitted hadrons, called the elliptic flow. Because of this, the observation of any substantial amount of elliptic flow can be taken as evidence that local thermal equilibrium is achieved faster than the time scale by when the spatial anisotropy would be completely erased. Hence the elliptic flow is a self-limiting phenomenon in the thermodynamic limit. Meanwhile, the higher momenta in any direction will bring quicker expansion, quickly reducing the spatial asymmetry. On the other hand, if the strong scattering is absent, the local thermal equilibrium

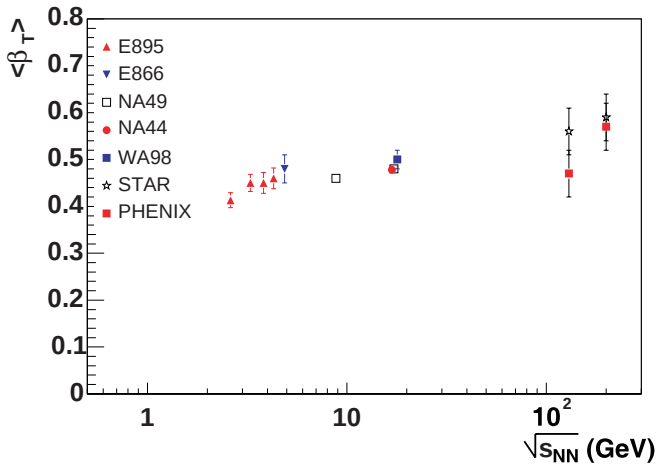

Figure 1.4 Beam-energy dependence of the extracted mean transverse expansion velocity as a function of beam energy from simultaneous fits to spectra of different mass.

will arrive after larger delay, when the initial spatial anisotropy will be reduced, as described by Kolb et al. (15).

To quantify the evolution of the initial spatial anisotropy, we introduced the eccentricity of collision geometry as a function of time. The initial value of eccentricity ϵ can be analytically calculated once the density profile of the nuclei is chosen (typically via a Glauber Monte Carlo (22) and a Woods-Saxon shape in Equ.1.1). It can also be calculated using Monte Carlo techniques, where the discrete positions of those nucleons that participate in the reaction are used to calculate the averages in Eq.1.2.

$$\epsilon = \frac{< y^2 > - < x^2 >}{< y^2 > + < x^2 >} \tag{1.2}$$

The ratio of timing-dependent eccentricity to its original value is calculated through the hydrodynamic evolution. We plot this function in Fig.1.5, also as a function of centrality. We can see that after time delay in the order of t $\sim$ R/c, the magnitude of the eccentricity is significantly reduced, as a function of centrality. Therefore a strong elliptic flow observed will be a good evidence of strong scattering existed at the early stage of medium, before this $\sim$ R/c. Here R is the nuclear radius. Current hydrodynamical calculations require a thermalization

time from 0.6 - 1.0 fm/c to reproduce the magnitude of elliptic flow observed at RHIC, a time delay lower than the R/c above.

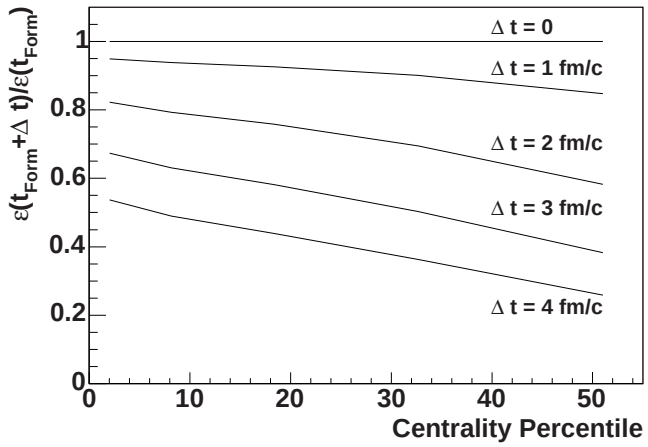

Figure 1.5 The ratio of the eccentricity after a time delay t compared to its value at formation time, as a function of Au+Au collision centrality. The calculations follow the prescription of (15) where the produced particles are allowed to free-stream at first and reach local equilibrium only after some time delay.

We can expand the azimuthal spectra in PHENIX in terms of Fourier coefficients. Because of the collision geometry is symmetric, we neglect the first coefficient v1. Thus the second coefficient v2 becomes the dominant factor in the elliptic flow. And we ignore any higher order coefficients since they are much smaller than v2.

$$\frac{d^2N}{d\phi dp_T} = N_0(1 + 2v_2(p_T)cos(2\phi)) \tag{1.3}$$

As the reduction of eccentricity is a also a function of Au+Au collision centrality in Fig.1.5, we need to study if this hydrodynamic process is uniform in all centralities, i.e., if phase transitions happen all the same. That's when we begin to scale the elliptic flow with initial geometry eccentricity. Obviously, because the eccentricity represents the original non-uniform nucleons distribution in the nucleus, any energy and/or centrality dependence of elliptic flow after this scaling will give information about the critical point, as the phase transition happens above certain energy density. The measurement in Fig.1.6 shows that:

At low pT, v2 approximately scales with the initial eccentricity ϵ of the reaction zone, and increases approximately linearly with pT for low pT. This fact confirms that the initial anisotropy in collision geometry is the main contribution of later elliptic flow. Then the rate of increase of v2(pT)/ϵ as a function of pT is larger at RHIC (16; 17) than at SPS (19; 20), mainly indicating an energy dependence. The slope (dv2/dpT)/ϵ increases from SPS to RHIC by approximately 50%, consistent with high pressure and a shift of their positions in the phase diagram. Note here that the critical point may lead to a reduction in the flow due to a reduction in pressure gradient.

Currently, the hydrodynamical calculations (23) reproduce the data both at RHIC and at CERN SPS within one standard deviation.

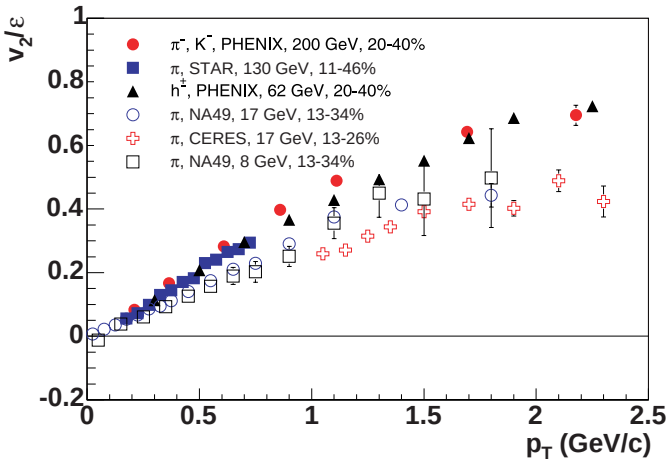

Figure 1.6 v2(pT)/ϵ vs. pT for mid-central collisions at RHIC (filled symbols) and SPS (open symbols). Dividing by eccentricity removes to first order the effect of different centrality selections across the experiments (16; 17; 18; 19; 20).

Further insight into the expansion dynamics can be obtained from the kE_T and quark number dependence of v2(pT) shown in Fig. 1.7 on a broad range of particle categories (24). Here $kE_T = m(\gamma_T - 1) = m_T - m$. We use kE_T other than pT because the former includes relativistic effect and is more robust, and kE_T is better to describe the strong influence of hydrodynamic pressure gradients. Clearly the mass-ordering of v2 is broken in Fig. 1.7, and

even baryon/meson difference is very small if we scale both v2 and kE_T by the number of quarks in each particle. This is interpreted in paper (24) as an indication of the inherent quark-like degrees of freedom in the flowing matter. And the fact that v_2/n_q shows good scaling over the entire range of kE_T/n_q and does not for p_T/n_q, highlights the hydrodynamic mass scaling is preserved over the domain of the linear increase in KET. We are expecting a comparison with an early hydrodynamic model calculation from theorists.

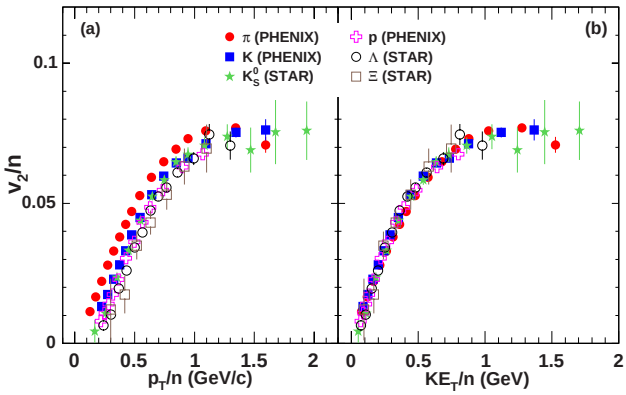

Figure 1.7 The v2 scaling on the quark number n as a function of p_T/n and kE_T/n.

1.2 Jet As A Tool

We have talked about the bulk properties of medium. Now we focus on the high-energy probes such as "hard" particles. We will discuss the mechanism how these "hard-probes" are produced, and why these work as good probes of medium. Then the concept of jet and correlation is introduced, and a summary of previous work on jet correlation at PHENIX is given. Finally in this section I will introduce the core value of my jet correlation work, the controlling of path-length partons travel in the medium. My analysis methods include the "2+1" correlation, reaction-plane dependence, and AA to p+p comparison. Corresponding details of my work are in the next chapters.

1.2.1 Hard Scattering and pQCD

Hard scattering process is defined as scattering of constituents of the nucleons (partons) as described by pQCD (25). For p+p collisions in the RHIC energy range, hard scattering is considered to be the dominant process of "hard" particle production with pT $\geq$ 2 GeV/c at mid-rapidity. Then in AA collisions, because the hard-scattering happens on the earlier stage of colliding, the parton and its following production will interact with the medium. This makes hard-scattering parton a good probe of early stages of medium evolution, before the hadronization.

There have been existing theories to calculate the hard-scattering cross-section in p+p collisions, where it's easier to compare with the experimental data without having to consider the medium effect. The basic idea is to do a two-step calculation, first sum over the parton-parton hard-scattering cross-section, then sum over the processes into one certain hadron using the fragmentation functions of each process.

The overall p+p hard-scattering cross section in "leading logarithm" pQCD is the sum over parton reactions a+b $\rightarrow$ c+d (e.g. g+q $\rightarrow$ g+q) at parton-parton center-of-mass (c.m.) energy $\sqrt{s}$:

$$\frac{d^3\sigma}{dx_1 dx_2 dcos\theta^*} = \frac{1}{s}\sum_{ab} f_a^{x_1} f_b^{x_2} \frac{\pi\alpha_s^2(Q^2)}{2x_1x_2}\sum^{ab}(cos\theta^*) \tag{1.4}$$

In the right-side of this equation:

The $f_a(x1), f_b(x2)$ are parton distribution functions, the differential probabilities for partons a and b to carry momentum fractions x1 and x2 of their respective protons (e.g. u(x2)), and where θ^* is the scattering angle in the parton-parton c.m. system. The parton-parton c.m. energy squared is $\hat{s} = x_1x_2s$, where $\sqrt{s}$ is the c.m. energy of the p+p collision. The parton-parton c.m. system moves with rapidity y = 1/2 ln(x1/x2) in the p+p c.m. system.

Then we calculate how this summed hard-scattering cross-section on the left-side of this equation gives the pT spectrum of outgoing parton c, which then fragments into hadrons, e.g., pions. This is calculated via the fragmentation function $D_c^\pi(z, \mu^2)$, which is the probability for a pion to carry a fraction z = p_π/p_c of the momentum of outgoing parton c. The parameter

μ^2 is an unphysical "factorization" scale introduced to account for collinear singularities in the structure and fragmentation functions (25; 26). In the vacuum $D_c^\pi(z, \mu^2)$ is considered to be colliding system independent, and therefore can be cross-compared between multiple deep-inelastic-scattering experimental data.

One theory model then can calculate the total pion yield by summing over all sub-processes in Equ.1.4 and then each of their $D_c^\pi(z, \mu^2)$.

1.2.2 Mid-Rapidity pT Spectra from p + p Collisions

The high-pT particles production in p+p collision is measured by PHENIX itself as a reference, to compare with theory models, and work as reference of its own AA collision data. According to NLO pQCD, the hard scattering will produce two roughly back-to-back group of particles measurable in mid-rapidity range of center-of-mass frame. Because in PHENIX beam-beam collision, the center-of-mass reference is approximately the same as the lab reference at mid-rapidity, we concentrate in the measurement of the hard probes in the pseudo-rapidity range ~ 0 of PHENIX acceptance. This measurement is done by the central-arm detectors of PHENIX, and the details are in the chapter of detector.

The PHENIX measurement of the invariant cross section for π^0 production in p+p collisions at $\sqrt{s} = 200$ GeV (28) agrees with NLO pQCD predictions over a broad pT range. This comparison is shown in Fig.1.8. The power-law behavior of π^0 spectra with pT $\geq$ 2 GeV/c is another evidence that the high-pT π^0s are typically produced from hard-scattering jets. Hence, we have a good experimental reference for our AA collision data.

1.2.3 Binary Scaling

Now that we have a good reference of hard-scattering in the vacuum, we use this process as a probe in AA collisions. Again we need to find a scaling-factor which scales AA data to p+p data, assuming there is no any medium effects. Since hard scattering is point like, with distance scale 1/pT $\leq$ 0.1 fm, the hard-scattering cross section must be proportional to the relative number of possible point-like encounters, as we compare p+A or A+B collisions to p+p. And any deviation from this scaling is the evidence of medium effects,

For AA collisions, the relative number possible point-like encounters is a monolithic function of the nuclei-nuclei overlap volume. This volume can be calculated as a function of impact parameter b, the distance of centers of two nuclei. We define this nuclear-overlap function as $T_{AB}(b)$, the integral of the product of nuclear thickness over the geometrical overlap region of the two nuclei. Hence, the yield of high-pT π^0s for A+B collisions, with centrality f, can be written as a function of p+p cross-section and average $T_{AB}(b)$ in that centrality bin.

$$\frac{1}{N_{AB}^{Evt}}\frac{d^2N_{AB}^{\pi^0}}{dp_Tdy}\mid_f = < T_{AB} >_f \times \frac{d^2\sigma_{pp}^{\pi^0}}{dp_Tdy} \tag{1.5}$$

In addition, $< T_{AB} >_f$ is defined as:

$$< T_{AB} >_f = \frac{\int_f T_{AB}(b)d^2b}{\int_f(1-e^{-\sigma_{NN}T_{AB}(b)})d^2b} = \frac{< N_{coll} >_f}{\sigma_{NN}} \tag{1.6}$$

Therefore we use the ratio of measured differential yields instead of cross-section to calculate the AA scaling to p+p. Here $< N_{coll} >_f$ is the average relative number of binary nucleon-nucleon inelastic collisions, with nucleon-nucleon cross section σ_{NN}, in the centrality class f. With $< N_{coll} >_f$, the production of hard-probes within certain centrality f are written to be proportional to $< N_{coll} >_f$, also known as the N_{coll} scaling.

Meanwhile, nuclear medium effects, either in the initial or final state, can modify the expected scaling. These modifications can be quantitatively studied by measurement of the nuclear modification factor R_{AB} , which is defined as

$$R_{AB} = \frac{dN^P_{AB}}{< T_{AB} >_f \times d\sigma^P_{NN}} = \frac{dN^P_{AB}}{< N_{coll} >_f \times dN^P_{NN}} \tag{1.7}$$

where dN^P_{AB} is the differential yield of a point-like process P in a A+B collision and dN^P_{NN} is the differential yield of same process P at nucleon-nucleon collisions, or p+p in PHENIX.

If there are no initial or final-state effects in AA collisions, the N_{coll} scaling stands, and the high-pT probe P from hard-scattering process has a $R_{AB} = 1$. Thus the hard photons spectrum in Au+Au collisions at RHIC is an important tool to check this scaling. This is because the photons only interact electromagnetically, and in QCD matter where deconfined partons are dominant this interaction is very tiny. The direct-photon differential yield in AA collision should then reflect only the properties of the initial state, and obey the N_{coll} scaling we mentioned earlier.

The first measurement of direct photon production in Au+Au collisions at RHIC has been reported by the PHENIX collaboration as shown in Fig. 1.9. We see clearly in this plot the hard photons (direct γ) has a $R_{AA} \sim 1$ within errors in a wide pT range, proving the validity of N_{coll} scaling. There are argues about why the R_{AA} goes below 1 at higher pT region. One explanation is that the p+p cross-section cannot fully represent the dN^P_{NN} in Equ.1.7, since we have both protons and neutrons inside Au.

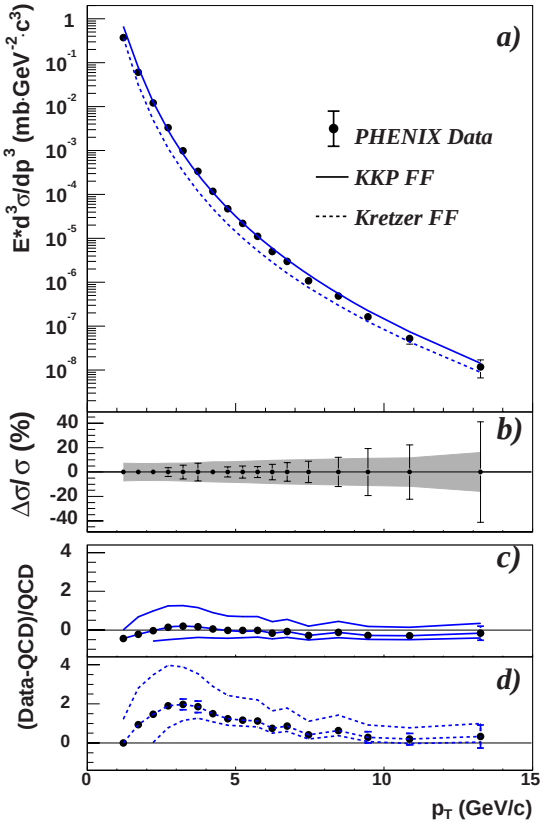

Figure 1.8 PHENIX π^0 invariant cross section at mid-rapidity from p +p collisions at $\sqrt{s} = 200$ GeV, together with NLO pQCD predictions from Vogelsang (29; 30). a) The invariant differential cross section for inclusive π^0 production (points) and the results from NLO pQCD calculations with equal renormalization and factorization scales of pT using the "Kniehl-Kramer-Pötter" (solid line) and "Kretzer" (dashed line) sets of fragmentation functions. b) The relative statistical (points) and point-to-point systematic (band) errors. c,d) The relative difference between the data and the theory using KKP (c) and Kretzer (d) fragmentation functions with scales of pT /2 (lower curve), pT , and 2pT (upper curve). In all figures, the normalization error of 9.6% is not shown (31; 28).

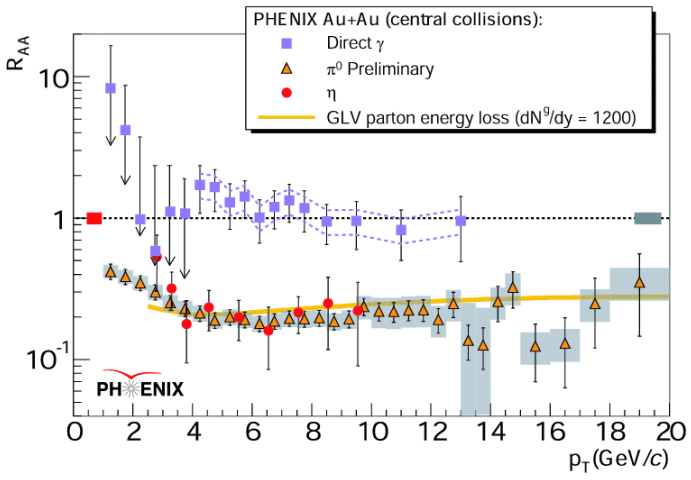

Figure 1.9 R_{AA} of both hard photons (direct γ) and hadrons (π^0 and η) as a function of p_T

1.2.4 Hard Probe And Suppression

In Fig.1.9, the hard photons shows a $R_{AA} \sim 1$, as a proof of the N_{coll} scaling. On the other hand, hadrons with a broad range of masses (π^0 and η) in this plot show a clear suppression of $R_{AA} < 1$. This suppression patterns is a good evidence of high-pT particles be a good probe of the medium.

The suppression is explained by theorists as a result of partons losing energy while propagating through the dense medium created in AA collisions (32; 33; 34; 35; 36; 37; 38; 39; 40). Since partons lose their energy, the average momentum of the fragmentation high-pT hadrons are also reduced, relative to what happens in the vacuum, such as in p+p collisions. More

experimental results of high-pT suppression are published in PHENIX papers based on initial measurements from RHIC Run 2001 (43; 44; 45) and Run 2002 (46; 47; 48; 49).

In detailed observation, the spectra and suppression pattern already ruled out some models. For example, the power-law shape in AA similar to that in p+p at pT $\geq 3GeV/c$ seems to veto a strong modification of the fragmentation function from that of vacuum. Moreover, the results of RHIC year 2003 d+Au measurements (53; 54; 55; 56) showed that the suppression was not due to initial-state effects, such as nucleon condensation.

Therefore, it is originally accepted that this energy loss is predominantly through medium-induced emission of gluon radiation (41; 42). An energetic parton scatters off color charges in the high-parton-density medium and radiates gluon bremsstrahlung. Thus the suppression quantified by R_{AB} provides a direct experimental probe of the density of color charges in the medium (50; 51; 52). Meanwhile, newest measurements and calculations suggest that even elastic scattering can play important role in the energy-loss of high-pT partons. This is done via the re-distribution of energies through elastic scattering inside the medium.

In either way, to re-produce the high-pT probes suppression pattern in the experiments, a theory calculation has to make various assumptions on the medium properties. These assumptions include the thickness of the medium, the energy of the radiating parton, and the coherence in the radiation process itself. Hence by comparing between different theory models and find the one agrees best with experimental data, we have a good opportunity of understanding the medium properties. The PHENIX white paper (1) includes discussion over a few of them (41; 42; 57), comparing their results to the PHENIX R_{AA} as a function of pT.

The size and density are especially important for theory models, as they are not only important medium properties, but also the critical parameter in partons energy-loss models. Any theory model has to carefully treat the time evolution of medium, because the longitudinal expansion increases the medium size and produces a rapid reduction in the energy density as a function of time. Most energy-loss calculations assume that the color charge density decreases as a function of proper time τ as

$\rho(\tau) = \rho_0\tau_0/\tau$

Here τ_0 represents the formation time of the partons from which the medium is composed and ρ_0 the initial number density of those partons. Hence the measured R_{AA} is directly dependent on the product $\rho_0\tau_0$.

The GLV model is one of the first few detailed energy loss model that predicted the flat pT dependence of R_{AA} over the pT range covered by RHIC data, as is reported by PHENIX white paper. This model uses the gluon density as the initial color-charge density as gluons have the largest scattering cross section. GLV model also assumed that the produced partons are spread over a longitudinal spatial width $\delta z = \tau_0 \delta y$. Hence the GLV formulation (40; 58; 59; 60; 52) relates the product $\rho_0\tau_0$ to the initial $\mathrm{d}n_g/\mathrm{dy}$ and obtain $\mathrm{d}n_g/\mathrm{dy} = 1000 \pm 200$ from the PHENIX π^0 R_{AA} values (52).

However, the GLV model calculation is not very sensitive to parton density. This is confirmed when we use different energy density configuration from hydrodynamic calculations (61) to check the result of GLV model. We found it is also true for many other theory models, that the pT dependence of the PHENIX π^0 R_{AA} values is not sufficient to rule out them. Often, a theory model can re-produce the spectra only in specific kinetic region, or it is insensitive to the medium properties we care about.

1.2.5 Introduction of Jet Correlation

We already observe a clear evidence of medium effect in AA collisions at RHIC, via the suppression pattern of the high-pT probes. It is generally accepted (Sec.1.2.4) that the suppression is due to high-momentum partons losing energy as they travel through the dense QGP formed at RHIC, However, we claimed in previous section that the single inclusive high-pT spectra is not sufficient to rule out many theory models on energy-loss mechanisms. On the other hand, from experimental point of view, we cannot exclude the effect of those high-pT particle not directly from hard-scattering process, i.e., recombination, by looking only at the inclusive spectra of high-pT probes. All these are pushing us to apply a new tool, which is more sensitive to the multiple theoretic models from hard-scattering point of view.

A hard-scattered parton in vacuum fragments into multiple particles within a restricted

angular region (i.e. a jet). This is confirmed by experimental data, including PHENIX p+p result (91). And we know many energy-loss models assume that high-pT hadron production is mainly due to hard scattering. Hence, a reasonable way to evaluate these models is to directly observe the angular correlations between hadrons in the jets. The comparison between theory and experimental data in vacuum (p+p in PHENIX case) can confirm the basic credibility of theories. These models shall also re-produce any modification while we compare the p+p data to our own AA data, had they given a correct description of hard-scattering parton energy-loss in medium.

In the reality, the large soft background of a Au+Au collision makes it very hard to reconstruct a full jet event-by-event at RHIC. Instead, both STAR (62; 63) and PHENIX (64; 65) have used a statistical method to study jets, called 2-particle azimuthal-angle correlations. Fig.1.10 shows a typical 2-particle correlation function (66). We will tell later in Sec.1.2.6 how this 2-particle correlation is defined.

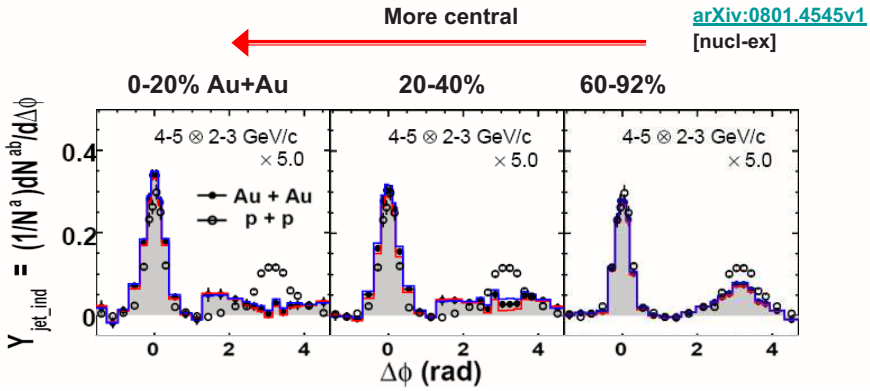

Figure 1.10 A typical plot of correlation functions. Each panel is from a different centrality Au+Au collision, while the same p+p correlation is in all panels as reference.

In Fig.1.10, the jet signals are plotted as a function of the relative azimuthal angle $\Delta\phi$ between pairs of charged particles detected within the PHENIX acceptance in Au+Au collisions from peripheral (60-90%) to central (0-20%), after the subtraction of combinatoric background. The p+p data are also shown in the plot in form of open points as a reference. In each panel, at the region of $|\Delta\phi| \sim 0$ the jet peak is clearly visible, and the region of $|\Delta\phi| \sim \pi$ represents the back-to-back jet if any. The definition of correlation function is in next section, and a detailed explanation of our correlation functions will be in Sec.2.1.

Similar to the case of single hard-pT probes, the hadrons spectrum within the jets will also be modified, if the parton they fragment from loses energy while traveling through dense matter. Because hard-scattering processes are supposed to produce a pair of back-to-back high-momentum partons, this modification shall also be observed via back-to-back jets of hadrons within a restricted angular region. If we compare the most central Au+Au jet signals in Fig.1.10, we do observe strong suppression of jets, especially on the away-side. Detailed

suppression of jets at AA collisions is included in the PHENIX publication (67; 66).

To quantify the suppression of jets, the angular distribution and number of jet fragments are used. Theorists have given quantified predictions on these values by calculation on the coupling of jets to a strongly interacting medium (68; 69; 70; 71; 72; 73; 74; 75). These interaction mechanism are similar to what we used in the single high-pT probes, such as the gluon bremsstrahlung in the medium. However, since the definition of jets required the restrict of angular direction of hadrons, energy-loss of partons doesn't always decrease the jet yield. Quarks from hard scattering processes may recombine with thermal quarks from the dense medium, and form "extra" particles to enhance the jet yields. (68; 69). It is also proposed that the energy deposited in the medium creates a shock wave around the propagating parton, thereby enhance the jet yields by a "sonic boom" in the hydrodynamic fluid. (73; 74; 75).

1.2.6 Definition of Correlation Functions

As we know, inside the center-of-mass reference frame, the fragmentation products from a jet are tightly correlated in ϕ and in η space. If two particles fragment from the same jet, their momentum vectors will have a high probability of being close in $\Delta\phi$ and $\Delta\eta$; if the hadrons fragment from two back-to-back parton jets in a $2\rightarrow2$ hard-scattering, they will have a high probability of being back-to-back in center-of-mass reference frame, or $|\Delta\phi| \sim \pi$ if we project them into the azimuth space. Both back-to-back jets can fall into the PHENIX azimuthal acceptance in its central arms, since that's where PHENIX has its lab reference the same as the center-of-mass reference frame. This is because at mid-rapidity, where the central arms of PHENIX detector are located, the partons will have roughly the same "x" (percentage of longitudinal momentum the parton carries of the nucleon). We will focus on the azimuthal space ($\Delta\phi$) correlation in our analysis below, because of the much less η coverage of PHENIX central arms than their ϕ coverage,

In a full-coverage high-energy experiment and with low soft background, a event-by-event jet reconstruction is feasible. We can define a high-energy seed (or trigger) to tag a jet, then count the relative-low-energy particles around it to measure the jet yield. This method has

been successfully implemented in $e^+ + e^-$ where the multiplicity is low and the jets signal are clean even at relatively low energy (see Fig.1.11). In higher-energy pp collisions this method also works if the jet energies are very high and the detector have a very good acceptance coverage.

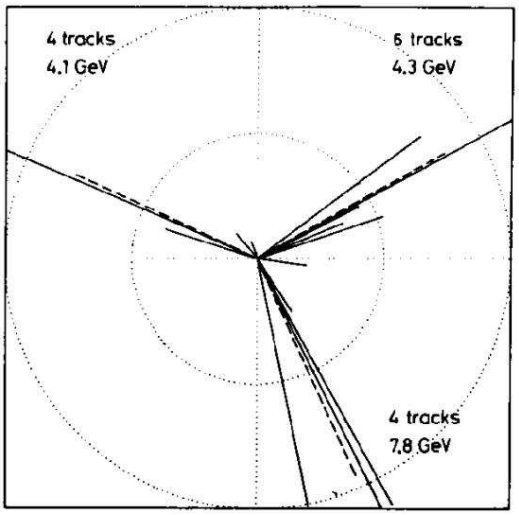

Figure 1.11 One of the earliest three-jet reconstruction plot.

However, in the heavy-ion collision experiment such as PHENIX, neither conditions above are well met, even if both jets fly within the PHENIX central-arm acceptance. In Au+Au events the soft underlying background is very large because there are tens or hundreds of nucleons interacting. Even particles spectrum above $p_T > 2GeV/c$ are not guaranteed to be from hard-scattering process and jets. Meanwhile the PHENIX detector has roughly one third of full coverage, thus an average multiplicity of 10 particles for a given p+p event is incident on PHENIX. Considering the actual detector efficiency, this is a multiplicity too low for event-by-event jet reconstruction (46).

Therefore, we can't derive jet signal event-by-event in PHENIX in either Au+Au or p+p data. Instead, a technique of statistical measurement was applied, first pioneered at the CERN Interacting Storage Ring (ISR) (76). This method is known as two-particle correlations (34). If two particles produced in a given event, one at ϕ_A and η_A, and one at ϕ_B and η_B, the correlation between the two particles is written as

$$\mathrm{C}\left(\Delta\phi,\Delta\eta\right)=\frac{\mathrm{Prob}\left(\phi_{\mathrm{A}},\phi_{\mathrm{B}},\eta_{\mathrm{A}},\eta_{\mathrm{B}}\right)}{\mathrm{Prob}\left(\phi_{\mathrm{A}},\eta_{\mathrm{A}}\right)\mathrm{Prob}\left(\phi_{\mathrm{B}},\eta_{\mathrm{B}}\right)} \tag{1.8}$$

$\mathrm{Prob}(\phi_A,\phi_B,\eta_A,\eta_B)$ is the probability of finding both particles in a given event. $\mathrm{Prob}(\phi_A,\eta_A)$ and $\mathrm{Prob}(\phi_B,\eta_B)$ are the probabilities of finding one single particle at ϕ_A,η_A or ϕ_B,η_B, respectively, in a given event. $\Delta\phi=\phi_A-\phi_B$, and $\Delta\eta=\eta_A-\eta_B$ are the relative azimuth and pseudo-rapidity of the pair.

The reconstruction of jet signals requires the removing of soft background and detector effects such as acceptance. Experimentally one can measure the distributions for each individual particle as a function of azimuthal angle ϕ and pseudo-rapidity η. In a head-to-head collision, when the colliding system is $\phi-$symmetric and after detector effects are taken out, the resulting single particle distributions will be uniform in $\phi-$ space for any specific energy/momentum after averaging over many events. This is confirmed by experimental data, and helps to simplify the function of singles' probability as a function of ϕ. Further measurement shows that at mid-rapidity, the η distribution of single hard-probes is roughly flat in p+p (77), d+Au (55), and Au+Au collisions (49), especially over the relatively small η coverage of PHENIX which is less than +/- 0.35 unit η.

This flattening makes the statistical jet correlation function visible in the relative $\Delta\phi$ or $\Delta\eta$ space. The advantage of the statistical technique is it is independent of the rate of jet production and depends solely on the signal-to-background of the jet over the multiplicity of minimum-bias particle production.

1.2.7 Brief Summary of Prior Jet Correlation Result

To investigate the energy-loss mechanisms of transporting partons, the PHENIX experiment at RHIC measures azimuthally 2-particle jet correlations, within a wide range of centrality in AA (Au+Au and Cu+Cu) collisions and momentum and/or categories (p_T) of hadrons. Different categories of particles are also used to specifically measure certain energy-loss mechanisms.

In the recent PHENIX publications (78; 66), we shown measurements proving that the

angular widths of the same-side jet correlations are the same level (if not narrower) within errors comparing central Au+Au collisions to p+p collisions, in spite of the factor of larger yield of associated hadrons in certain pT ranges. This result is shown in Fig.1.12 as a detailed example, which shows both the centrality and p_T dependence of the same/away -side jet peaks in the Au+Au compared to the jet widths extracted from p+p collisions. Since this Gaussian width is a unique characteristic of the parton fragmentation process, we conclude that high-pT hadrons tagging the near-side jet in Au+Au collisions, is dominantly produced from hard scattering followed by jet fragmentation, as those in p+p.

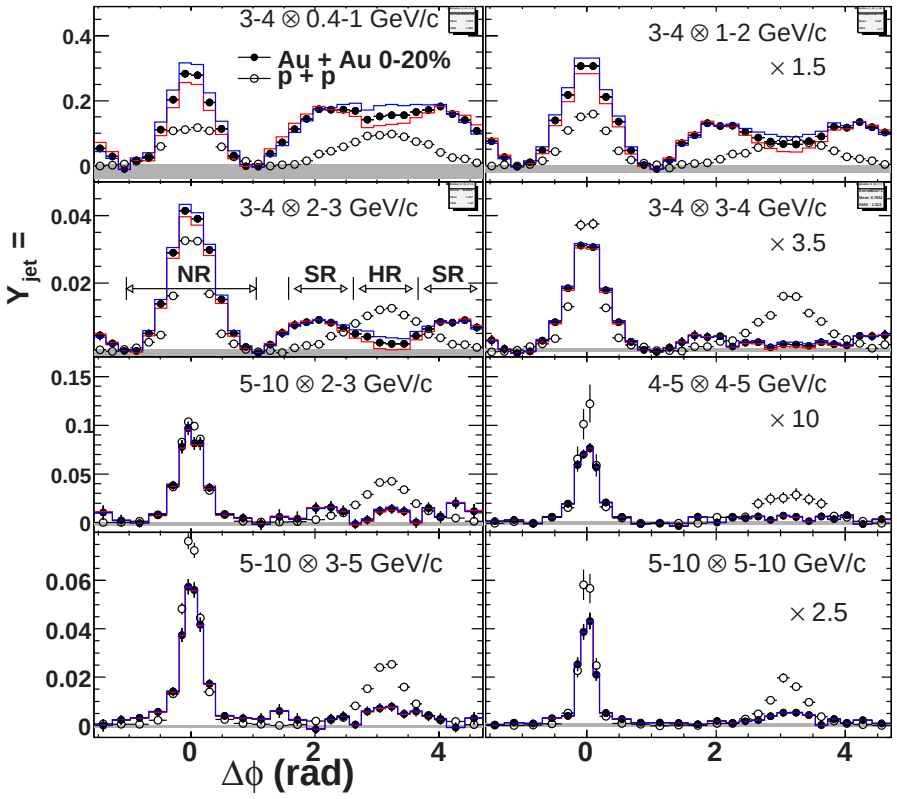

Figure 1.12 Per-trigger yield versus $\Delta\phi$ for various trigger and partner pTs, in p + p and 0-20% Au+Au collisions. The Data in some panels are scaled as indicated. Solid lines (shaded bands) indicate elliptic flow (ZYAM) 2.1.5 uncertainties.

Meanwhile, there exists clear evidence of medium modifications of the fragmentation multiplicity, including the yield of high-pT particles is suppressed in AA collisions. While this suppression confirms what we measured with single high-pT probes, it can also be affected by many factors, such as re-combination or surface-bias. Some factors, such as surface-bias, are not easily observable in single high-pT probes spectrum measurement. In the same Fig.1.12, the jet measurements in PHENIX-RHIC have indicated a modification of di-jet angular correlations that has also been attributed to in-medium parton energy loss. This is evident if we look at the away-side jets $|\Delta\phi| \sim \pi$ in the same figure. The reduction of away-side jet yield relative to p+p is evident. In the paper (66) publishing this plot, this reduction was further studied. We can see in this Fig.1.12, concepts such as head-region **HR** and shoulder-region

SR are introduced to divide the away-side region for fine comparison.

1.2.8 Path Length Control in Medium

The existing theory models have their calculation based on parameters of the density and path-length of medium is traveled by the parton. Hence, how to best disentangle these two effects is an open question and work proceeds on multiple fronts: studying energy-loss versus reaction plane, centrality, and for different size colliding systems. Part of the difficulty is the strong energy-loss means that partons, which survive to produce high$-p_T$ hadrons, come from hard-collisions that occur predominantly near the surface of the dense matter, i.e., surface-bias. While we claimed the single high-pT spectra from existing models such as GLV may not be sensitive to such a surface-bias, it's not the same case while processing jets. The jet mechanisms currently being discussed, including re-combination and "shock-wave", seriously dependent on the path-length traveled by partons. Therefore, it's important if we can find one experimental method to shift, even statistically, the collision position to the center of medium, so that the partons will have to travel more length in the hot-and-dense matter. This will do great help to remove the concern of surface bias.

My analysis work in this thesis will concentrate on this path-length control. I will introduce in following sections the analysis methods I used. The actual making of correlation function, detector configuration, and cuts will be included in the following chapters of my thesis. Then it will be the chapter of analysis result, followed by further scope.

1.2.8.1 Definition of 2+1 Correlation

One possible method is to tag events that have two back-to-back jets. On average these two jets/partons will have a higher possibility of traveling through similar lengths of dense matter and lost similar amounts of energy. This statistically shifts the surface bias more towards the center of this collision. We call this method "2+1" correlation, as we introduced later in this chapter.

The idea of "2+1" correlation comes from a concern of surface-bias of single high$-p_T$

particles measurement. As we have measured in Sec.1.2.3, the single particle spectrum of central AA collisions is already suppressed compared to that of p+p, if we normalized the former by N_{coll}. However, this single fact can't tell us all the details of the properties of this hot-dense matter, because the energy loss depends on both the density of the medium and the path-length that is traveled by the parton. This seriously affects our jet analysis, where we select a high$-p_T$ particle as the trigger of correlation. If this trigger is surface-biased, the shape of jets, especially that of near-side jet, may not tell us the properties of medium as expected.

Thus it's important to change even statistically the surface-bias from our correlation function. That's how we introduce this "2+1 particle" correlation function in addition to the previously mentioned "2-particle" correlation. Here "1" means another high$-p_T$ particle in the same event of trigger, but in the back-to-back hemisphere of the trigger particles. We then call this 2nd high$-p_T$ back-to-back particle the "conditional" particle in our analysis since it changes the condition of surface-bias. The idea of this extra particle is by a event selection:

We already know 2 back-to-back partons in a hard-scattering event produce jets. For both partons to survive the medium and produce high-pT hadrons, they must travel comparable path-lengths through the dense Quark Matter (possibly the "QGP"). The events excluded additionally by the "2+1" correlation are those that hard-scattering locations nearby the surface of medium. They are likely to have one jet traveling a short distance in the medium and presenting a high-pT trigger, but won't give the presence of the "conditional" high-pT hadron on the away-side because the back-to-back jet is most likely to be absorbed in the medium. These events would have been included in our "normal" 2-particle correlation analysis, because they do provide a high-pT trigger at near-side. Since we remove them, we shift the average location of hard scattering towards the center of the medium, statistically. This is plotted in a cartoon in Fig.1.13.

By comparing the jet shape of "2+1" correlation function to those usual 2$-$particle correlation function, we shall have a better understanding of how jets are affected by the medium and thus the properties of this hot-dense medium.

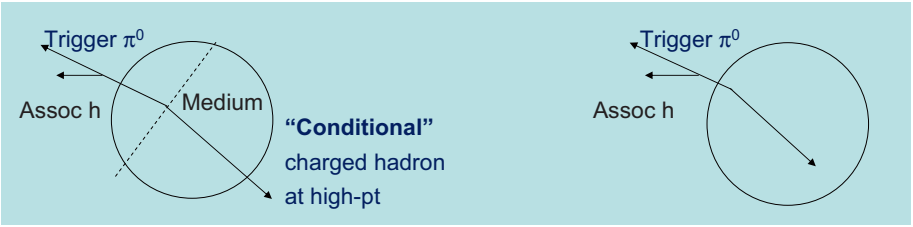

Figure 1.13 A cartoon of how 2+1 correlation works. On the left side, the existing of "conditional" particle shifts the hard scattering to center of medium, and both partons survive the medium and produce high-pT particles. On the right side, it shows the possibility that a normal 2-particle correlation has its away–side parton absorbed in the medium and no high-pT particle created on the away side.

1.2.8.2 Definition of Reaction Plane

Another path-length controlling method in my thesis work is through the parton (trigger) angle relative to the reaction plane in the azimuthal space. Here the event-by-event reaction plane is defined by z-axis and the line connecting centers of two nucleus. This plane is measured in PHENIX by a set of detectors, and we will give details on that in reaction plane detector section 3.2.5.

As we see in the Fig.1.14, the partons and their successive jets will travel different path-lengths when they are of different angle $\Delta\Psi$ relative to the reaction plane. Thus by measuring jets at different $\Delta\Psi$ region, technically by tagging triggers, we can compare the jets traveling different amount of dense medium, and have a better understanding of medium properties. Again, because of the existence of surface bias, the distribution of hard-scattering locations is

not uniform, so this reaction plane dependence is also a statistical effect.

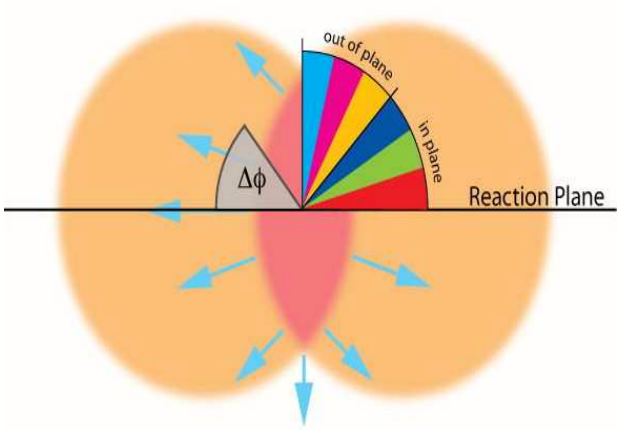

Figure 1.14 A cartoon of how the triggers are divided into different azimuthal bins with their angles relative to the reaction-plane.

CHAPTER 2. Experimental Details of Jets Measurement in Heavy Ion Collisions

This chapter tells the details of our experimental procedure in measuring jets through the construction of correlation functions. First, the definition of two-particle correlation function is given. Then we introduce the practical method in constructing these functions. Later the different sources of physical correlations in hadronic and heavy-ion collisions, namely elliptical flow and di-jet correlations are discussed. The chapter ends with a discussion of fundamental relationships that are used to quantify these sources of correlations from the functions.

2.1 Construction of the Correlation Function

We select high$-p_T$ trigger π^0 and select charged particles as the associated. Then we plot the yield of associated charged hadrons per trigger for each data set. All our yield functions are generated on a pair-by-pair basis and normalized to be per-trigger yield. Thus correlation functions on different physics observables ($|\Delta\phi|$, x_E, $p_{Tout}^{Near-side}$) share the same normalization factors if they are from the same centrality/p_T bins. The basis of our correlation work, such as normalization and flow, comes from $|\Delta\phi|$ function however.

2.1.1 Mixing Event Technology

As we introduced before, the PHENIX detector does not have a full azimuthal coverage in central arms, so the raw single particle distributions are not uniform in azimuth. These must be corrected by the shape of the PHENIX acceptance, so as to further correct the joint pair distribution as well, since the acceptance is folded into the raw spectrum. Experimentally, one defines the correlation by

$$\mathrm{C}\left(\Delta\phi,\Delta\eta\right)=\frac{\frac{\mathrm{d}^2\mathrm{N}_{\mathrm{pair}}^{\mathrm{real}}}{\mathrm{d}\Delta\phi\mathrm{d}\Delta\eta}}{\frac{\mathrm{d}^2\mathrm{N}_{\mathrm{pair}}^{\mathrm{mix}}}{\mathrm{d}\Delta\phi\mathrm{d}\Delta\eta}} \tag{2.1}$$

The numerator of Eqn. 2.1 is the raw joint pair distribution we measure in the detector. The denominator is the raw mixed pair distribution representing the acceptance effect, where each of the particles from the pair is taken from different events (see Sec.2.1.1). Ideally the mixed pair distribution does not contain physical correlations, and only carries information about the acceptance and the efficiency of the singles. Constructing the correlation function in this way removes the pair acceptance from the raw pair distribution. We also apply same pair-cuts to real and mixed correlations to remove possible ghost tracks, when trigger and associated are of the same category particle. Therefore, the correlation function from Eqn.2.1 is proportional real pair distribution.

$$\mathrm{C}\left(\Delta\phi,\Delta\eta\right)\propto\frac{\mathrm{dN}_{\mathrm{pair}}}{\mathrm{d}\Delta\phi\mathrm{d}\Delta\eta} \tag{2.2}$$

In correlation analyses, a range of momentum is defined for each of the two particles of a pair. Any combination of ranges is possible since the pair distribution is symmetric with respect to the particles. **Fixed** correlations are defined as both trigger and associated particle having the same p_T range. **Assorted** correlations are defined as both particles having different p_T ranges, where typically we have one ***trigger*** particle which is the particle in the highest momentum range and one ***associated*** particle which is the particle in those lower momentum ranges.

Events will then be further subdivided into centrality bins and collision z-vertex bins. So one event that has at least one pair of particles, one in the trigger and one in the associated bin, is selected into its specific centrality and collision z-vertex bin. The real joint pair distribution of that bin-combination is then filled with all available pairs of particles in that event. That distribution is the numerator in Eqn.2.1. And the number of triggers in this event is recorded for later normalization. In this way we do not directly reconstruct jets but only look for the statistical correlation of the particles produced by jets.

2.1.1.1 Selecting Events To Be Mixed

The purpose of the mixed event distribution is to completely remove all physical sources of correlation so that the only source of mixing-event correlation functions is the pair acceptance and efficiency, i.e., only detector effects. It can be then used to correct our real-event foreground correlation function.

The technique that is employed is known as the "rolling-buffer" technique. A list of N trigger events of our physical interest (in our case, if one event contains at least one trigger π^0 or a π^0 plus a conditional hadron) are kept in a "trigger-event" buffer. A list of general events sample, without bias over our physics interest (in our case, no trigger and/or conditional particle requirement), are kept in a "associated-event" buffer. Each time one trigger event enters the bottom of buffer, its trigger(s) will correlate with all "similar" events from the associated buffer. When either the trigger or associated buffer is full, the top (earliest) event is thrown out of the buffer. The word "similar" is explained below.

After this, the head event in both buffers are removed and the buffers are shifted to make room for the next event. This is the general method, but there are variations. For instance, the number of events in the buffer is not fixed and is typically guided by requiring a factor of 10 more statistic in the mixed distribution than the real distribution. The number of particles that are correlated from each mixed event is not fixed and can varied as well, although in our case we will use all particles in the desired p_T bins. This will decrease our statistical errors from mixing-event as much as possible.

The one vital assumption that is made in Eqn.2.2 to assure the events to mixed are "similar" is that the two-particle efficiency factorizes into the product of the two single particle efficiencies. That typically means that if a pair-cut is applied to real pairs, i.e. detector resolution cuts, the same cut must be applied on the mixed pairs. Also, to remove event-dependent geometry effect as much as possible, the mixed pair must come from two events of similar collision geometry, i.e., similar centrality and collision-vertex, so as to avoid the change of z-vertex dependent acceptance by magnetic field and the multiplicity dependent single particle tracking efficiency.

In Au+Au, we have all events divided into 3 centrality bins: 0-20%, 20-40%, 40-92%.

In Cu+Cu, we have all events divided into 6 centrality bins: 0-10%, 10-20%, 20-30%, 30-40%, 40-50%, 50-92%. On the other hand, in p+p we have only one centrality bin.

In either Cu+Cu or p+p we have 6 z-vertex bins between -30 to 30cm, 10cm each. Events only mix within same centrality and collision z-vertex bin. Since we are running analysis jobs via analysis taxi4.4.2, the associated hadrons are from the minbias trigger nanodst events of the same run, and most nearby run-segments, thus timing period, to those of trigger events. Therefore, this rolling-buffer technique ensures only events within closing timing frame can mix. The mixing-event correlation histograms are then be used to correct the acceptance of the real-event one, of the same trigger and associate p_T bin. Since we are analyzing per-trigger yield, we don't need to correct single trigger π^0 efficiency here.

Regardless of the mixing method, it is important that the associate events that are used to mix with our events of physical interest must be from a pure minimum bias sample, otherwise acceptance effects can bias your sample. For example, if you mix between trigger events themselves, and your trigger selections are biased because of the detector acceptance, you can decrease the jet yield in the peak region while increasing yield in other region of correlation functions. It's called a "space bias" then. Here, a minimum bias event is defined as being selected by detector components other than the central arms, so that it won't have the same detector bias the trigger events have. In our case, we use BBC detector, which located at $3.1< \eta <4.0$, as our minbias event selector. On the other hand, if we are selecting our trigger events and associate events from two different sets of detectors, it's possible that they will be from different time periods and thus not being measured by the same detector geometries. This will produce a "time bias" on the other hand.

In our analysis of next chapters, we will show both results and use the difference of them to estimate one source of our systematic errors.

2.1.2 Definition of Condition

When we require a "conditional" charged hadron we select the events with at least one back-to-back ($\pi/2 < |\Delta\phi| < \pi$) hadron with π^0 trigger. We use several p_T ranges for this hadron: the p_T to be smaller than 10GeV while larger than 1, 2, 3, 4, 5 GeV, respectively. When we are filling foreground real-event correlation functions, we require this conditional particle won't be used as an associate particle.

It's also important that when doing event mixing, only those π^0 with a good "conditional" particle go into event pool. Thus we keep the same requirements on "real" and "mixing" triggers, so as to keep both events in the same category of physical interest.

2.1.3 Normalization

The correct normalization of the correlation function is necessary in order to extract the correct yield of pairs. A common way at RHIC is to report per trigger yields, where the correlation function is divided by the number of triggers and an appropriate normalization $\mathcal{N}$ is used. This normalization $\mathcal{N}$ satisfies (where the subscript "pair" from is dropped now on)

$$\frac{1}{N_{trig}}\frac{d^2N}{d\Delta\phi d\Delta\eta} = \mathcal{N}\mathrm{C}\left(\Delta\phi, \Delta\eta\right) \tag{2.3}$$

The normalization constant has been derived in (79). After η integration we obtain

$$\frac{1}{N_{trig}}\frac{dN}{d\Delta\phi} = \frac{R_{\Delta\eta}}{N_{trig}}\frac{\int d\Delta\phi \, \frac{dN^{mix}}{d\Delta\phi}}{\Omega_{\Delta\phi}}\frac{\frac{dN^{real}}{d\Delta\phi}}{\frac{dN^{mix}}{d\Delta\phi}} \tag{2.4}$$

Here $R_{\Delta\eta}$ is the correction for the jet yield to an eta range of ± 1 unit, including also the single associated particle efficiency ϵ. This is easily done in p+p and d+Au collisions since the jet behaves in a well known way, but not the case in Au+Au collisions because the jet on the near side has a ridge structure in η (80). Since I am mostly interested in comparing AA to p+p correlation functions and see how it evolves according to centrality and p_T, I don't need to derive the absolute yield of AA or p+p separately. Thus I don't apply $R_{\Delta\eta}$ in my analysis. $\Omega_{\Delta\phi}$ is the azimuthal range of the correlation function which is either π or 2π depending on

if the full range is folded. In my analysis, I will constantly use π since the basic correlation functions are written in form of $|\Delta\phi|$.

2.1.4 Sources of Correlations

Physical correlations in position and momentum space can occur from many sources. They include Hannbury-Brown-Twiss (HBT) correlations and decay, which is due to the wavefunction overlap of particles, and being strongest at low transverse momentum near a few hundred MeV where the relative momentum of the particles is low. Decay from both long and short lived particles introduces correlations as well. Since our analysis focused at $p_T > 1$ GeV/c the contribution from decays is expected to be negligible.

2.1.4.1 v_2

In heavy-ion collisions such as Au+Au, a source of physical correlations arises due to flow. When two spherical nuclei undergo a non-central collision, the resulting overlap is an almond shape (see Fig. 2.2), and a reaction (event) plane is formed by the beam direction and the impact parameter direction. A cartoon of reaction plane defined by beam-axis and collision geometry is shown in Fig.2.1

A pressure exists within this almond and a larger pressure gradient is present along the short side of the almond, in plane, as compared to the long side of the almond, out of plane. This produces a scenario called "flow", where the momentum distribution is not ϕ symmetric but a function with respect to the reaction plane 1.2.8.2. If we expand the azimuthal distribution of single particles as a Fourier series, as in 2.5:

$$\frac{dN}{d(\phi - \Psi)} = \frac{N_0}{2\pi}\left(1 + v_1\cos(\phi - \Psi) + 2v_2\cos\left(2(\phi - \Psi)\right) + \ldots\right) \tag{2.5}$$

where the v_n coefficient are the flow coefficients. While the odd coefficients go to zero at midrapidity because of the left/right symmetry. The dominant terms in Equation. 2.5 are the even coefficients. Since the first even coefficient is a constant, we will focus on the second one, the v_2 term, and it is known as elliptic flow.

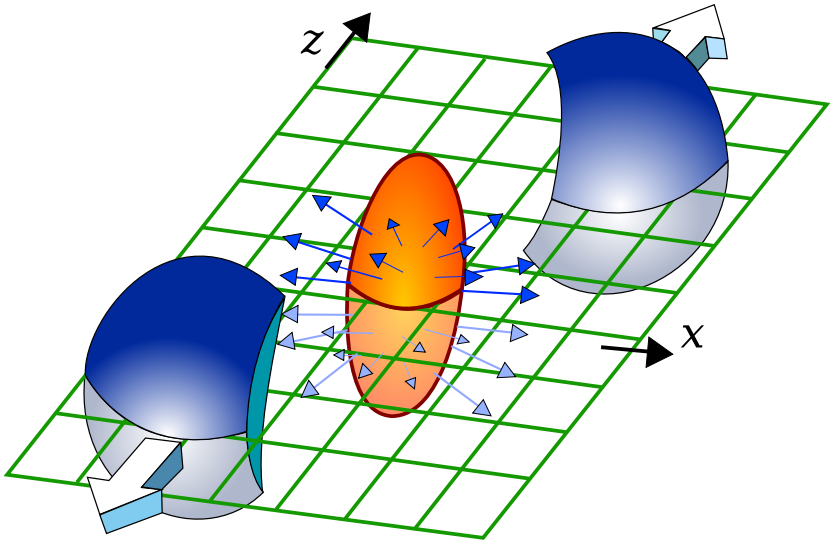

Figure 2.1 In this cartoon we show the definition of reaction plane. This plane is defined by two lines, the beam axis, and the line between the centers of two nuclei in collision.

Since each of the particles in the event can be correlated with the reaction plane, they will be correlated with one another in a very straightforward manner. This correlation can be seen by writing the definition of the two-particle correlation

$$\frac{dN}{d\Delta\phi} = \int_0^{2\pi}\int_0^{2\pi} d\phi_A d\phi_B \, \frac{dN}{d\phi_A}\frac{dN}{d\phi_B}\delta\left(\Delta\phi - \phi_A - \phi_B\right) \tag{2.6}$$

We can substitute Eqn. 2.5 and follow the mathematics.

$$\begin{aligned}\frac{dN}{d\Delta\phi} &= \int_0^{2\pi}\int_0^{2\pi} d\phi_A d\phi_B \frac{N_A}{2\pi}\left(1 + 2v_2^A\cos\left(2(\phi_A - \Psi)\right)\right) \\ &\quad \frac{N_B}{2\pi}\left(1 + 2v_2^B\cos\left(2(\phi_B - \Psi)\right)\right)\delta\left(\Delta\phi - \phi_A - \phi_B\right) \qquad (2.7)\\ &= \frac{N_A N_B}{(2\pi)^2}\int_0^{2\pi} d\phi_A[1 + 2v_2^A\cos(2(\phi_A - \Psi)) + 2v_2^B\cos(2(\phi_A - \Delta\phi - \Psi)) + \\ &\quad 4v_2^A v_2^B\cos\left(2(\phi_A - \Psi)\right)\cos\left(2(\phi_A - \Delta\phi - \Psi)\right)] \qquad (2.8)\\ &= \frac{N_A N_B}{(2\pi)^2}[2\pi + 4v_2^A v_2^B\int_0^{2\pi} d\phi_A\ (\cos^2(2(\phi_A - \Psi))\cos(2\Delta\phi) +\end{aligned}$$

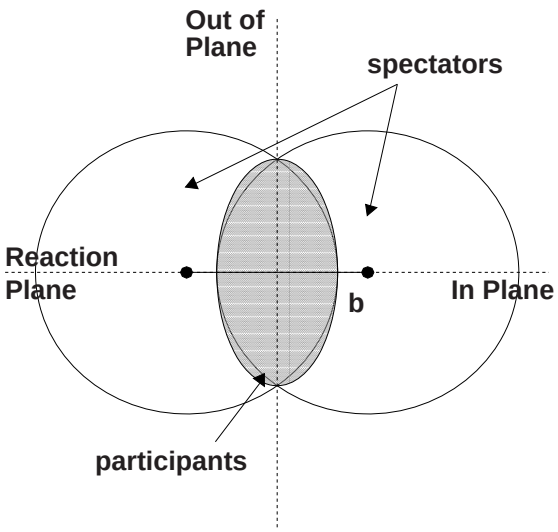

Figure 2.2 Schematic diagram of interacting nuclei. The overlap (shaded grey) region is where the nucleons which participate in the interaction are located. The remaining nucleons are labeled as spectators. The distance between the two nuclear centers is labeled, b, the impact parameter. The overlap region is typically denoted by a function $T_{AA}(b)$.

$$\cos(2(\phi_A - \Psi))\sin(2(\phi_A - \Psi))\sin(2\Delta\phi))] \tag{2.9}$$

$$= \frac{N_A N_B}{2\pi}\left(1 + 2v_2^A v_2^B \cos(2\Delta\phi)\right) \tag{2.10}$$

We can see the pair distribution has the same correlation shape as that of the single particle, but with a new strength that is the product of the v_2s of the trigger and associated particles. This shape can exist wherever we have a combination of trigger and associated p_T bins, and it will peak at both $\Delta\phi = 0$ and π, a feature similar to the jet and di-jet correlations.

The flow v_2 in Au+Au and Cu+Cu we applied here came from (81). In each centrality/p_T (trigger-associate-conditional) bin, we plot the p_T spectrum of trigger/associate, and derive the mean p_Ts. We then derive the specific v_2 for the triggers and associates by interpolating within the measured results as a function of p_T and centrality in Fig.2.3.

Because we are mixing with minbias events from the same centrality bin and neighboring time frame, the v_2 therefore has the correct centrality weighting for the sub-sample of min-bias

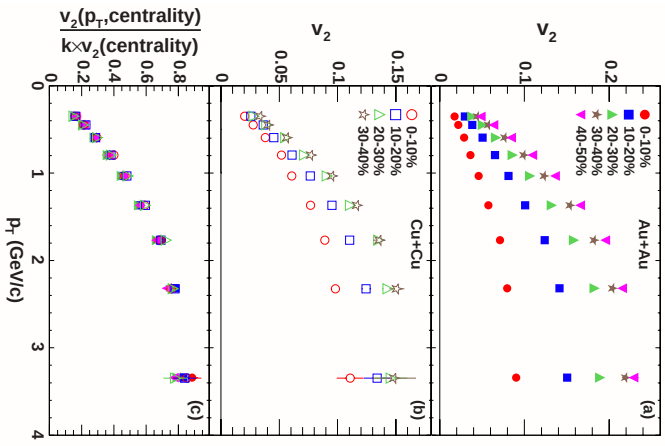

Figure 2.3 The published PHENIX measurement of v_2 in Au+Au and Cu+Cu as a function of centrality and pT.

events selected by requiring a π^0 and a conditional hadron. These requirements tend to make the reactions more central. Note Note we assume the v_2 for trigger π^0 has the same functions of p_T and centrality as those of associated charges. We also assume the v_2 is flat beyond highest v2 measurable p_T region in each centrality bin, and use the v_2 of highest available p_T bin for even higher p_T particles in each centrality bin. In ppg062, the $1-\sigma$ errors of v_2 include both statistics and systematic ones. Plus, there is a systematic error due to systematic error on v_2. The reaction plane correction uncertainty dominates this systematic error and is 10% for Cu+Cu. Operationally we calculate our own $1-\sigma$ error of v_2 as the quadratic sum of errors from ppg062 and this 10% error from reaction plane. We then analyze the data with the nominal v_2 and compare with v_2 larger and smaller by $1-\sigma$ cases. This comparison leads to different yields which are propagated to the extracted yields.

Now that we have a background source, our correlation function will be written into two items, the jets with the accompanying underlying event. In p+p and d+Au collisions this background is *assumed* to be isotropic because of the small size of collision geometry and ignorable flow. In the case of A+A collisions, the elliptic flow introduces a harmonic $\cos(2\Delta\phi)$ shape on the background, and the correlation function, or more precisely the pair per trigger distribution, has to be written as

$$\frac{1}{N_{trig}}\frac{dN}{d\Delta\phi} = B(1 + 2v_2^{trig}v_2^{assoc}\cos(2\Delta\phi)) + \mathcal{J}(\Delta\phi) \tag{2.11}$$

where B is the underlying isotropic background, v_2^{trig} and v_2^{assoc} are the trigger and associated particle's elliptical flow, and $\mathcal{J}(\Delta\phi)$ is the shape of the jet plus di-jet distribution. Our next job will be to subtract the flow background from the raw per-trigger yield, which is already corrected by the acceptance and single particle efficiency.

2.1.4.2 Reaction Plane Dependence of v_2

When we do reaction-plane dependent analysis of jet correlation, the trigger particles are selected with specific relative angle to the reaction plane. In this case, the $\Delta\phi$ of trigger to reaction-plane are biased, and the correspondent v_2 are not the inclusive value any more. Instead, we force the trigger to be correlated (in-plane) or anti-correlated (out-plane) to the reaction plane. And the v_2 of this specific trigger selection can be calculated using 3 parameters: center angle of trigger selection ϕ_S, azimuthal width of trigger selection c, and reaction-plane resolution. The details of this calculation was summarized by Shinichi Esumi in (82)

2.1.5 ZYAM method

ZYAM is a method named from Zero-Yield-At-Minimum (ZYAM) (83). We first correct the raw correlation function (or more precisely, the per-trigger yield) by acceptance and single-particle efficiency, then we shift the v_2 flow background curve from below and let it "touch" the raw correlation function, then subtract the flow contribution from the raw correlation function to derive the jet shape and yield. This is based on the assumption that both near and away-side jet yield, peaking at $\Delta\phi = 0$ and π respectively, have a localized shape and won't expand into the whole azimuthal space. Therefore, there will be a region in $\Delta\phi$ where only flow background contributes, and we define this region as a single bin in our $\Delta\phi$ correlation shape where each bin of our histogram has a finite size. In practice, because we use histograms to represent "raw" functions, the "touching" of flow shape to it can be done in either direct bin-by-bin way, or we fit the "raw" function by a basic shape, a Gaussian+flat at near-side,

then let the flow shape touch this fitted shape. In either way, the stability of touching will be later counted as systematic error of ZYAM.

All jet-yield functions on different physical observables will share the same background normalization factor. In practice, we use the $dN/d|\Delta\phi|$ functions since that's where v_2s are originally derived.

An example is shown in Fig.2.4, as for the Cu+Cu correlation functions, with the trigger π^0 at $5 < p_T < 10\text{GeV}/c$, and associated charged tracks at p_T = 1-2, 2-3GeV/c. All yields under the flow line is defined as flow background of underlying events, and the area between the flow and total line will be considered as our jet contribution.

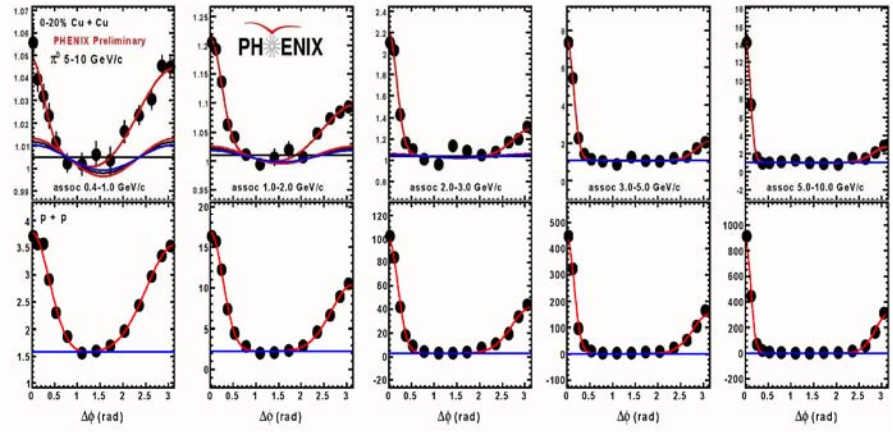

Figure 2.4 Comparing correlation functions of Cu+Cu (top) to p+p (bottom). Acceptance effects already corrected. Flow background from ZYAM method is marked on Cu+Cu plots.

2.2 Fundamental Relationships

To determine the functional form for the jet distribution after subtraction of flow contribution, we must introduce some fundamental ideas about fragmentation.

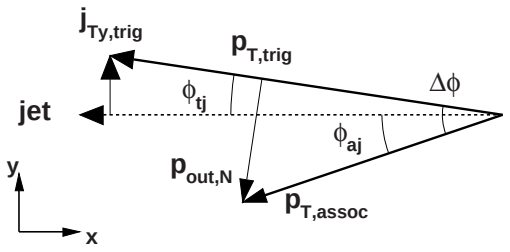

Figure 2.5 Schematic of a single event which produces two fragmenting hadrons from the same jet.

To study jets in depth, the model that that is used is an extension of that suggested by Feynman, Field, and Fox in a series of papers (84; 85; 86) in the late 1970's which addressed the results from CERN Interacting Storage Ring (ISR) p+p experiments at high-p_T at midrapidity. Fig. 2.5 and Fig. 2.6 introduce the necessary variables that are accessible to two-particle correlations.

2.2.1 Near-angle Jet Correlations

The top panel of Fig. 2.5 shows the transverse plane of a single event where two hadrons fragment from a single jet, $p_{T,trig}$ is in the trigger momentum range and $p_{T,assoc}$ is in the associated momentum range. The trigger hadron momentum is written for a single event as

$$p_{T,trig} = \sqrt{z_{trig}^2 q_T^2 + j_{Ty,trig}^2} \tag{2.12}$$

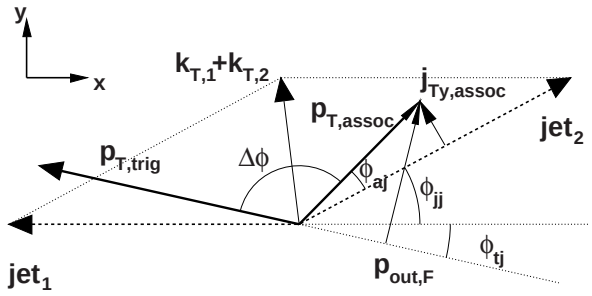

Figure 2.6 Schematic of a single event which produces one fragmented hadron from each pair from a di-jet.

where the parent parton has momentum q_T, the fragment has some fraction z_{trig} along the parent parton direction, and the fragmented hadron has a component transverse to the jet direction known as $\vec{j}_T$. This $\vec{j}_T$ has components in the transverse and longitudinal directions. The transverse component is denoted as j_{Ty}. This j_{Ty} is part of the fragmentation process. It is empirically given a Gaussian distribution but has power-law tails at very large magnitude due to hard gluon radiation (87). Similarly, the associated particle momentum is written as

$$p_{T,assoc} = \sqrt{z_{assoc}^2 q_T^2 + j_{Ty,assoc}^2} \tag{2.13}$$

where these parameters have the same meaning as described except now for the associated particle.

What is measured by two-particle correlations is the angle between the fragments, $\Delta\phi_N$. The subscript N is used here to denote the near angle correlation. This angle can be written in terms of the angles that each fragment makes with respect to the parent jet direction.

$$\Delta\phi_N = \phi_{tj} - \phi_{aj} \tag{2.14}$$

The angles on the right-hand side of Eqn. 2.14 can be written in terms of the p_T and the j_{Ty} of the fragments.

$$j^2_{Ty,assoc} = p^2_{T,assoc}\sin^2\phi_{\rm aj} \tag{2.15}$$

$$j^2_{Ty,trig} = p^2_{T,trig}\sin^2\phi_{\rm tj} \tag{2.16}$$

To better describe the jet shape and not constrained by only bins at center of near-side peak, we need to introduce a concept called $p_{out,N}$, the component of $p_{T_{assoc}}$ that is perpendicular to $p_{T_{trig}}$, as is shown in Fig.2.5.

$$p_{out,N} = p_{T,assoc}\sin(\Delta\phi_N) \tag{2.17}$$

This observable is defined in Equ. 2.17 as the associated particle's momentum transverse to the trigger direction and is directly related to shape of near-side jet. Since it is proportional to $sin(\Delta\phi)$, even bins of $\Delta\phi > 3\sigma$ can have non-trivial contribution. In our analysis, we calculate the distribution of $p_{T_{out}}$ of associated particles from the region of $|\Delta\phi| < 1$ radian, pair-by-pair, for both "real" and "mixing" events, and apply the same acceptance correction and ZYAM-background-subtraction of corresponding $\Delta\phi$ bin as described above for correlation functions.

It is necessary to square the quantities because the event averages will eventually be taken and, in the case of a Gaussian distribution, the mean is zero but the root-mean-squared, RMS, is non-zero. To use Eqn. 2.15, Eqn. 2.14 must be rewritten in terms of the sine of the angles.

$$p_{T,assoc}\sin(\Delta\phi_N) = p_{T,assoc}\sin(\phi_{tj})\cos(\phi_{aj}) + p_{T,assoc}\sin(\phi_{aj})\cos(\phi_{tj}) \tag{2.18}$$

Squaring this term and taking the event average gives

$$\begin{aligned}\left\langle p^2_{T,assoc}\sin^2(\Delta\phi_N)\right\rangle &= \left\langle p^2_{T,assoc}\sin^2(\phi_{aj})\right\rangle + \left\langle p^2_{T,assoc}\sin^2(\phi_{tj})\right\rangle \\ &\quad -2\left\langle p^2_{T,assoc}\sin^2(\phi_{aj})\sin^2(\phi_{tj})\right\rangle + \frac{1}{2}\left\langle p^2_{T,assoc}\sin(2\phi_{aj})\sin(2\phi_{tj})\right\rangle\end{aligned}$$

$$
\begin{aligned}
&= \left\langle j_{Ty,assoc}^2 \right\rangle + \left\langle \frac{p_{T,assoc}^2}{p_{T,trig}^2} j_{Ty,trig}^2 \right\rangle - 2 \left\langle \frac{j_{Ty,assoc}^2 j_{Ty,trig}^2}{p_{T,trig}^2} \right\rangle \\
&\approx \left\langle j_{Ty}^2 \right\rangle + \left\langle x_h^2 j_{Ty}^2 \right\rangle
\end{aligned} \tag{2.19}
$$

The terms of order $\left\langle j_{Ty}^4 \right\rangle$ have been neglected since $j_T \sim \Lambda \sim$ 0.4 GeV/c. Further there is an assumption that the trigger and associated j_{Ty} after event averaging will be the same. The notation

$$
x_h = \frac{p_{T,assoc}}{p_{T,trig}} \tag{2.20}
$$

has been introduced. Since the j_{Ty} distribution is approximately Gaussian, it follows from Eqn. 2.19 that $p_{T,assoc} \sin \Delta\phi \equiv p_{out,N}$ is approximately Gaussian distributed for small angles. From the correlation function the RMS of the near angle Gaussian distribution is determined and related to the RMS of j_{Ty}. By making several approximations to Eqn. 2.19, it is found that

$$
\sqrt{\left\langle j_{Ty}^2 \right\rangle} = \sigma_N \frac{\langle p_{T,assoc} \rangle \langle p_{T,trig} \rangle}{\sqrt{\langle p_{T,assoc} \rangle^2 + \langle p_{T,assoc} \rangle^2}} \tag{2.21}
$$

where σ_N is the RMS of the near-angle $\Delta\phi$ distribution.

2.2.2 Away-Side Jet Correlations

The study of the away-side correlations is much more complex. Initial state partons that participate in the hard scattering are confined within the hadron and, by simple uncertainty arguments, have some distribution of transverse momentum in the center-of-mass frame of the hadron-hadron collision. In the frame in which the partons that participated in the hard scattering were collinear, the outgoing partons from the interaction will have the same momentum and be exactly back-to-back. However, the initial state transverse momentum of the partons boosts this system into the center-of-mass frame of the hadron-hadron collision, causing the outgoing parton momenta to be different and for the partons not to be back-to-back, i.e. they are acoplanar. This transverse momentum of the partons is called $\vec{k}_T$ and is entirely in the

transverse plane (see Fig. 2.6). This partonic transverse momentum magnitude is Gaussian distributed in 2 dimensions.

$$P\left(\vec{k}_T\right) = \frac{1}{2\pi\left\langle k_T^2\right\rangle} e^{\frac{-k_T^2}{2\left\langle k_T^2\right\rangle}} \tag{2.22}$$

Similar to the analysis of the near angle, the far angle can be analyzed.

The first collaboration to systematically study away-side correlations in hadronic collisions was the CCHK collaboration at the ISR (88). They introduced two variables which are important in the study of two particle correlations. The first is p_{out} and is defined as (see Fig. 2.6)

$$p_{out,F} = p_{T,assoc}\sin(\Delta\phi_F) \tag{2.23}$$

This observable defines the associated particle's momentum transverse to the trigger direction and is directly related to the acoplanarity of the di-jets. The other is x_E

$$x_E = \frac{\vec{p}_{T,trig}\cdot\vec{p}_{T,assoc}}{|p_{T,trig}^2|} \tag{2.24}$$

which is the fractional momentum of the associated particle along the trigger direction. This observable is meant to substitute for z, the fraction of the fragment's momentum along the parent parton direction. We can relate x_E to the z of each of the fragments

$$x_E = \frac{p_{T,assoc}\cos\Delta\phi_F}{p_{T,trig}} \approx \frac{z_{assoc}}{z_{trig}} \tag{2.25}$$

This approximation is reasonable when k_T is not large enough to cause a large difference between the two parent parton momenta. These observables can be used to determine the relationship between the far angle and k_T. This is seen by first writing the far angle in a given event as (see Fig. 2.6)

$$\Delta\phi_F = \phi_{jj} + \phi_{aj} + \phi_{tj} = \phi_{jj} + \Delta\phi_N \tag{2.26}$$

Squaring and taking the sine of this and following the mathematics, it is found that

$$
\begin{aligned}
\sin\Delta\phi_F &= \sin\phi_{jj}\cos\Delta\phi_N + \cos\phi_{jj}\sin\Delta\phi_N \\
p_{T,assoc}^2\sin^2\Delta\phi_F &= p_{T,assoc}^2\sin^2\phi_{jj}\cos^2\Delta\phi_N + p_{T,assoc}^2\cos^2\phi_{jj}\sin^2\Delta\phi_N \\
&\quad + \frac{1}{2}p_{T,assic}^2\sin(2\phi_{jj})\sin(2\Delta\phi_N) \\
\left\langle p_{out,F}^2\right\rangle &= \left\langle p_{T,assoc}^2\sin^2\phi_{jj}(1-\sin^2\Delta\phi_N)\right\rangle \\
&\quad + \left\langle p_{T,assoc}^2(1-\sin^2\phi_{jj})\sin\Delta\phi_N\right\rangle
\end{aligned}
\tag{2.27}
$$

It is important to note that one component of the k_T vector is

$$
k_{Ty} = q_{T,assoc}\sin\phi_{jj} \tag{2.28}
$$

where $q_{T,assoc}$ is the parent parton momentum of the associated particle. With this definition and Eqn. 2.19, it follows that

$$
\begin{aligned}
\left\langle p_{out,F}^2\right\rangle &= \left\langle\frac{p_{T,assoc}^2}{q_{T,assoc}^2}k_{Ty}^2\right\rangle + \left\langle j_{Ty}^2\right\rangle + \left\langle x_h^2 j_{Ty}^2\right\rangle \\
&\quad - \left\langle\frac{2k_{Ty}^2}{q_{T,assoc}^2}\right\rangle\left(\left\langle j_{Ty}^2\right\rangle + \left\langle x_h^2 j_{Ty}^2\right\rangle\right) \\
&= \left\langle z_{assoc}^2 k_{Ty}^2\right\rangle + \left\langle j_{Ty}^2\right\rangle + \left\langle x_h^2 j_{Ty}^2\right\rangle - \left\langle\frac{2z_{assoc}^2 k_{Ty}^2}{p_{T,assoc}^2}\right\rangle\left(\left\langle j_{Ty}^2\right\rangle + \left\langle x_h^2 j_{Ty}^2\right\rangle\right)
\end{aligned}
\tag{2.29}
$$

Inspecting the above result, $p_{out,F}$ is the quantity that is Gaussian distributed because j_T and k_T are Gaussian distributed. If the far-angle distribution is not very wide, the far-angle can be approximated as a Gaussian. We could go further to relate the far-angle RMS to the RMS of k_{Ty} but this requires knowledge of $\langle z_{assoc}\rangle$.

To summarize, the jet function is approximately two Gaussian distributions, one centered at $\Delta\phi = 0$, the near side that is defined by j_{Ty} via Eqn. 2.21, and one at $\Delta\phi = \pi$, the far side that is defined by the convolution of j_{Ty} and k_{Ty} via Eqn. 2.29.

$$
\mathcal{J}(\Delta\phi) = \frac{S_N}{\sqrt{2\pi}\sigma_N}e^{-\frac{\Delta\phi^2}{2\sigma_N}} + \frac{S_F}{\sqrt{2\pi}\sigma_F}e^{-\frac{(\Delta\phi-\pi)^2}{2\sigma_F}} \tag{2.30}
$$

2.2.3 Di-jet Acoplanarity

An alternative variable that can quantify the di-jet acoplanarity is the angle between the jets, ϕ_{jj}. Following the derivation as above the angle between the jets can be written in terms of the measured near and far angle relative azimuth, Eqn. 2.26. Taking the sine of both sides and squaring it is similar to removing the $p_{T,assoc}$ dependence from Eqn. 2.27. We have the following after squaring each side and taking the event average

$$\left\langle \sin^2 \Delta\phi_F \right\rangle = \left\langle \sin^2 \phi_{jj} \right\rangle + \left\langle \sin^2 \Delta\phi_N \right\rangle - 2 \left\langle \sin^2 \phi_{jj} \right\rangle \left\langle \sin^2 \Delta\phi_N \right\rangle \tag{2.31}$$

This can be rearranged to find $\langle \sin^2 \phi_{jj} \rangle$

$$\left\langle \sin^2 \phi_{jj} \right\rangle = \frac{\langle \sin^2 \Delta\phi_F \rangle - \langle \sin^2 \Delta\phi_N \rangle}{1 - 2 \langle \sin^2 \Delta\phi_N \rangle} \tag{2.32}$$

The left-hand side is a partonic quantity related to hadronic variables and contains all of the information about k_T. When the jets are nearly back-to-back, $\phi_{jj} \sim$ zero, so $\langle \sin^2 \phi_{jj} \rangle$ is near zero. As the dijet distribution becomes more acoplanar, $\langle \sin^2 \phi_{jj} \rangle$ is larger than zero. Because of j_T this quantity is never exactly zero.

To relate the quantities on the right-hand side of Eqn. 2.32 it is assumed that the angles are Gaussian distributed. This is not exactly true as was argued above but by inspection of the correlation functions this is a reasonable approximation. Quantitatively it is good to less that 2%. Since the angles are small the sine term can be expanded.

$$\begin{aligned} \left\langle \sin^2 \Delta\phi \right\rangle &= \left\langle \left(\Delta\phi - \frac{1}{6}\Delta\phi^3 + \frac{1}{120}\Delta\phi^5 + \ldots \right)^2 \right\rangle \\ &= \left\langle \Delta\phi^2 \right\rangle - \frac{1}{3} \left\langle \Delta\phi^4 \right\rangle + \frac{2}{45} \left\langle \Delta\phi^6 \right\rangle + \ldots \end{aligned} \tag{2.33}$$

The first term, $\langle \Delta\phi^2 \rangle = \sigma^2$, is the measured RMS. For a Gaussian distribution the higher even moments are related to the RMS by

$$\left\langle x^{2n} \right\rangle = (2n-1)!! \left\langle x^2 \right\rangle^n = (2n-1)!! \sigma^{2n} \tag{2.34}$$

In this case the higher powers are

$$\left\langle \Delta\phi^4 \right\rangle = 3\left\langle \Delta\phi^2 \right\rangle^2 = 3\sigma^4 \tag{2.35}$$

$$\left\langle \Delta\phi^6 \right\rangle = 15\left\langle \Delta\phi^2 \right\rangle^3 = 15\sigma^6 \tag{2.36}$$

These are substituted into Eqn. 2.33 and the expansion in terms of the Gaussian RMS of the angle is

$$\left\langle \sin^2 \Delta\phi \right\rangle = \sigma^2 - \sigma^4 + \frac{2}{3}\sigma^6 \tag{2.37}$$

This approximation is good to 2% for $\sigma < 0.5$ rad and 0.6% for $\sigma < 0.2$ rad. The final result is

$$\left\langle \sin^2 \phi_{jj} \right\rangle = \frac{\left(\sigma_F^2 - \sigma_F^4 + \frac{2}{3}\sigma_F^6\right) - \left(\sigma_N^2 - \sigma_N^4 + \frac{2}{3}\sigma_N^6\right)}{1 - 2\left(\sigma_N^2 - \sigma_N^4 + \frac{2}{3}\sigma_N^6\right)} \tag{2.38}$$

In high-p_T p+p, d+Au, and Au+Au collisions the acoplanarity is quantified in terms of Eqn. 2.38.

2.2.4 Fragmentation Functions

The yields from the correlations can be related to the fragmentation functions by way of x_E distributions. The goal is to write the single inclusive spectrum in a factorized form. To do so we must first write it assuming all processes happen in vacuum, like what people did in $e\pm$ annihilation. The distribution of partons in the final state is defined as

$$f_q\left(q_T\right) \equiv \frac{1}{q_T}\frac{d\sigma_{hard}}{dq_T} \tag{2.39}$$

This distribution represents the hard parton cross-section for all of the different channels which produces an outgoing parton at q_T. The fragmentation function is defined as usual

$$D(z) = \frac{d\sigma_{frag}}{dz} \tag{2.40}$$

This fragmentation function is the effective fragmentation function which describes the probability of a parton to produce the single particle in question. The single particle distribution follows from these definitions.

$$\begin{aligned} d\sigma &= d\sigma_{hard} d\sigma_{frag} \\ &= q_T f_q\left(q_T\right) dq_T D(z) dz \\ &= \frac{p_T}{z} f_q\left(\frac{p_T}{z}\right) \frac{dp_T}{z} D(z) dz \end{aligned} \tag{2.41}$$

The last line follows for a fixed z. To find the p_T distribution the integral over z is performed. The lower limit of z is $x_T = 2p_T/\sqrt{s}$ since the parton cannot have a lower momentum than the fragment. The upper limit is 1, the kinematical limit. Therefore, the single inclusive spectrum can be written as

$$\frac{1}{p_T}\frac{d\sigma}{dp_T} = \int_{x_T}^{1} \frac{dz}{z^2} f_q\left(\frac{p_T}{z}\right) D(z) \tag{2.42}$$

Assuming some form for the final state parton distribution, $f_q\left(q_T\right)$, it is possible by a fit to the data to numerically extract the fragmentation function in form of z. This function is however biased by two facts: 1) z is the ratio of di-jets, and the associated selection will bias not only z_a but z_t and 2) k_T smearing.

Further information on fragmentation functions can be obtained from the associated particle distributions, $dN/dp_{T,assoc}$ and dN/dx_E. Following the same arguments as above the pair cross-section can be written as

$$\begin{aligned} d\sigma &= d\sigma_{hard} d\sigma_{frag,trig} d\sigma_{frag,assoc} \\ &= q_T f_q\left(q_T\right) dq_T D\left(z_{trig}\right) dz_{trig} D\left(z_{assoc}\right) dz_{assoc} \\ &= \frac{p_{T,trig}}{z_{trig}} f_q\left(\frac{p_{T,trig}}{z_{trig}}\right) \frac{dp_{T,trig}}{z_{trig}} D\left(z_{trig}\right) dz_{trig} D\left(\frac{p_{T,assoc}}{p_{T,trig}} z_{trig}\right) \frac{dp_{T,assoc}}{p_{T,trig}} z_{trig} \end{aligned} \tag{2.43}$$

The last line follows when assuming that q_T is the jet momentum for both jets, that is, assuming no k_T introduces any difference between the outgoing jet momentum. The integration over z_{trig} can be performed with the same limits as before yielding the pair cross-section.

$$\frac{d^2\sigma}{dp_{T,trig}dp_{T,assoc}} = \int_{x_{T,trig}}^{1} \frac{dz_{trig}}{z_{trig}} f_q\left(\frac{p_{T,trig}}{z_{trig}}\right) D\left(z_{trig}\right) D\left(\frac{p_{T,assoc}}{p_{T,trig}} z_{trig}\right) \tag{2.44}$$

In this distribution the interpretation of the f_q function changes to that distribution which produces two (azimuthally) back-to-back partons both with q_T. Each of the fragmentation functions then represent the probability for a parton to fragment to the trigger and the associated particle. In principle they should not be the same function when dealing with different particle types for the trigger and associated particles.

Finally, this pair distribution can be related to the x_E distribution by making the substitution of $p_{T,assoc}$ with x_E for a fixed $p_{T,trig}$. By the definition of x_E, Eqn. 2.24

$$\begin{aligned} x_E &= \frac{p_{T,assoc}}{p_{T,trig}} \cos\Delta\phi_F \\ &= \frac{p_{T,assoc}}{p_{T,trig}} \left(\cos\phi_{jj}\cos\Delta\phi_N - \sin\phi_{jj}\sin\Delta\phi_N\right) \\ &\approx \frac{p_{T,assoc}}{p_{T,trig}} \cos\Delta\phi_N \\ &\approx \frac{p_{T,assoc}}{p_{T,trig}} \sqrt{1-\sin^2\Delta\phi_N} \\ &\approx \frac{p_{T,assoc}}{p_{T,trig}} \sqrt{1-\frac{j_{Ty}^2}{p_{T,assoc}^2}} \end{aligned} \tag{2.45}$$

This is good only when k_T is small, which was also used in deriving the pair distribution. Therefore, the x_E distribution can be related to the $p_{T,assoc}$ distribution approximately as

$$\frac{1}{N_{trig}}\frac{dN}{dx_E} \approx \frac{p_{T,trig}}{\sqrt{1-j_{Ty}^2/p_{T,assoc}^2}} \frac{1}{N_{trig}}\frac{dN}{dp_{T,assoc}} \tag{2.46}$$

Each of the distributions is proportional to the cross-section. This affects the normalization of the distribution only and not the shape. Therefore, the $p_{T,assoc}$ and x_E distributions are proportional to an integral containing the product of the trigger and associated fragmentation functions. These were derived with the $k_T \approx 0$. Adding k_T is possible with the risk of double counting but the distributions are not dramatically affected even with a large (double counted) k_T.

CHAPTER 3. PHENIX Detector in Heavy Ion Collisions

This chapter is the introduction of PHENIX detector. While PHENIX is a complex system capable of multiple categories of particles, my analysis are focused on jet correlation, and the physical observables are from the high-pT hadrons from hard-scattering parton fragmentation. Thus, I will concentrate on the detector components I have been using in my analysis. I will introduce these components based on the particles they measure. A lot of technical content comes from the PHENIX technical publications, and more details about the detector can be found there. The direct access to these technical papers are the NIM papers. (89) The actual parameters used in my analysis will be introduced in the next chapter.

3.1 PHENIX Overview

The physical result of my analysis work in the following chapters were provided by the Relativistic Heavy Ion Collider (RHIC) at Brookhaven National Laboratory in Upton, New York. This RHIC utility is able to collide a variety of collision particle species including p, d, Au and Cu. And collider works over a wide range of center of mass energies, from $\sqrt{s_{NN}} \sim 20$GeV to 500GeV. The object of design is to achieve high enough energy density to reach the phase change region in QCD that we described in the introduction chapter. There have been four relativistic experiments set up on RHIC. Their names are BRAHMS, PHENIX, PHOBOS, STAR. The specific experiment used in our measurement is called the PHENIX detector, the Pioneering High Energy Nuclear Interaction eXperiment. It is a large, multipurpose detector with several integrated subsystems used for event triggering and characterization, charged particle tracking, and electro-magnetic calorimetry. To achieve these purposes, multiple detectors components have been installed into PHENIX. Two central arms, each covering 90

degrees in azimuth and $-0.35 < \eta < 0.35$ in pseudo-rapidity, are utilized for measurements of photons and charged hadrons in the central rapidity region. Two other spectrometer arms at forward and backward rapidity $1.2 < \eta < 2.2$ are designed for muon measurements. Two detectors, Zero-Degree Calorimeters and Beam-Beam Counters, are placed close to the beam pipe. This set of detectors is used to determine global event information, including centrality as an observable of impact parameter T_{AB}. The 2004/2005 PHENIX detector configuration is illustrated in Fig. 3.1, showing a view along the beam direction.

The PHENIX coordinate system is right-handed and chosen such that the z-axis is oriented along the beam pipe in the direction of the north muon arm. The x-axis points into the west central arm and the y-axis is perpendicular to the other two axes. One Central Magnet and two Muon Magnets with iron yokes and water cooled copper coils generate an axial magnetic field for the central arm and a radial field for the muon arms, respectively. The magnetic field bends the charged tracks and provides momentum measurement.

3.2 Event Selection and Characterization

Two pairs of detectors at forward/backward pseudo-rapidity are used to determine the necessary global event information. The basic idea is to detect the physics observables of global event at a pseudo-rapidity region far away from the region where our analysis focus happens, so that they won't make bias through direct correlation. The global observables include collision z-vertex, event centrality and reaction plane. These global observables help us to categorize physics events in our analysis, and often work as starting points of other detector measurements. For example, all Time-of-Flight (TOF) measurement rely on global timing information as starting point. Also, the level one trigger system (Sec.3.2.3) relies on these global observables. We need triggers to keep as much cross-section as our hardware limit allows, while still keeping the ability of selecting those physics events we are mostly interested in. We will explain these global-event detector and their applications in the following sections.

3.2.1 The Zero-Degree Calorimeters

Two compact hadronic Zero-Degree Calorimeters (ZDC) with tungsten absorber plates are installed close to the beam pipe at a distance of 18m north and south of the center of interactive region (z=0), located at very forward ($|\eta| > 6$) pseudorapidities. The main purpose is to provide the information of overlapping geometry in nuclei-nuclei collision, by measuring a clear portion of neutrons from the nuclei after collisions. Since the ZDCs are located behind the beam dipole magnets from collision point of view, the charged particles are bent away from the ZDC. At ZDC, we have a clear determination of the deposited energy of spectator neutrons with a resolution of 20%. This energy deposit comes from the part of nuclei not participating the collision and gives a direct measurement of colliding geometry.

3.2.2 The Beam-Beam Counters

The two Beam-Beam Counters (BBC), each composed of 64 Cherenkov PMTs with quartz glass radiators, are positioned along the beam axis at a distance of 1.44m relative to the center of the interaction region, and referred to as BBCN (North) and BBCS (South), respectively. Each BBC array is installed circling the beam pipe and has full azimuthal coverage plus a pseudorapidity acceptance $3 < \eta < 3.9$.

Whenever two nuclei collide, those charged particles produced at forward pseudo-rapidity go through BBC. These particles emit Cherenkov radiation in the glass radiators, and BBC collect the light signals. The BBCs measure the uncorrected arrival time T_{raw}, via the average timing of hits. After subtraction of an offset determined by an iterative minimization of the residual times of all BBC elements, one obtains the corrected arrival time $T_{corr} = T_{raw} - T_{offset}$. By looking at the T_{corr} of both north and south BBCs and compare the timing difference, we can decide the actual time and position one nucleus-nucleus collision happens. The timing resolution of BBC is 20ps, and the z-vertex position of the collision can be obtained from the time difference in both BBCs with a resolution of 6 mm. This starting time t0 provides the start time for the time of flight (ToF) measurements with the ToF detector and Electromagnetic Calorimeter (EmCal) subsystems, with a resolution of 52 $\pm$ 4ps. The z-vertex works as the

initial condition of all particle tracking.

3.2.3 The Minimum-Bias Trigger

Because the collision-event rate happened in the interaction region is usually higher than the computing ability to record, it's important to filter events based on their detector response at first time. Those events show a higher probability of interesting physics shall be given higher priority to be recorded. In PHENIX this mechanism is called "level-one trigger". .

The level-one trigger record usually the most hard-scattering cross-section in PHENIX is called "minbias trigger". The collision vertex and the number of hits in the BBC photomultipliers are key variables for the PHENIX minimum bias trigger. The trigger efficiency was evaluated via Monte Carlo simulations and found to be 92 ± 2 % of the inelastic cross section for Au+Au and Cu+Cu collisions and 88.5 % of the d+Au cross section, respectively. In p+p collisions, the lower multiplicity in BBC often lowers this percentage, and we increase the bandwidth for events with higher probability of hard-scattering. For example, the ERT trigger (Sec.3.3.3.3) is defined, where a BBC and Central Arm coincidence is required. This trigger is useful to tag and filter a jet-containing event using high-p_T particles in real time.

Meanwhile, the ZDCs also provide a coincidence signal for the minimum bias level-one trigger and permit the reconstruction of the z-vertex from the time difference in both detectors. Although not as good resolution as BBC, the larger cross-section coverage makes ZDC well suited to monitor luminosity during data taking.

Beside min-bias trigger, we also would like to trigger on those rare events containing physics we are more interested in. This is achieved by detector-specific triggers other than those from global event detectors. For example, to select those rare Drell-Yan events, a di-muon trigger is set up. This trigger selects those events containing two high-momentum muons at the same forward direction.

3.2.4 Centrality

We explained in the introduction chapter that centrality is defined to quantitize the overlapping area of two colliding nuclei. This collision centrality can be defined from any variable that is a monotonic function of the impact parameter T_{AB}, such as total multiplicity, total transverse energy, etc. The BBC charge sum distribution fulfills this requirement since it's proportional to the nuclei-nuclei scattering cross-section. This calculation is then done through a Glauber model Monte Carlo simulation (21; 22) described in Sec.. In d+Au and Cu+Cu collisions BBC can solely determine the centrality. In Au+Au collisions, the narrower BBC charge distribution at peripheral collisions (smaller T_{AB}) makes the help of ZDC necessary. We make cuts in the 2-D distribution band of ZDC versus BBC analog response as shown in Fig. 3.2. This is a two dimensional plot of BBC charge sum versus the energy deposited in the ZDC.

The calculated centrality are then used to calculate the scaling factors such as N_{coll}. We wrote before that the N_{coll} 1.2.3 and N_{part} are used to scale the probability of hard-scattering in the corresponding centrality bins. These average number of collisions N_{coll} and number of participants N_{part} (90) in the overlapping geometry of two nucleus are also monotonic functions of centrality or T_{AB} . Hence both can be calculated in each centrality bin using the Glauber model (21; 22).

In practice, the number of nuclei participants N_{part} is frequently used to characterize the centrality of a nucleus-nucleus collision, especially when reactions of nuclei with different mass number A are compared. The number of inelastic nucleon-nucleon collisions N_{coll} and the nuclear overlap function T_{AB} for a given centrality class are related quantities, as in Equation.3.2.4

$$T_{AB} =< N_{coll} > /\sigma_{nn} \tag{3.1}$$

3.2.5 Reaction Plane

To identify jets from the big soft-interaction background, we need to measure the soft background. As we claimed in Sec.2.1.4.1, this soft background is dominated by the elliptic flow effect. The measurement of flow requires a fine measurement of event-by-event reaction plane, which is defined by z-axis and the line connecting centers of two nucleus (Sec.1.2.8.2). As we introduced, the source of flow is that original anisotropy of colliding geometry produces the later momentum anisotropy in particle production. Hence, the particles produced within the reaction-plane tend to have higher momentum and produces more radiation lights in BBC. That's how we can measure the reaction-plane in Run 4/5/6 by BBC, via the peak of weighted angle distribution of radiation signals in BBC photomultipliers (PMT). A more precise formula in finding peaks is by arc-tangential of ratio of sum of sin and cos function of angle distribution (see 3.2.5), each weighted by the charges of each hit.

$$\Psi = tan^{-1}\frac{\sum sin(\Psi_i) * W_i}{\sum cos(\Psi_i) * W_i} \tag{3.2}$$

A particularly attractive feature of BBC is the relatively large pseudorapidity gap $\Delta\eta > 6$ between the north and south BBCs, which serves to minimize the non-flow contributions to the reaction plane determination. Since we have a pair of BBCs at both north/south of collision vertex, it's also convenient to compare their results to estimate the systematic error of our reaction plane measurement. The resolution of reaction plane is decided usually by comparing the Ψ from two BBC components. This resolution will be propagate to our systematic error, too (24) .

Since Run 2007, a new detector specifically designed for reaction-plane measurement (RXNP) was introduced. This means we will have multiple reaction-plane measurement included in our primary data output, and analyzers will have choices other than the traditional BBC RP output. However, RXNP is not used in our analysis in this thesis.

3.3 Single Particle Measurement at Central Arms

This chapter summarizes how we measure each type of particle we use in our correlation analysis. Only central arm detectors in Fig. 3.1 are mentioned here as that is where all the particles used in our particle correlation analysis come from. These particles include high-energy π^0 as our trigger (tagging jets) and charged hadrons as associated particles. π^0 are selected as trigger because that's the highest-energy identified particle PHENIX can measure, and charged hadrons are selected as associates because of their high multiplicity in the central-arm region. Multiple combination of detectors are used to reconstruct these particles and remove the background noise, including fake particles. The "good" particles, both π^0 and charged hadrons, will be kept and used to form two-particle correlation function in our analysis. We will explain the actual parameters of these cutting thresholds in the following chapter.

3.3.1 Central Magnetic Field

The PHENIX magnetic field is a combination of four different magnets, two for the central arms, and one for each of the muon arms. Our analysis work in next chapters concentrates at the central arm region. Because the field of muon magnets only slightly affect the central arm region on the edge, we will focus on the central arm magnets.

This central arm field is designed that it is approximately axial along the beam-axis, so that charged particles bend only in azimuthal space in central-arm region. Because the Drift Chamber (see Sec. 3.3.2) has better resolution in azimuthal plane, we maximize the pT sensitivity.

There have been several different field configurations by operating independently the inner and outer coil of each central magnets. For example, the "++" configuration has both coil pointing their fields to positive z-axis direction (or "−−" if to the negative z-axis direction). This results in the largest magnetic field of about 9 kG at the center of the interaction region, while decreasing racially outward and becoming negligible with a strength of a few hundred Gauss at about 2.2 m radius, the center of the Drift Chamber. On the other hand, the "+−" configuration results in a field that is zero at the center of the interaction region, peaking at

3.5 kG at around 1 m from the beam line, and decreasing until it is negligible at around 2.2 m radius, the DC center. In Run4 and Run5, the mainly used field configurations are "++" and "−−". In Run6 we used mainly "++". Zero-field runs are also taken time-to-time for the purpose of calibration (see Sec.4.4). The actual field is measured by probes put at multiple positions at the beginning of each PHENIX run year, and then calculated for the whole space.

3.3.2 Charged Tracks

3.3.2.1 Drift Chamber

The two PHENIX drift chambers covers each $\pi/2$ in azimuth and 180cm in the z direction, centered around midrapidity, and their main purpose is the charged-particle tracking. The drift chambers are positioned outside the magnetic field from 2.02m to 2.46m in radial distance from the interaction point.

Each drift chamber (east or west) consists of 20 sectors, each with six wire layers: X1, U1, V1, X2, U2 and V2. Fig. 3.3 shows a side view of a single sector. There are four types of wires in the drift chamber as shown.

The potential wires create the drift electric field in the detector. The gate wires further shape the field to direct the charge toward the sense wires from one side. A gas mixture is supplied to the wires inside drift chambers. When charged particles pass through the drift chambers, they will ionize the gas mixture. The electrons released from gas then move under the high voltage field, and are collected by those sensor wires as hits. The back wires block charge from the other side from reaching the sense wires, and prevents left-right ambiguities in the hit position. The gas is composed of 50% argon and 50% ethane with $< 1\%$ alcohol, for maximum performance.

The hit position is measured by the time the electrons hit the wire, which is ensured by the fast response time under strong field. Each track consists of many (up to 41) wire hits inside the DC. The U and V wire layers are oriented at an angle of 6° with respect to the X layers, and opposite ends of the U and V layers are in neighboring sectors. The U and V layers provide z position information on the tracks, and the X layers provide ϕ position information in the

azimuth space. Because of the narrow pseudo-rapidity coverage of PHENIX central-arms, we need better resolution in the azimuthal plane. The DC provides a spatial resolution better than 0.15mm in ϕ direction, two track separation better than 1.5mm, and spatial resolution in the z direction better than 2mm. The single wire efficiency is 95%; the single track efficiency is $> 99\%$, without considering the effect of occupancy and ghost tracks.

The momentum vector of a charged particle at the DC is calculated by measuring the angular deflection of the track from a straight line trajectory using average hit positions back to the collision vertex, see Fig. 3.4. Assuming this track originates from the collision vertex (decided by BBC), the hits in DC are looped back to the collision vertex in the field, using a fine timing and space resolution magnetic map. The original momentum vectors of the tracks in DC are fitted by minimum χ^2 method then. For those particles not originating from collision vertex, such as decayed ones, they may leave enough number of hits in DC to be reconstructed as tracks, although usually in unrealistic (high) momentum, or even failed the χ^2 threshold. Some of these "fake" tracks shall be removed by the charged track quality cut (see Sec. 4.3.1).

During the track reconstruction, measured charge points in the X1 and X2 wires in the Drift Chamber are transformed into two-dimension tracks in a space defined by the two angles ϕ_{DC} and α. Here, ϕ_{DC} is the azimuthal angle of the track at its intersection with the DC reference radius R, and α is the inclination angle between the track and a straight line drawn from its intersection with R to the collision vertex as illustrated in Fig. 3.4. In practice, n hits in DC from the same real track produce a spike with amplitude n(n-1)/2, much larger than the average background produced by random combinatorials. For each DC track passes this threshold, those PC1 hits that lie within 2 cm of the track in the transverse plane are projected back to the BBC z-vertex to determine the track z-coordinate at DC center. The underlying assumption is that, due to the small radial magnetic field in the central arm, tracks will bend very little in the z-direction. The z-coordinate information from the DC stereo wires are also applied to remove the ambiguities between multiple PC1 hits.

3.3.2.2 Pad Chamber

The charged tracks reconstructed by DC is then projected onto three layers of multi-wire proportional chambers known as the pad chambers (PCs). The projections of DC tracks are then matched with PC hits to remove backgrounds including conversions, albedo, and decays. Because all charged tracks are reconstructed and projected in magnetic field assuming they are from collision vertex, these "noise" tracks don't have a valid matched hits in PC, as they do not likely originate from collision vertex and their momentum vector are unrealistic.

The Pad Chamber are also composed of sensor wires. Particles travel through these wires ionize the gas and the signals are collected, in a similar mechanism to that of DC. The operating gas for the Pad Chamber (like for the DC) is a 1:1 mixture of argon and ethane.

The PCs are labeled:
PC1 for the inner most located in both arms directly behind the DCH,
PC2 for the intermediate chamber located only in the West Arm behind the RICH, during years of Run 2004 and 2005 (see Fig. 3.1),
and PC3 for the outer chambers located in both arms in front of the EMC.

These detectors each have a single set of sense wires along the z-direction. These wires are segmented into pixels 8.2 mm along z by 8.4 mm in ϕ. A single "pad" is formed by formation of pixels shown on the left panel of Fig. 3.5.

A single cell is formed by three adjacent pads as shown, thus it has smaller size resolution than a single pad. Because we require one valid "cell hit" if the track goes through all three pads in the same area of one cell, we reach a better resolution using cells than the size of pads. On the other hand, we only have to develop electronics of pad size instead of having to develop much smaller (pixel or cell) size ones.

The resulting performance of the pad chambers are greater than 99.5% hit efficiency even in the high-multiplicity Au+Au environment and a z-resolution of 1.7 mm. The two-track resolution for PC1 and PC3 is 4 cm and 8 cm, respectively.

3.3.2.3 Charged Track Quality

Because of the multiplicity in high-energy collisions, it's possible to have either reconstructed tracks missing hits, or fake tracks reconstructed from physically uncorrelated hits. Thus it's important to define the track quality. The track model assigns a quality variable to the track that reflects its reconstruction history. The quality is represented by a 6-bit word, and each bit represents whether the hits of this track are good at certain layer (X1, X2, UV1, UV2, PC1 match existing, PC1 unique match), and the binomial value of this word is recorded. Here PC1 matching means if we project the DC track in the field to the PC1 planes, and find within a fixed $\phi-$z window around the projection point, those real PC1 hits. Because all projections assume the track is from collision vertex, those decay tracks are unlikely to find their matchings. On the other hand, one track can have multiple PC1 hits matched to this track due to random matching.

For example, if the track has information of all 5 layers, but has multiple PC1 match, all bits but the highest one will be 1, its quality is 31. The momentum resolution of high quality tracks in the drift chamber and pad chamber finally is δp/p = 0.7% $\oplus$ 1.0% p(GeV/c) for the Au+Au in Run2 and δp/p = 0.7% $\oplus$ 1.1% p(GeV/c) for the d+Au and p+p in Run3. We are still waiting for the newest result from Run5 and Run6 spectrum analysis. Before that, we are going to use the Run2 and Run3 systematic errors in our analysis.

A shortcoming of this approach is that low momentum decay daughters can be falsely reconstructed as high momentum tracks. To reject background coming from decays, albedo, and conversion electrons, the charged tracks are also projected to the PC3 plane and compared with pad chamber hit information. Because there is a big distance between DC and PC3, all those background with unrealistic momentum are more likely to be out of the $\phi-$z matching window and rejected. In practice, we fit the distribution of matching difference in either ϕ or z -space to double-Gaussian shape. One Gaussian represents the matching result (thus the quality) of tracks, and the other Gaussian (much broader) means the random combinatorials between DC and PC3. The 2nd Gaussian is removed by doing cross-matching between north-DC and south-PC3, or vice versa. This is called "swap matching" and help quantify the

random matching background. Then we can get the width of 1st Gaussian shape, and use the PC3 matching Δz or $\Delta\phi$ in unit of σ of Gaussian to quantify the PC3 matching quality of tracks. More details on PC3 matching cuts are in later Sec.4.3.1.

Because the detector isn't perfect in detecting all charged particles passing through, especially in case of high occupancy, we need the single-track efficiency of DC/PC system. This job is done via a Monte-Carlo simulation in PISA 6.2.4. Single particles go through the detector volumes then the normal data reconstruction stages. The percentage of successfully reconstructed particles gives us the detector efficiency. On the other hand, in practice we can directly count the reconstructed tracks spectrum in real event, and compare it to (divide it by) published spectrum to get the efficiency. We will describe the result in later chapter.

3.3.3 Photons and π^0s

For our π^0analysis, we used the high-branching-ratio $\pi^0 \longrightarrow \gamma + \gamma$ decay channel to reconstruct π^0. The outmost Electro-Magnetic Calorimeters (EMCal), include both Pb-Gas Scintillator (PbSc) and Pb-Glass Cherenkov Counter (PbGl). The photons create electro-magnetic showers in the calorimeters and form clusters of deposited energy. This EMCal also works as a filter of fake high-momentum charged hadrons by looking at the E/p of these hadrons explained later in 3.3.3.1. Electrons as a background of both our charged hadron and photon measurement are rejected by the Ring Imaging Cherenkov (RICH) detector.

We also use EMCal and RICH combination in our level one triggering system to filter those events containing a high-p_T π^0.

3.3.3.1 Electro-Magnetic Calorimeter

The Electromagnetic Calorimeter (EmCal) consists of two subsystems: six sectors of lead-scintillator (PbSc) detectors and two sectors of lead-glass Cherenkov counter (PbGl) detectors, and cover the full central arm acceptance of PHENIX. Both sets of detectors have been designed to measure electrons and photons with excellent timing, good position and energy resolution. The PbSc has excellent timing resolution of about 100 ps for electrons and photons nearly

independent of the incident energy. It's energy resolution from beam tests is $8.1\%/\sqrt{E(GeV)}\oplus$ 2.1%. On the other hand, the PbGl has excellent energy resolution of $5.9\%/\sqrt{E(GeV)}\oplus 0.8\%$, and a timing resolution of about 300 ps.

The charged particles and/or photons interacting in the lead produce a spray of electrons and photons which scintillate in the scintillator and the resulting light is readout by PMTs. Electromagnetic showers are primarily identified by time-of-flight (TOF) and shower shape. Because electrons are light and photons are massless, they are the first to arrive at the EMC. After correcting for the flight time from the interaction point to the EMC using the BBC timing information 3.2.2, a peak at $t \sim 0$ is seen for photons and electrons. Heavier hadrons show up as long tails at long times in the distribution.

In the PbSc, the shower shape is corrected for the impact angle and the energy of the photon. To quantify the shower shape in the PbSc, the χ^2 variable of each photon cluster in EMCal is defined as:

$$\chi^2 = \sum_i \frac{(E_i^{measure} - E_i^{predict})^2}{\sigma_i^2} \tag{3.3}$$

where E_i^{meas} is the energy measured at tower i of this photon cluster, E_i^{pred} is the predicted energy for an electro-magnetic particle of total energy $\sum_i E_i^{meas}$, and σ_i is the predicted fluctuation in energy in the tower i. This χ^2 value is useful for the discrimination of electromagnetic showers from hadron showers.

EMCal also provides a good measurement of the hadronic energy, although the hadronic response is well understood only for the PbSc detector. For this reason, and also because of the reasonable timing resolution, the PbSc can work for hadron identification, but our analysis won't go deep in this direction. We are going to use inclusive high-pT charged hadrons.

A better rejection of background such as fake high-momentum charged hadrons results from requiring the high momentum particle candidate have an E/p $\approx$ 1. This E/p is defined as the ratio of energy the particle deposited in EMCal to its momentum reconstructed via Drift Chamber. Also, conversions can be removed by doing a spatial matching of DC or PC hits projected to EMCal vs. EMCal clusters. All these cutting parameters will be described

in detail in the chapter of analysis.

The further technical details of PbSc and PbGl can be found at PHENIX NIM paper (89).

3.3.3.2 Ring Imaging Cherenkov Radiator

The Ring Imaging Cherenkov detector is a ethane-filled volume. If a charged particle passes through the medium with $v_{particle}^{inmedium} > v_{light}^{inmedium}$, it will radiate Cherenkov light and be detected. Electrons radiate above 18 MeV/c and charged pions radiate above 4.9 GeV/c. Particles above the threshold velocity, c in medium, emit light around a Cherenkov cone with a half angle dependent on their velocity. This Cherenkov light is reflected off the back of the RICH by a set of mirrors that focus the light onto a series of PMTs to be read out.

Electrons are determined by matching DCH-PC1 tracks to the outer detectors (PC2 and/or PC3), to the EMC cluster of an electromagnetic shower, and to a RICH Cherenkov ring. This makes RICH a key detector in identifying electron signal, or removing the electrons as background from our photon or charged pion samples, as discussed in our analysis in the next chapters.

3.3.3.3 ERT Trigger

In p+p collisions, because the low multiplicity, a hard-scattering can be missed if we rely on only the strong signals on BBC detector, as we did in AA collisions. Thus we need the min-bias trigger to loose threshold on signal strength, while expand the $\phi-$z space of trigger. This means a central-arm coincidence is necessary.

The fast readout of the PMTs allows the RICH and EMCal to be part of the Level-1 triggering. We make our level-one triggers in form of combinations of EMC and RICH modules, each composed of multiple detector cells, with different EMC cluster energy threshold, and decisions on whether we require or exclude the electron signal in RICH. These are called ERT triggers, and give us good ability of selecting jet-containing events in real-time mode (online). The application of trigger information in our physics analysis (offline) will be discussed in our analysis next chapters.

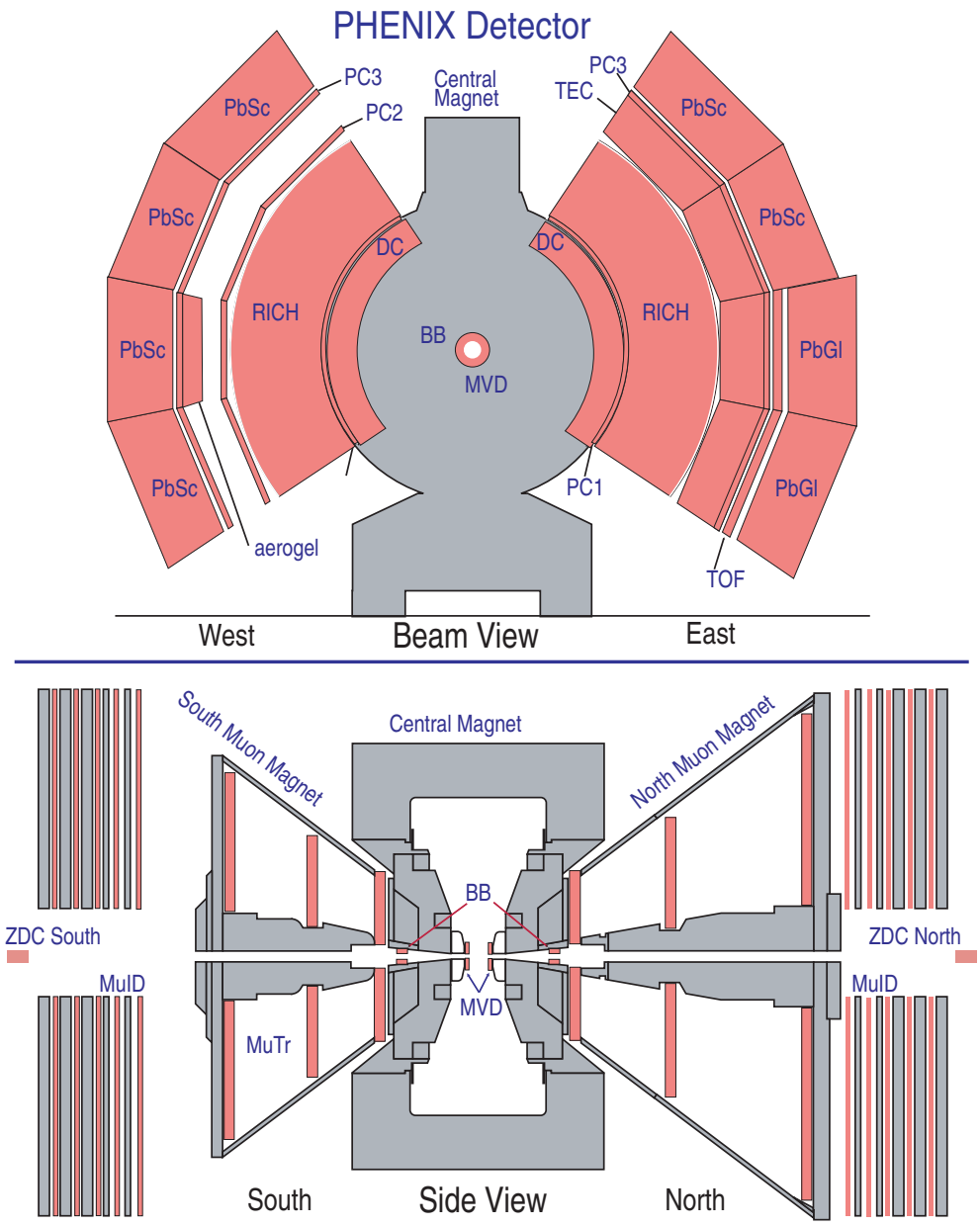

Figure 3.1 This is the cross-view cartoon of PHENIX detector in 2004. We show the central arms only since no muon arms were used in my analysis. In 2005 the main change is the expansion of Aerogel PID system on the west arm, but our analysis didn't use that component.

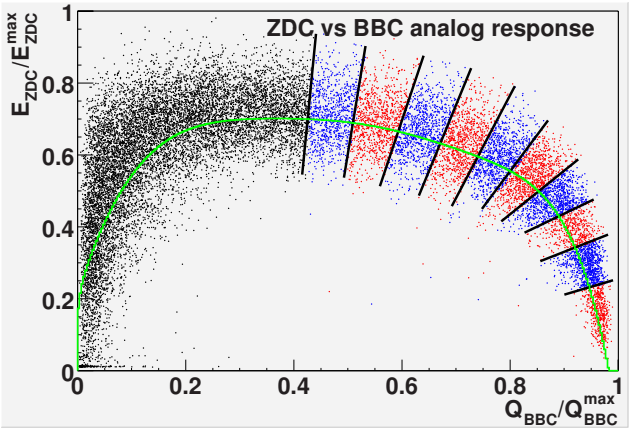

Figure 3.2 Correlation between BBC charge sum and energy deposit in ZDC. The lines define bins containing intervals covering 5% centrality. The bin to the far right represents events ranging from 0 to 5% centrality. The central line shown in the figure is the centroid of the BBC-ZDC distribution with the lines defining the centrality bins drawn perpendicular to it.

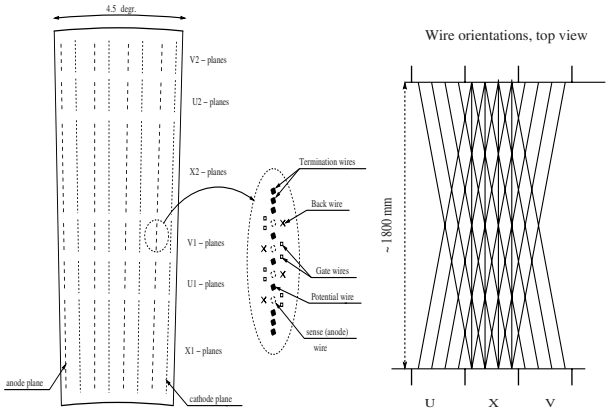

Figure 3.3 The layout of wire position within one sector and inside the anode plane (left). A schematic diagram, top view, of the stereo wire orientation (right).

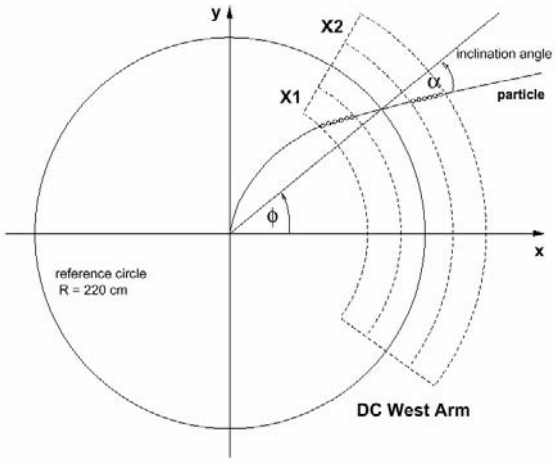

Figure 3.4 A brief cartoon of how charged tracks are reconstructed via DC hits.

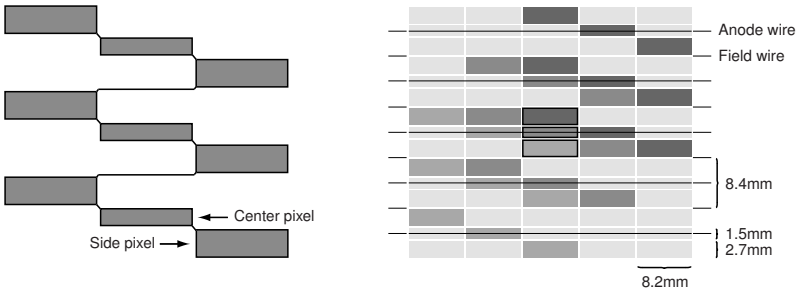

Figure 3.5 The pad and pixel geometry (left). A cell defined by three pixels is at the center of the right picture.

CHAPTER 4. Particle, Event and Run Selection

Now that we already have all combinations of detectors for our purpose of physics observation, it's important to categorize physics observables we use in our jet analysis. We will introduce our event and single particle selection criteria in the following sections.

4.1 Run Selection

In the actual running of RHIC-PHENIX, each beam store are injected into the blue/yellow RHIC rings and sustain a few hours. The data acquisitioning system (DAQ) is designed in such a way that it will take data for ∼1hour, then stop (automatically). This is called one "Run", a different concept to our RHIC-Runs marked with calendar years. In the later chapters, this word "Run" will always mean this one-hour-run unless followed by the calendar year number.

The start of one run is always manually started by the operator on shift. This will give the shifters a chance to decide if the current experiment is in good status to start.

It's important to keep the physics events we are interested in within a consistent experiment environment for quality assurance (QA). For this purpose, real-time experiment parameters that have important effects on the quality of data are recorded to electronic log book. These parameters include the magnetic field configuration, beam luminosity, level-one trigger rates, spin configuration (in p+p), and intended detector movements (e.g., installation of converters). These parameters are measured between physical runs, using specific detector configurations, sometimes running exclusively and/or based on existing most recent physics data. Then these parameters are used during the physical run by DAQ operation, to maintain a uniform performance of detectors. We call this "on-line" calibration, contrary to the "off-line" calibration later done to the reconstructed data. The 1-hour policy also permits calibration work based

on a short time interval and give more stable output.

All these factors will be included in the later run-by-run QA analysis. Because our data of analysis come from multiple kinds of collision systems, each collision system will have a separate selection of runs of its own dataset.

4.2 Global Event Selection

First, because of the detector acceptance, we made general cuts over all events. We require the reconstructed collision vertex (by BBC/ZDC) to fall in between +/-30cm. To make maximum yield of jets, we use those events that fired the ERT trigger mentioned in Sec.3.3.3.3 in Cu+Cu and p+p datasets. This is done by selecting the desired flavor of production data, which are categorized according to different types of triggers each event fired.

For p+p collisions, the purpose is to make a precise measurement of jets physics in vacuum. The good understanding of this physics will be a backbone of our AA collisions measurement. To achieve this purpose, we need to keep as much cross-section as possible. Hence we will keep any p+p events in our statistics as long as it satisfies the run-QA .

For AA collisions, our main purpose is to study the effect of media over passing jet partons. We divide our AA events into centrality bins after the run-QA step. Because the most central collisions (smaller impact parameter or larger T_{AB} 3.2.4) contain higher per-event trigger yield, we can make finer binning over them. This give the advantage that events inside a narrower bin is more similar in geometry, while we can still keep enough statistics in this bin. On the other hand, the peripheral events has lower per-event trigger yield, the more peripheral bin is usually wider.

Run QA is performed to minimize the effect of fluctuation, by setting cuts on averaged event information over the whole run. This averaging of the whole run help avoid loss of those rare event that truly contains the physics we are interested in (such as hard-scattering). These averaged event information are plotted on a run-by-run basis, and we calculate the threshold based on such a plot. If one run has its variables out of threshold, the whole run has to be thrown away.

The threshold can be decided in more than one way. One way is to directly compare between runs. For example, we assume under same collision systems, the mean p_T per event, if averaged over the whole run, shall be approximately same among all runs. Then we can throw away those runs of a too high or too low mean p_T as in Fig.4.1. The other way is to plot distributions inside each run. For example, the distribution of centrality and reaction plane (RP) is believed to be purely random and has to be flat. It's therefore reasonable to throw away a single run if its centrality/RP distribution deviates from a flat line. A typical "bad" run decided by this QA is shown in Fig.4.2. Of course, this kind of quality check shall be done in the min-bias data of PHENIX. Otherwise we can bring detector bias if we use the data triggered by the same detector that we want to analyze later.

The lists of good runs used in my analysis are mainly decided by the analysis taxi operation if the code is run by analysis taxi 4.4.2.

4.2.1 Event Selection Thresholds

Collision vertex: $|getBbcZvertex|$ <30cm

Minbias Au+Au: minbias(BBC) events of Run4 Au+Au 200GeV.
ERT triggers Cu+Cu: ERT-trigger events of Run5 Cu+Cu 200GeV.
ERT triggers p+p: ERT-trigger events of Run5 and Run6 p+p 200GeV, must fire ERT4x4b or ERT4x4c live trigger.

Conditional hadron:
As we mentioned in Sec., we also need a high p_T charged particle in the same event that we select high p_T π^0 trigger from, if we are doing "2+1" correlation. The absolute value of relative azimuthal angle between this hadron and the trigger π^0 is larger than $\pi/2$.

4.3 Single Particle Selection

4.3.1 Charged Particle Selection

Charged particles are reconstructed as DC/PC tracks in Sec.3.3.2. The presence of conversions and fake tracks (ghost) requires we make a quality cut on each single charged track. The first step is from DC/PC1. As we mentioned in Sec.3.3.2.1, DC has 3 set of planes: X1 and X2 for $\phi-$resolution, and UV for z-resolution. Each track will be assigned a 6-bit word to represent its basic quality.

From low to high, each bit means:

bit 0: This track has sufficient X1 hits,

bit 1: This track has sufficient X2 hits,

bit 2: This track has UV information,

bit 3: This track has a unique set of UV hits,

bit 4: This track has matched PC1 hits (falling within the window of the DC track's projection to PC1),

bit 5: This track has a uniquely matched PC1 hits.

In the actual reconstruction there are pre-set quality requirements, and there won't be arbitrary combinations of all bits in track quality as shown in Fig.4.3. For example, a DC track has to contain both X1 and X2 hits to be reconstructed. This is because the DC has a higher resolution in $\phi-$direction than in $z-$direction. So we include in the analysis all tracks quality > 7. This set include all the combinations of track qualities that have: 1) sufficient X1 and X2 hits, and 2) UV hits and 3) matched PC1 hits.

Also, it's possible that a track hits the edge of DC detector and cross out the side boundary, and thus unreasonably reconstructed. This can also bring unexpected error to our charged efficiency calculation. To avoid this case, we required a fiducial cut, so that tracks hitting the edge of DC/PC3 won't be included in my analysis.

The cuts applied in my analysis are:

West arm: -0.54 $< \phi_{DC} <$ 0.92

East arm: 2.25 $< \phi_{DC} <$ 3.65,

Zed$< 75cm$

the0$<$ 0 (the reconstructed θ of tracks at collision vertex).

ϕ_{DC} and Zed are the $\phi-$ and $z-$ coordinate of hit position on DC, respectively.

If a track passes DC/PC1 quality cut at first step, it tends to be a real charged particle instead of "ghost", such as the random combination of DC/PC1 hits. However, this doesn't guarantee it's good for usage yet. For example, conversion tracks may be reconstructed with an incorrect momentum information, because the current reconstruction assumes all charged tracks come from collision vertex. Usually this means a much higher momentum than reality, possibly by a decay or conversion.

To reduce such tracks, we include outer PC layers in our quality cuts. Only PC3 are used in our analysis because PC2 was installed at only the west arm. The method is to calculate how the reconstructed charged track at DC/PC1 will propagate in the magnetic field remnant, and project this track to PC3 panels. The projection is then matched to most nearby "real" PC3 hit, within a very broad window (to ensure a matching happens). The difference between projection and hits will then be plotted in both $\phi-$ and $z-$ direction (called pc3dphi and pc3dz, respectively) and fitted in Gaussian. This Fig. 4.4 shows a sample of the PC3 matching distribution, and how to determine the cuts.

The distribution of this matching deviation pc3dphi/pc3dz is momentum and multiplicity (thus centrality) dependent in a magnetic field. And random combinations between DC/PC1 hits and PC3 hits will make noise to their distributions. So in practice, we will first divide the pc3dphi/pc3dz distributions into different p_T and centrality bins. Then in each bin, both pc3dphi and pc3dz will be fitted by double Gaussians, since real matching and random combinations will each make a Gaussian distribution. The Gaussian widths of random combinations can be derived by swapping North/South sectors of DC/PC1 to PC3 correspondence. That is, we swap the sign of $z-$ coordinate of south PC3 hits and match them to the projection of north DC/PC1 and vice versa. Because there can't be any real physics between such combinatorials,

the shape of such "swapped" matching deviation (called spc3dphi/spc3dz) shall be the pure background combinations.

Then both pairs of Gaussians are normalized and written into data. These number of σs are called pc3sdphi/pc3sdz (for "real" matchings) and spc3sdphi/spc3sdz (for "swapped" matchings). Naturally, such distribution shall always be a normal Gaussian, centered at 0 and σ =1, see Fig. 4.5

In our following analysis, we require a $3\sigma-$window in PC3 matching. That is, we require the $\sqrt{\sigma^2_{\Delta\phi} + \sigma^2_{\Delta z}} < 3$. This will include most "real" charged tracks, while efficiently remove those obviously unreasonable, such as conversions. Because the matching is momentum dependent, if the momentum information is updated, the σ values also has to re-calculated. This is done mainly through recalibrators in Sec.4.4.1.

Also we need to exclude electrons. This is achieved by projecting charged tracks to RICH radiation rings. Any charged pion/kaon/proton with a $p_T < 4.9GeV/c$ won't radiate Cherenkov light in the PHENIX RICH detector3.3.3.2, and has thus 0 coincidence with RICH radiation rings (n0<=0). This works as a good cut for our charged tracks below this p_T threshold. For those above this pT threshold, pions will first radiate, and we need alternative cuts to identify them from electrons. One method is to look at the EMCal energy deposit of this particle comparing to its momentum, the so called e/p ratio. The systematic error due to this e/p cut will be discussed further in later analysis.

Because the single-particle spectrum analysis has not finalized the cuts, we won't apply their efficiency result directly. Instead, we will produce our raw spectrum and compare it with the published physics spectrum from PHENIX. The ratio of these two will bring us the charged particle efficiency, after being corrected by $\phi-$ and $\eta-$ acceptance. This was done primarily for Cu+Cu. Since small centrality dependence was observed ($< 10\%$), we apply a uniform efficiency in our Cu+Cu analysis without centrality dependence. We also use the same efficiency in our $p + p$ data analysis. To cover the centrality dependence of efficiency corrections (i.e. if we use real p+p and a centrality dependent Cu+Cu efficiency), we apply a 10% systematic error to each of the Cu+Cu centrality bin and p+p due to the uncertainties

in the efficiency.

The general cuts for single charged particles are:

quality > 7

n0<=0

the0>=0

$spc3dphi^2 + spc3dz^2 < 9$

-0.54 $< \phi_0 <$ 0.92 or 2.25 $< \phi_0 <$ 3.65, and Zed$< 75cm$

4.3.2 Photon Selection

Since we use identified high-p_T π^0s as trigger to tag jets, it's important to reconstruct these π^0s first. Because of its short life-time ($\sim 10^{-16}s$) and highly-probable decay channel (99% $\pi^0 \longrightarrow \gamma + \gamma$), we use photon pairs to reconstruct π^0s.

As we mentioned before in Sec.3.3.3.1, the photons entering EMCal detector will produce electro-magnetic shower, a spray of electrons and photons. These electrons/photons will radiate light in the EMCal material and be collected by EMCal towers. Usually one particle will create a shower that is collected by more than one towers. Thus we will loop through the towers, find the energy peaks (center tower of shower), and form clusters using towers around each energy peak.

Because the energy distribution among towers of the same cluster (photon/hadron) will drop sharply from center to edge, we use 21 towers, 5x5 without 4 corners, to reconstruct one particle. Photons usually need all 21 towers to collect almost all the energy, while hadrons may need only the central 3x3 towers. Since we don't know whether it's photon or hadron in the first stage of data reconstruction, we will use two energies to mark each cluster: e assuming it's a hadron (based the sum of energy of all towers), and ecore assuming it's a photon (based on the sum of energy of central 9 towers). The towers are numbered from center to edge, and tower 0 is always the most central one.

Then we need to evaluate the quality of each cluster. The existing parameters include:

1) Energy distribution shape: We use χ^2 (3.3), the difference between measured and expected cluster shape, for PbSc. For PbGl, because the neighboring Cherenkov Counters may not give consistent response, it takes a more complex calculation to give out a similar shape parameter equivalent to χ^2. We use $\chi^2 < 3$ cut for photons in Fig.4.6. Another advantage of this χ^2 cut is to remove overlapping PbSc clusters, which will give a large χ^2. In our dynamic region where most $p_T^{\pi^0} < 10$GeV, it's rare for two photons from same π^0 to overlap at EMCal. So overlapping clusters can be viewed as pure noise, such as random combination of two un-correlated photons.

2) Time-of-Flight (TOF). The massless photons/electrons shall reach the EMCal (Distance = ∼5m from collision vertex) within $D/c = 20ns$. The hadrons within the same p_T region will arrive later. It then takes both particles a finite time to produce EMCal shower and radiate light. This means the TOF = t_{EMCal} - t_{BBC} will have a distribution as a sharp peak below 100ns and a long broadened tail. In our analysis, we are using only the lower limit of TOF to cut off unreasonable EMCal response (TOF> $-300ns$) Fig.4.7, and rely on the shape cut to remove those hadrons from our π^0 samples. These unreasonable EMCal responses are usually from either tail of last bunch cross, or the hot channels of electronics.

3) The matching between DC or PC3 projections and EMCal clusters. This projection is made by connecting a straight line between collision vertex and DC or PC3 hits, then projected it straightly to EMCal. A close matching between hits and EMCal clusters possibly mean this EMCal cluster is from a charged hadron or conversions, and should be removed. As we introduced earlier in Sec.4.3.1, such matching between hits of same particle is a narrow Gaussian shape. On the other hand, a real photon shall be only randomly matched to DC/PC3 hits. Such Emcal-PC3 matching is a very broad Gaussian shape. Hence, if we cut only those EMCal clusters whose matching is close to 0, we shall lose very few "true" photons while remove hugely the charged hadrons.

This "charge-veto" cut has a similar function as our χ^2 cut. In fact, during our analysis, we compare the π^0 spectrum before and after matching cuts in Fig.4.8, with all other cuts

remaining the same. The comparison shows basically the same S/B ratio within our invariant-mass window. We concluded the tail of emcal-pc3 matching cut is from random combinations between EMCal towers and PC3 hits, and we don't really need them if other similar cuts already exist, such as $\chi^2 < 3$.

4) Dead/Warn map cut. The EMCal tower electronics sometimes doesn't work fully well. One tower may become too hot or dead. If a photon comes of such tower, it's not to be trusted. So we make a dead/warn map of EMCal towers, and require that any photon we used cannot be from this map. The making of this dead/warn map is explained in more details at Sec.4.4.1.

The cuts for single photon are listed here:

chi^2 <3 for PbSc or equivalent for PbGl,

EMCal time-of-flight $> -300ns$,

photons can't be from EMCal areas marked as warn/dead,

No PC3 matching cuts applied in this analysis.

4.3.3 π^0 Selection

We use high-p_T π^0 to tag the jets because it's the highest-p_T-identified hadron measurable in PHENIX at this time. To make advantage of this, we need to select π^0 to achieve as much high signal-noise ratio (S/B) as possible, while still not losing too much signals. The photon selection rules in Sec.4.3.2 has provided us a relatively clear working basis.

It's important to remember that although π^0 has a very short life time, it's still finite. But our photon reconstruction has always assumed all photons come directly from the collision vertex. So these two factors, the life time of π^0 and the systematic error of collision vertex itself, add to our reconstructed π^0 mass error. A typical distribution of invariant mass of photon pairs is as in Fig.4.9

Note there are more kinds of errors included in Fig.4.3.3. For example, the energy measurement of photons can be dispersed from real values (see section 4.4). There can be random combinations of photons whose invariant mass fall nearby the particle-data-group (PDG) pub-

lished π^0 mass. Therefore, instead of using the published π^0 mass and error directly to cut our photon-pair invariant mass spectrum, we need to determine the cuts ourselves. The standard method in PHENIX is to fit this spectrum using addition of two shapes: Gaussian as the "real" π^0 plus a 3rd order polynomial as combinatorial background . The center and σ of Gaussian varies with p_T. In practice, we made a fixed cut of $0.11 < \pi^0_{inv-mass} < 0.15\text{GeV}/c^2$, which is roughly a 2.5σ cut. At the high p_T (>4GeV/c) region we studied, the peak positions and Gaussian widths are mostly stable and this is a safe cut.

To remove the random combinatorics, another method is to apply the asymmetry cut. At high-p_T region, most "fake" π^0 come from the random combination of a high-p_T photon (may come from a real high-p_T π^0) and a low energy photon from unknown source. We define asymmetry as in Equ.4.1:

$$asymmetry = |\frac{E_1^{photon} - E_2^{photon}}{E_1^{photon} + E_2^{photon}}| \tag{4.1}$$

We apply an asymmetry< 0.8 cut to all π^0s. Take a p_T =4GeV/c π^0 for example, this means the smaller-energy photon has energy at least 0.4GeV. For those photon whose energy falls below this cut, they are possibly from decay of a lower-energy π^0, or from thermal radiations at even lower energy region in rare case.

In the high-pT region we are looking at, the pair of photons decay from π^0s are most likely to fly into the same EMCal sector. On the other hand, random combinatorials between photon from different EMCal sector/arm can still fall into the invariant mass region. So we require that both photons be used in π^0 reconstruction (see Sec.4.3.3) must come from same EMCal arms. The purpose is to select good π^0s for our jet-tagging triggers, while not losing too much signal.

Meanwhile, since we are using ERT-trigger data in Cu+Cu and p+p, it's important to estimate correctly the percentage of hard-scattering cross-section such a trigger can record. Doing such a job requires our hardware trigger is actually fired by the high-pT particle. So we require our high-pT π^0 is the one that fired the ERT-trigger, via its decay photons.

The cuts for π^0 are listed here:

$0.11 < mass < 0.15$GeV,

asymmetry < 0.8,

both photons come from same arms,

At least one of the pair of photons must be from the same EMCal module that fires the ERT trigger in that event.

4.3.4 Pair Cut

If both trigger and associated particles are of same type, i.e., from exactly the same set of detector components, they may share detector hits between them during data reconstruction. This will produce "fake" correlation peaks. To avoid this, we usually need to apply additional pair cuts using detector parameters, such as $\phi-$ and Zed- coordinates of DC hits. However, in our analysis, the trigger π^0 and associated charged tracks are measured from two sets of detectors seperately. So we conclude it's safe to proceed without explicit pair cuts, as long as appropriate quality cuts are applied each.

4.4 Calibration

It's important as an experimentalist to remember we can never get the exact measurement at the first stage. For example, The DC wires may not locate in the exact position we expected. This will bring error to momentum of charged tracks. The EMCal towers may not have the same gain as in the manual, so our photon energy and following π^0 mass may deviate from published values (actually they did as shown in Fig.4.3.3). And there will always be hot and dead area of detectors' electronics in the real world. To minimize the effect of all these factors, we need to apply recalibrations to our reconstructed dataset before any serious physics can proceed.

In a big experiment such as RHIC-PHENIX, the data doesn't finish all of its calibrations at first stage. Instead, it undergoes at least two stages before reaching its final form: the primary data (PRDF) and the useable data (DST). And there will be two forms of calibrations, the

on-line and the off-line ones, respectively.

On a periodic-timely basis, the on-line calibrations are executed during the intervals of beam stores. These calibrations include the zero-field DC position calibration, EMCal laser scan and gain correction, TOF electronics recalibration, etc. The results will be recorded into the recalibration database and later applied to data reconstruction, the process from primary data form (PRDF) $\longrightarrow$ to user-readable data from (DST).

On the other hand, off-line recalibrations are calculated after the useable form of data (DST) are available. This means they will be applied real-time when we read from DST data. Of course, these off-line recalibrators has to be run before our analysis code see the data. This process is called the "recalibrators" in the following chapters. Another option is to re-generate DST data with the recalibrators running. In such a case, the recalibrators will be updated after data reconstruction so that the same recalibrator won't be run overlappingly later when we do analysis over DST.

4.4.1 Recalibrators

All recalibrators have to be applied in a certain order. Many detectors rely on results from other detectors, so one recalibrator usually uses information from specific detectors that are recalibrated by other recalibrators. For example, the recalibrator for PC3 matching (Sec.4.3.1) is momentum dependent and has to be run after the recalibrator for DC. Hence we need to run the recalibrators in a well-designed order. We now introduce the recalibrators in the order they are arranged to run.

First we need to care about recalibrators for global event information. 1) As there can be beam remnant in the empty bunch of each beam, they may produce noise at wrong bunch time triggers. This has to be removed by the bunch-crossing recalibrator. 2) Our global event information, such as collision vertex, is from BBC (Sec.3.2.2) using strict time calculation. Also, the timing signal is necessary for all particles in our analysis, and BBC timing (BBCt0) works as a basis for all the other Time-of-Flight detectors. All detectors will calculate their TOF (if available) as $t_{detector}$ - t_{BBC}. So the 2nd recalibrator is the BBC timing (BBCt0).

Then, there are always hot/dead wires/towers in our detectors. Both will affect our efficiency calculation, and hot electronics can easily produce "fake" signals. We apply recalibrators to mark these hot/dead areas, and tracks/photons from these areas are excluded from the analysis. The hot/dead areas are decided by the per-event multiplicity basis over the whole dataset (after run-QA), with properly-selected upper and lower thresholds.

Dead-warn map:
In PHENIX, the general EMCal dead-warn map is included into recalibrators. These maps are calculated by EMCal experts, written into database and later called by the recalibrators. Beyond that, recent runs have extra warn-dead maps if we are looking at specific dynamic ranges:
Run5 Cu+Cu 200GeV: Use the dead-warn map from Christian Klein-Boesing made the dead-warn map, as in Fig.4.10
Run5 and Run6 p+p 200GeV: Use the dead-warn map from Kensuke Okada.

In the Fig.4.10, each of the eight histograms shows warn-dead map of one sector of EMCal detector at Run5, in the geometrical order. left column is of west arm, right column is east arm, and from bottom to top is sector 0 to 3. In each histogram, white points are defined as "bad" towers, and deep-brown points around them are defined as "next to bad" towers. Both these two categories are considered as "bad" in our analysis.

We also commit into CVS the dead-warn map for Run 2005/2006 p+p. This information is from Kensuke Okada. Each line in the map file is a tower-id followed by its status id. Here we mark only those tower with id = 1 as "good". All others are marked as "bad".

Finally we come to detectors for specific particles. We need 2 of the 3 variables: momentum, mass (static), energy, to identify the particle. Both DC and TOF (from EMCal or specific TOF detector) can provide us this information. In practice, we calculate information needed for recalibrators in such an order:

1) The TOF will recalibrate its timing signal using the BBCt0 as working basis. As we

mentioned, the "real" photons shall arrive the TOF at a predictable timing scale, and we explicitly know the response time of TOF. So we can plot the distribution of TOF, mark the peak of "real" photons, and correct it back to the expected timing.

2) Then we need to calibrate the momentum of charged particles from DC. This is done by summing information from DC and TOF. With momentum (from DC) and speed (from TOF) already known, we can calculate the rest mass of each charged particle. This distribution shall have peaks at well-known particles such pion/kaon/proton. Among them, the proton is our primary selection because it's stable, and its mass is precisely measured. The deviation of measured proton mass from published values will be used to correct DC momentum, correlated to an error within 2% level.

3) The EMCal needs an energy recalibrator for photon measurement. This job is done in two steps. The first step there is a tower-by-tower (in the same sector) then sector-by-sector of whole EMCal flattening work. The object is to make tower-specific coefficient so that each tower has the same average energy per hit over the whole calendar year Run. This is to remove the fluctuation of energy measurement due to difference in gain of each tower. The second step is done by the π^0 reconstruction in 4.3.3. We plot the π^0 inv-mass spectrum, as a function of both photon energies and EMCal sectors. This gives us an energy-dependent coefficient for correcting photon energy measurement.

All recalibrators have their correction parameters recorded into database. In the later physics analysis, these recalibrators will be run before our private analysis code and read parameters from database, correct the data in the memory, and provide us a clear DST dataset.

4.4.2 Master Recalibrator and Analysis Taxi

As you can expect, these recalibrators are convoluted and has to be run in a strict time order. A lot of times, this can be a hard job for individual analyzers. This became more serious when our dataset volume increases into more than our hard-disk can contain. Because DST data has be grabbed from tape, any error in processing data means waste of resources. Due to this, we are now applying a framework of recalibrators, called "Master Recalibrator". All

recalibrators are fit into this framework, and the process of calling them become transparent to individual analyzers.

Also because of the huge dataset volume and time-cost process of grabbing data from tape, it becomes necessary to organize analysis jobs in a more efficient way, or "centralized" as called. The existing of Master Recalibrator makes it's possible. Now this organized way is called "Analysis Taxi", as each analyzer submit their jobs, specifying the input data source and output destination they desire, and the administrator (the "Taxi Driver") will organize these jobs. This doesn't mean one analyzer can't run his/her own job, of course.

When recalibrators have been stabilized for specific data source (calendar year/collision energy/collision particle species), it is feasible for the DST data to be re-produced, applying all the recalibrators. The recalibrators will then change themselves to reflect the change of data source, since they can't do a "double-correction". Because of the existence of Master Recalibrator, this process is supposed to be transparent to individual analyzers.

All code of analyzer's has to be committed into CVS system so that the analysis taxi can compile and run over them.

The version of analysis taxi used in my analysis are listed here:
All data are generated by modules running at PHENIX analysis taxi 65 (Sec.4.4.2). That means corresponding recalibrators were called by PHENIX Masterrecalibrator at that time in a proper order, and some runs were abandoned by certain recalibrators, such as bunch-crossing recalibrator which throws away mistakenly-marked bunches.

Source code is at CVS:
offline/AnalysisTrain/UltraLight
offline/AnalysisTrain/CabanaBoy
offline/AnalysisTrain/Hua Correlation
Running macro is at CVS:
offline/AnalysisTrain/pat/macros/Run ULpi0hRP CuCu(pp).C All runs processed by each taxi can be found on offline taxi page:
`https://www.phenix.bnl.gov/WWW/offline/wikioff/index.php\?title=AnalysisTrain`

Run 4 Au+Au 200GeV wasn't run over taxi. Instead it's all disk-resident min-bias statistics, about 900M events.

Run 5 Cu+Cu 200GeV Analysis Taxi 65, 492939109 ERT events

Run 5 p+p 200GeV Analysis Taxi 65, 1980653410 ERT events

Run 6 p+p 200GeV Analysis Taxi 65, 3123946290 ERT events

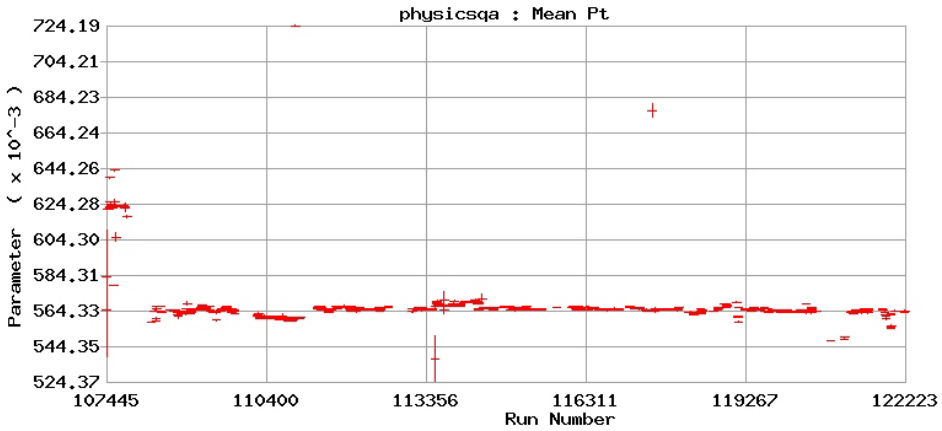

Figure 4.1 A run-group threshold plot generated by the calibrators database. We select the timing period (via run-numbers) and plot the run-mean-pT distribution. This distribution can be further used to decide the threshold cut.

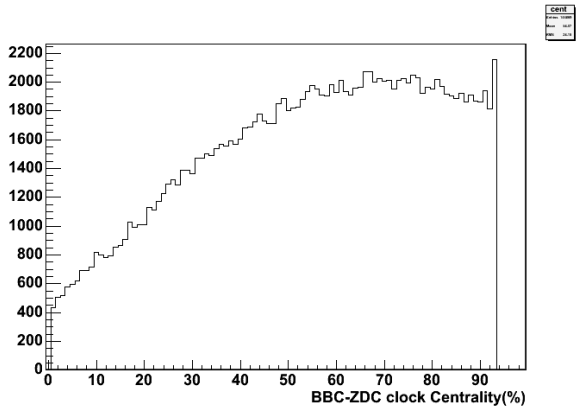

Figure 4.2 A typical "bad" run is shown here. It's centrality distribution is obviously deviated from a flat line.

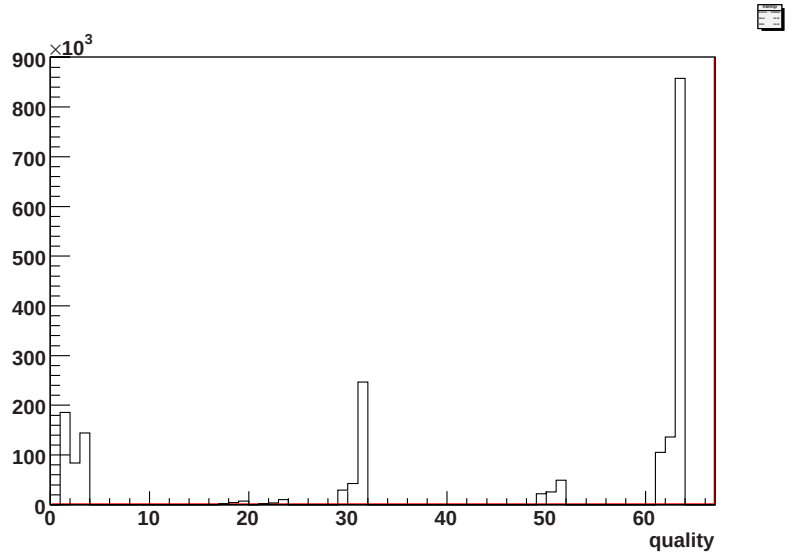

Figure 4.3 An example plot of quality distribution of DC/PC1 tracks. Note a track has to meet certain thresholds to be included into data reconstruction. So the distribution plot doesn't have statistics on all bins.

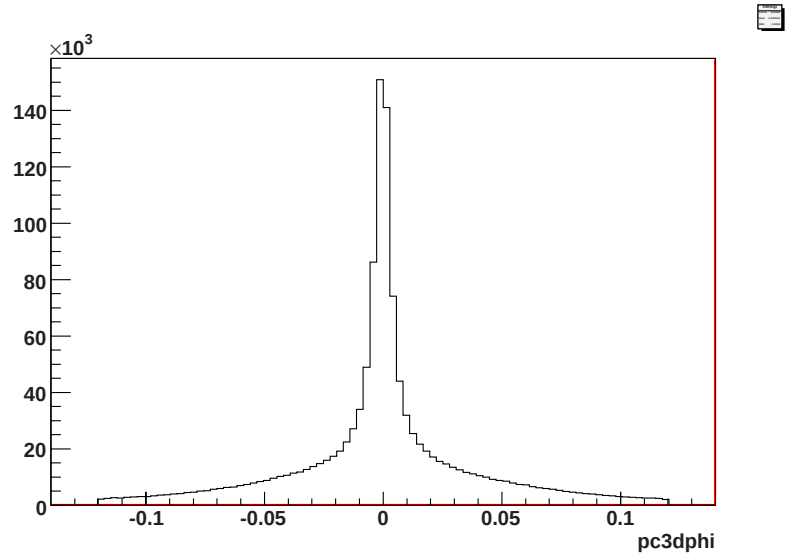

Figure 4.4 An example plot of PC3 matching distribution of DC/PC1 tracks.

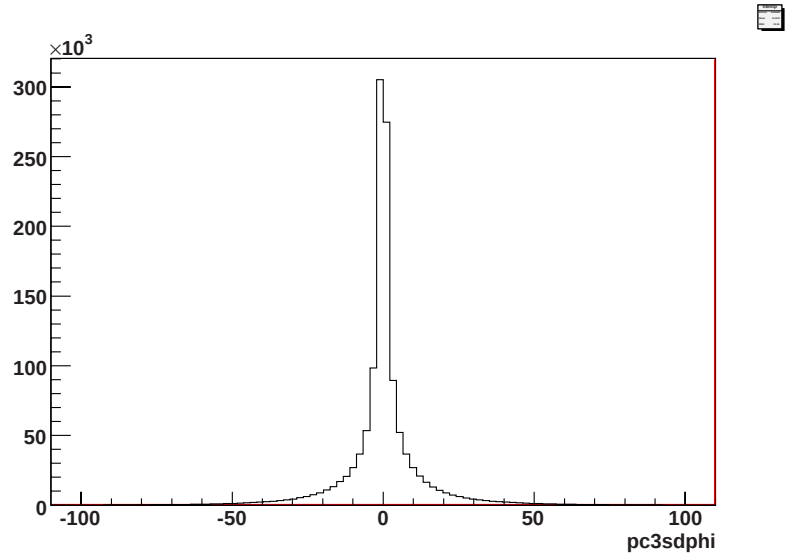

Figure 4.5 An example plot of PC3 matching σ distribution of DC/PC1 tracks.

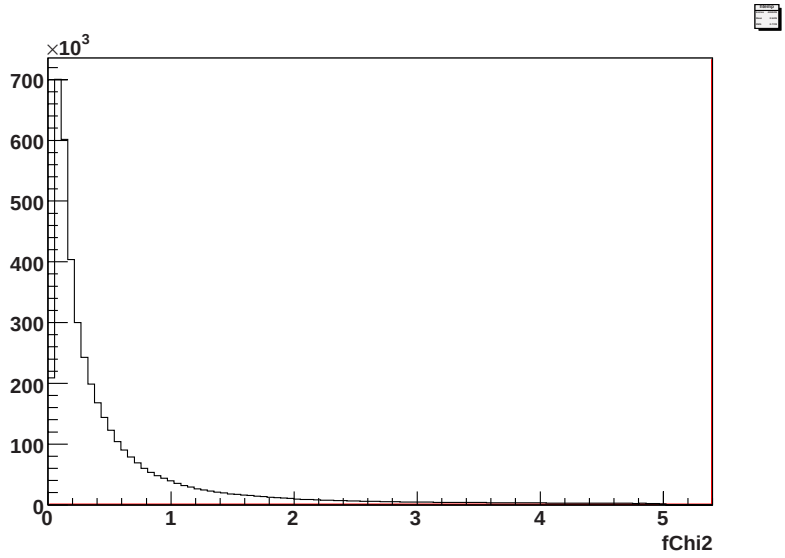

Figure 4.6 An example plot of EMCal χ^2 distribution.

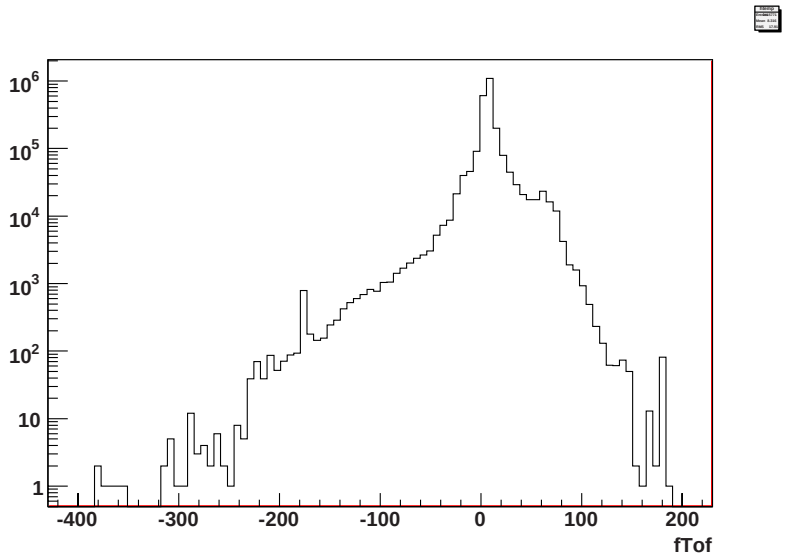

Figure 4.7 An example plot of EMCal Time-of-Flight distribution.

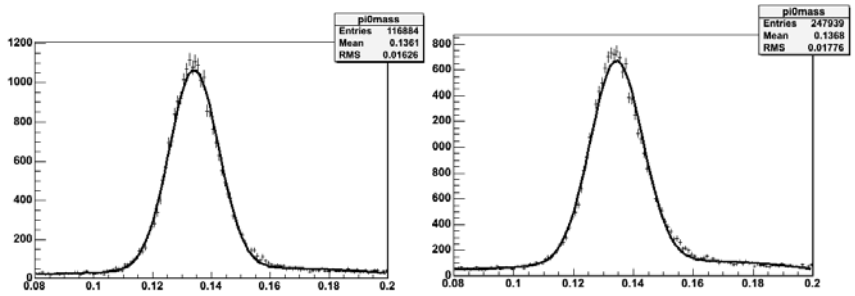

Figure 4.8 We compare the S/B with or without the EMCal-PC3 matching. The other cuts to photon clusters are the same. S/B ratio isn't changing in this plot with/without charge-veto cuts.

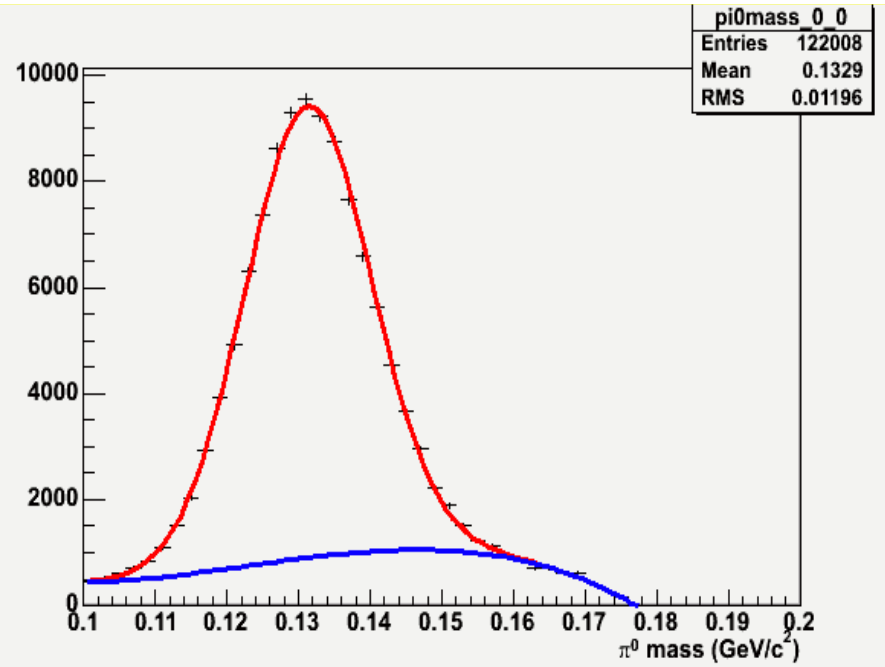

Figure 4.9 We show the invariant mass of photons pairs in this plot. The cross-markers in each bin is the actual statistics we have and will be summed (within the mass window we decided later) to get the total number of π^0 triggers. The blue line is the fitted 3rd-order polynomial as background, and the area between red and blue is the Gaussian shape fitted as the "true" π^0 signals. The ratio of "true" to background is the S/B we propagate later to get systematic error on our π^0 yield.

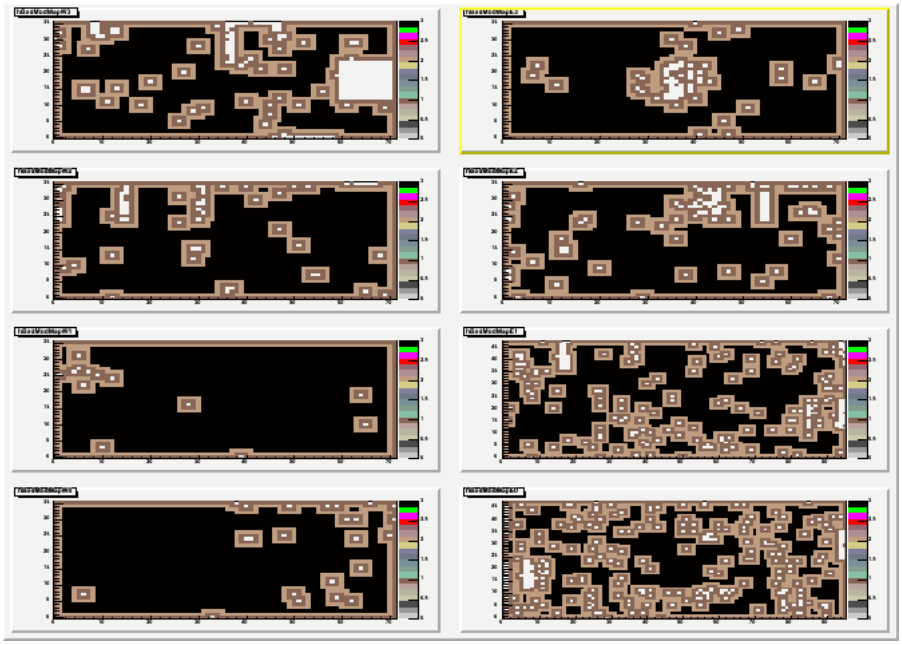

Figure 4.10 The Run 2005 Cu+Cu 200GeV EMCal dead-warn map from Christian Klein-Boesing. Each of the 8 sub-panels represent one EMCal sector. Each tiny squares in the sub-panels represent one EMCal tower. The white ones are bad (either hot or dead), and dark-brown ones are next to bad. Both the white and dark-brown categories are rejected in my Cu+Cu analysis.

CHAPTER 5. Physics Results

This chapter is about the jet correlation analysis work I have been doing in PHENIX. The jet correlation is defined in chapter.2. I have been using the high-pT π^0 as trigger and charged hadrons as associated and/or conditional particles. The exact cuts are summarized in chapter.4. The object of my correlation analysis work is to use the jet as the probe of medium. The path-length of jet traveling in medium is controlled by centrality, reaction-plane dependence, and the new "2+1" correlation.

5.1 Run 2004 Au+Au

The correlation code was first used on the PHENIX-RHIC 2004 Au+Au data. We run the π^0-h correlation, and observe its reaction-plane dependence. Here we show a typical correlation function evolving with centrality in Fig.5.1. The same plot was shown in the introduction chapter. In each panel from left to right, we show the jet functions after subtraction of flow background, from central to peripheral Au+Au events respectively. We can see a clear evolution of jet shape on the away-side. The most peripheral Au+Au away-side jet is still a peak, even if not exactly the same as p+p reference. When moving to central Au+Au events, the away-side jet signal shows a clear broadening. At the most central Au+Au events, new structure at away-side appears. This structure looks like a "mach-cone", where a concave shape shows around $|\Delta\phi| \sim \pi$. Possible mechanisms of "mach-cone" are parton-medium interactions, including the gluon radiation in medium, shock wave, and random momentum kick of parton. All this can be used to constrain theoretical models of parton energy-loss in medium. Meanwhile, the near-side jet also shows the dependence on centrality, although maybe a smaller effect comparing to that of away-side.

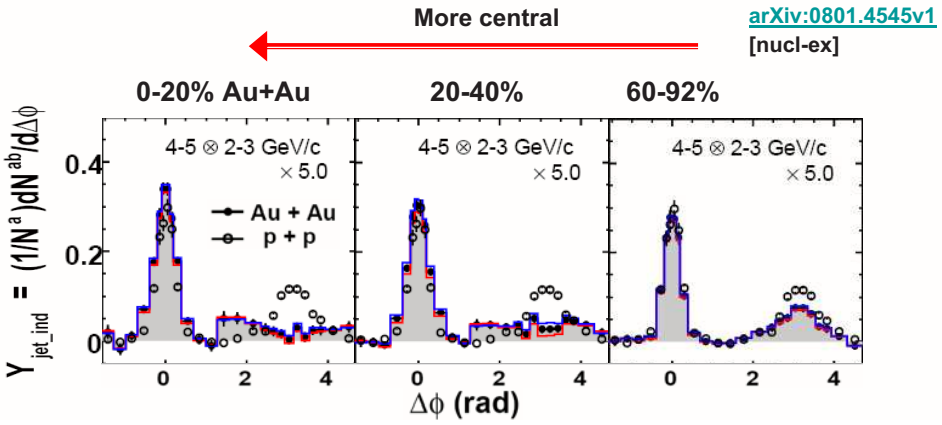

Figure 5.1 A typical plot of correlation functions. Each panel is from a different centrality Au+Au collision, while the same p+p correlation is in all panels as reference.

Therefore, it's important to quantify the shape of near/far -side as a function of path-lengths. We first extract the near/far -side widths to quantify the change of shapes, as a function of centrality, the first accessible control of path-length. We first quantified the far-side widths as function of trigger p_T in Fig.5.2 and associated p_T in Fig.5.3. In these plots, the centrality is plotted in unit of N_{part} 3.2.4, so it's easier to compare with p+p/d+Au reference on the left-end of each plot.. Although it might be true that this far-side width depends on N_{part}, the large error-bars make it hard to make a conclusion. The errors come both from statistics and systematic (multi-parameter fitting, ZYAM 2.1.5).

Summary of sources of systematic errors:

• Error of v_2. This include the error of reaction-plane (resolution) and the error of v2 extraction. The v2 error is propagated by varying the flow shape by $1-\sigma$ of v2 and re-derive the correlation function and Gaussian fitting.

• Error of ZYAM. This means we vary the foreground shape by $1-\sigma$ of its flat line and re-derive the correlation function and Gaussian fitting.

• Error of π^0 mass. This error is 2%, and is derived by varying the invariant mass window and compare the S/B of π^0.

• Error of efficiency and centrality smearing. This is error is about 10% in the correlation function, and is propagated to the Gaussian fitting.

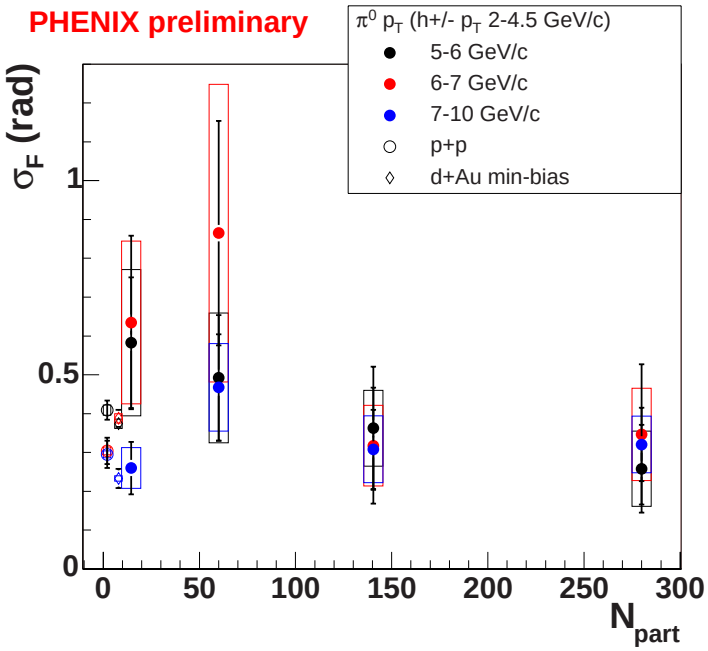

Figure 5.2 Far-side peak Gaussian shape width as function of N_{part} and trigger pT. Associated pT is fixed to be [2, 4.5]GeV. We also include p+p (91) and d+Au (87) data as reference on left-side of plot. Error lines are statistical errors and error boxes are systematic errors.

Then we used another method to quantify the far-side shape, the **RMS**. Since this RMS will fluctuate hugely in case of any negtive entries, which is almost in-evitable in a ZYAM process as we explained in Sec.2.1.5, we calculate the far-side RMS within a specific range $|\Delta\phi - \pi| < 1$, and fix the mean to be $\Delta\phi = \pi$. Again, we show the far-side RMS as function of trigger p_T in Fig.5.4 and associated p_T in Fig.5.5. Still, it's possible this far-side RMS is N_{part}

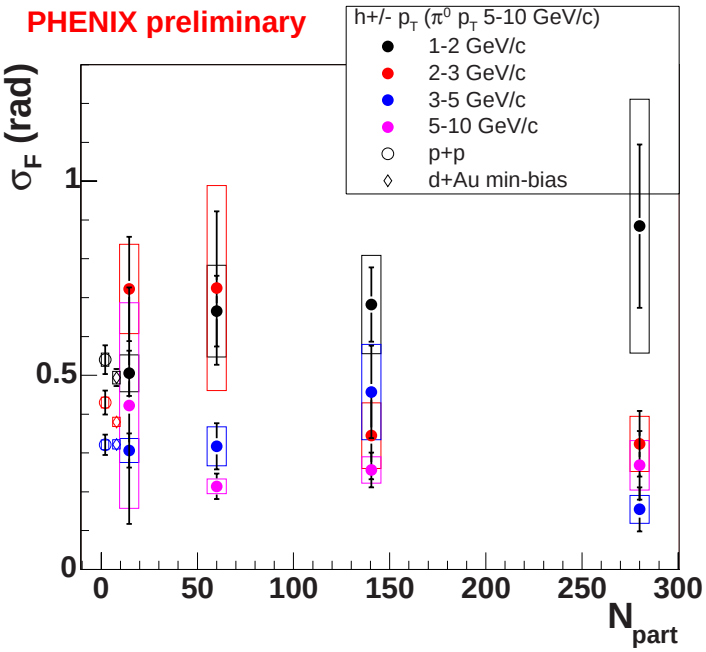

Figure 5.3 Far-side peak Gaussian shape width as function of N_{part} and associated pT. Trigger pT is fixed to be [5, 10]GeV. We also include p+p and d+Au data as reference on left-side of plot. Error lines are statistical errors and error boxes are systematic errors.

dependent, but the large error-bars make it hard to make a conclusion. The errors come both from statistics and systematic (multi-parameter fitting, ZYAM).

The statistics of PHENIX Run 2007 200GeV Au+Au is more than 3 times of the Run 2004 Au+Au data we used in this analysis work. We expect the far-side shape of high-pT jet correlation will give us a better understanding on N_{part} dependence, with this largely improved statistics.

Now we go to the near-side shapes, which are more stable. First we show the near-side widths for different trigger p_T as a function of N_{part} in Fig.5.6, and for different associated p_T in Fig.5.7. The errors come both from statistics and systematic (multi-parameter fitting, ZYAM). While fluctuations still happen amount various Au+Au centralities, we observe that p+p/d+Au widths are systematically higher than those of Au+Au under same p_T regions. This is an interesting observation and could lead to the possible "surface-bias" assumption. However, the errors are usually at the same or even higher level compared to the change of

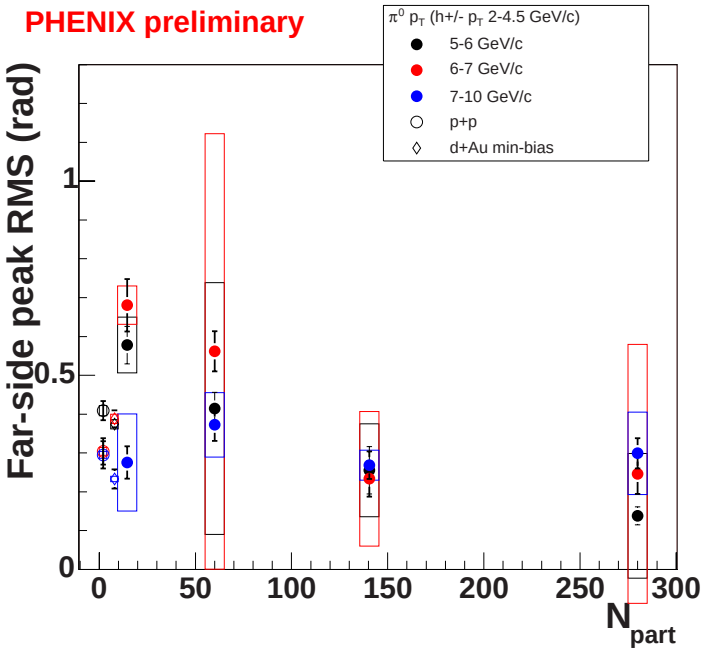

Figure 5.4 Far-side peak RMS $|\Delta\phi - \pi| < 1$ as function of N_{part} and trigger pT. Associated pT is fixed to be [2, 4.5]GeV. We also include p+p and d+Au data as reference on left-side of plot. Error lines are statistical errors and error boxes are systematic errors.

widths. This prevents us to reach further conclusion. More details of jet shape as a function of pT and centrality was discussed in details in PHENIX paper (66).

Again, we expect the largely improved statistics of PHENIX Run 2007 Au+Au data will do great help on this analysis.

We also studied the near-side widths as a function of the reaction-plane defined in Sec.1.2.8.2. The reaction-plane dependent near-side widths are shown as a function of $|\phi - \Psi|$ (the tigger π^0 angle relative to reaction-plane), for different trigger p_T in Fig.5.9 and for different associated p_T in Fig.5.10. Because the limit of statistics, we are doing only min-bias Au+Au (0-92%) here. A typical correlation function evoluting with reaction-plane dependence is shown in Fig.5.8. The red/black lines in each panel shows the flow contribution and its error. The region between black dots and flow lines represent the jet signal.

At lower trigger p_T regions, the peak-widths seem to increase from in-plane to out-plane. At higher trigger p_T regions, the peak-widths seem to be flat from in-plane to out-plane. At

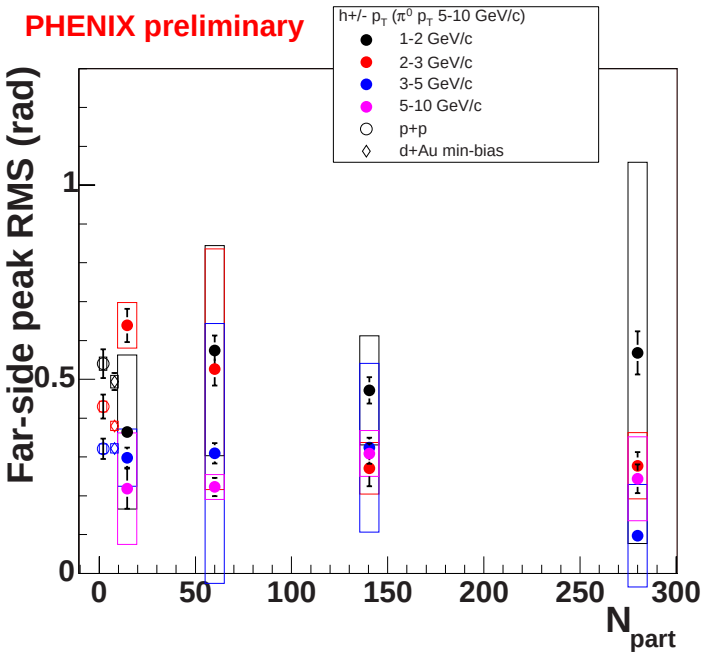

Figure 5.5 Far-side peak RMS $|\Delta\phi - \pi| < 1$ as function of N_{part} and associated pT. Trigger pT is fixed to be [5, 10]GeV. We also include p+p and d+Au data as reference on left-side of plot. Error lines are statistical errors and error boxes are systematic errors.

lower associate p_T regions, the peak-widths seem to fluctuate from in-plane to out-plane. It's possible that the lower p_T regions and higher p_T regions particles are statistically generated due to different physics mechanisms. However, the big error-bars prevents us to make further conclusion. One thing to notice here is that even the systematic errors, such as those of ZYAM, can be limited by statistics. For example, if the statistical error bars are too large, the process of ZYAM fitting will be unstable, as we explained in Sec.2.1.5. And systematic errors are also correlated with each other. For example, the resolution of reaction-plane can also affect the flow background and thus the ZYAM method.

In 2007, PHENIX-RHIC has collected much more statistics in 200GeV Au+Au collisions, roughly 3 times what we had in 2004. Also, the new reaction-plane detector has been installed and come to use at Run 2007, and reaction-plane resolution has been improved greatly. The reaction-plane dependent jet analysis are now being done, and some results by Wolf Gerrit Holzmann have been shown in QM08 (parallel talk by Hua Pei) and Winter-workshop 08

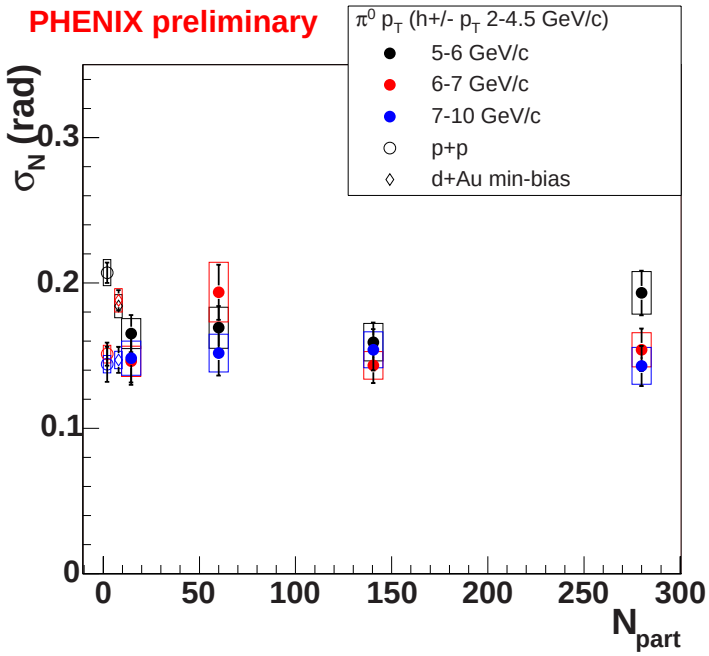

Figure 5.6 Near-side peak Gaussian shape width as function of N_{part} and trigger pT. Associated pT is fixed to be [2, 4.5]GeV. We also include p+p and d+Au data as reference on left-side of plot. Error lines are statistical errors and error boxes are systematic errors.

(Dave Winter).

5.2 Run 2005 Cu+Cu

In 2005 PHENIX-RHIC ran 200GeV Cu+Cu collisions. The statistics was improved, and we continue our analysis work on jet correlation.

Because Cu has only one third of nucleons as Au, the reaction-plane resolution of Cu+Cu is worse than that of Au+Au. This brings us difficulties while doing reaction-plane relevant analysis. The decision is then to use a new way, the "2+1" correlation we introduced before in Sec.1.2.8.1, to do the path-length control.

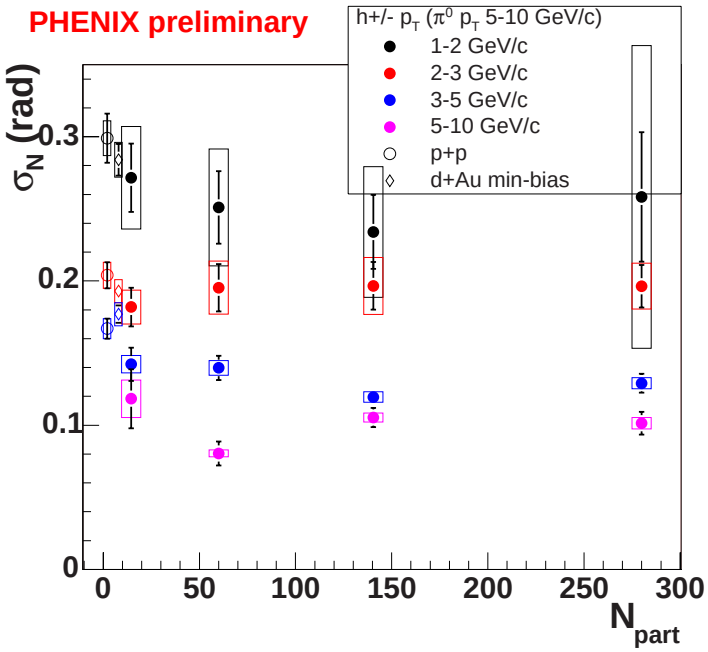

Figure 5.7 Near-side peak Gaussian shape width as function of N_{part} and associated pT. Trigger pT is fixed to be [5, 10]GeV. We also include p+p and d+Au data as reference on left-side of plot. Error lines are statistical errors and error boxes are systematic errors.

5.2.1 Result of p_{Tout}

Before we do this "2+1" correlation, we compare our Cu+Cu jet correlation to the p+p result. The object is to explain the existence of medium effects to jets before we make any actual path-length control. In the chapter of correlation, we define the near-side p_{Tout} in equation.2.17. And we know this near-side p_{Tout} is proportional to $sin(\Delta\phi)$, even bins of $\Delta\phi > 3\sigma$ can have non-trivial contribution. And p_{Tout} also has the advantage of combining contributions of a broad associate p_T range. We hope it's more sensitive to any change in near-side jet shape than the fitted Gaussian width σ we used in 2004.

The first results we have are encouraging. We show here the $p_{Tout,N}$ work of Cu+Cu in different centralities, and compare them to p+p. First it's the min-bias result in Fig.5.11. We see a clear excess at higher $p_{Tout,N}$ region, which indicate a broadening of jet shape in Cu+Cu. More centrality-bins are done, as in Fig.5.12, 5.13, 5.14. These plots have been shown in QM06

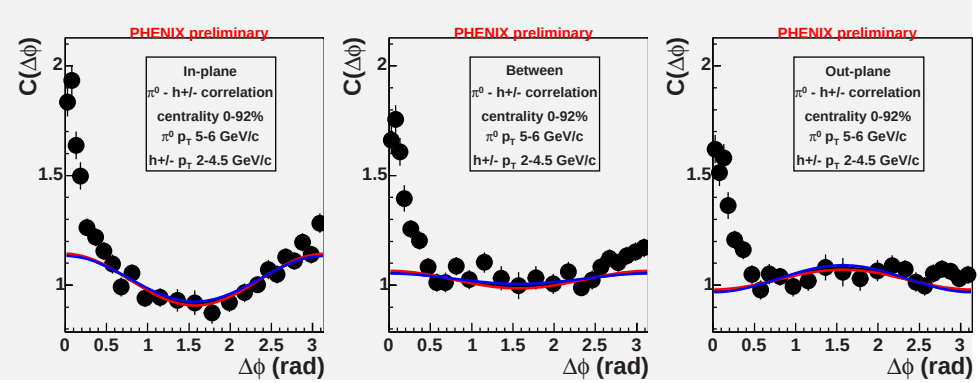

Figure 5.8 2004 Au+Au correlation function and its reaction-plane dependence. In each panel from left to right, the correlation functions are from in-plane, between, out-plane, respectively.

(by parallel talk of Justin Frantz and poster of Hua Pei) (92).

Summary of sources of systematic errors:

• Error of v_2, Cu+Cu only. This include the error of reaction-plane (resolution) and the error of v2 extraction. Both the errors are given by PHENIX paper(24). The v2 error is propagated by varying the flow shape by $1-\sigma$ of v2 and re-derive the correlation function and Gaussian fitting.

• Error of ZYAM. This means we vary the foreground shape by $1-\sigma$ of its flat line and re-derive the correlation function and Gaussian fitting.

• Error of π^0 mass. This error is 2%, and is derived by varying the invariant mass window and compare the S/B of π^0.

• Error of efficiency and centrality smearing. This is error is about 10% in the correlation function, and is propagated to the Gaussian fitting.

• In the correlation function a "bump" was observed at $|\Delta\phi| \sim \pi/2$. This is possibly due to the acceptance bias on ERT-trigger data and will affect our ZYAM. The error is estimated by flattening the bump and calculate the change of yields. We propagated the error of 10% into our p_{Tout} results.

• The RICH-veto cut will remove part of charged pions from our highest associated particle pT bin. This effect is estimated by comparing to PHENIX spectrum and propagated to yields.

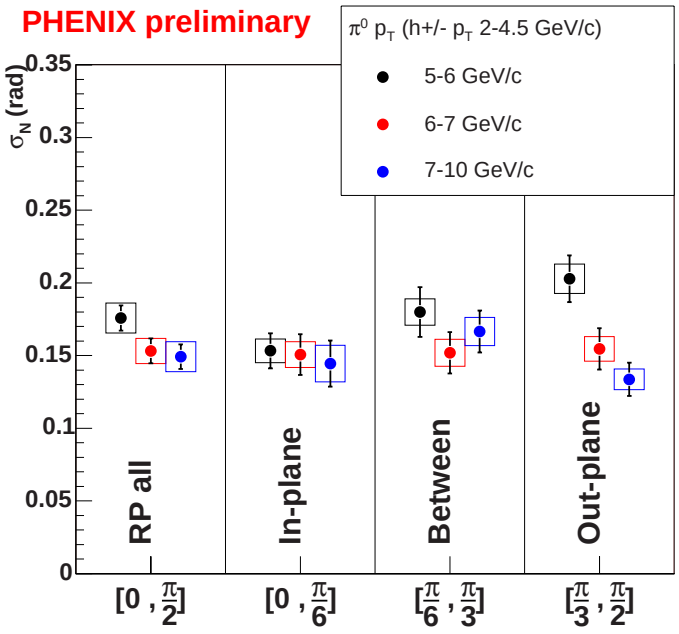

Figure 5.9 Near-side peak Gaussian shape width as function of reaction–plane and trigger pT. Associated pT is fixed to be [2, 4.5]GeV. We also include p+p and d+Au data as reference on left-side of plot. Error lines are statistical errors and error boxes are systematic errors.

Note there were some concerns about this Cu+Cu to p+p comparison.

My Cu+Cu work always came from ERT-trigger data. In QM06 result I was using the ERT-to-ERT mixing for Cu+Cu

The p+p points in these QM06 plots are from Jiangyong Jia of PHENIX, who used the Run 2005 200GeV p+p data of PHENIX. His work always uses ERT-minbias mixing as reported. Jiangyong Jia also did the near-side peak-width work of Cu+Cu shown in Fig.5.15, and we observe within errors the same near-side broadening from AA to p+p as we observed in Au+Au analysis.

In 2007, with the improved recalibrators (Sec.4.4.1), I re-ran the Cu+Cu analysis. It agrees with the 2006 output very well, even if we changed the mixing method to ERT-minbias mixing.

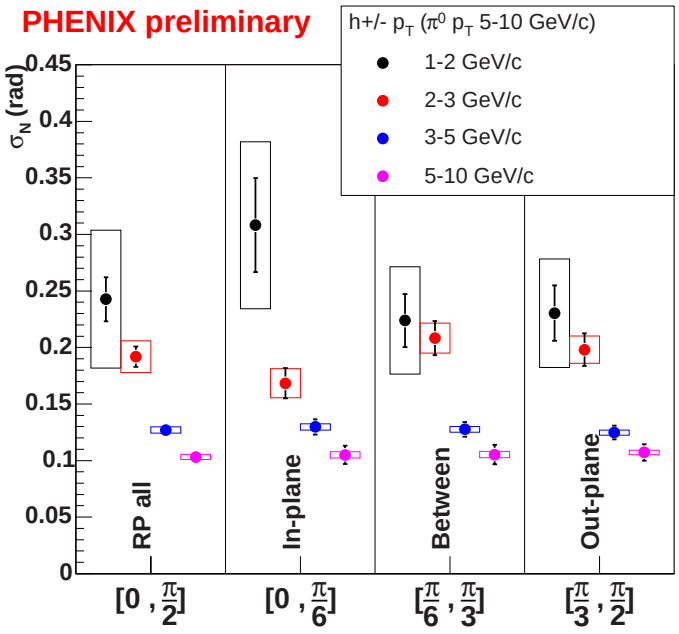

Figure 5.10 Near-side peak Gaussian shape width as function of reaction–plane and associated pT. Trigger pT is fixed to be [5, 10]GeV. We also include p+p and d+Au data as reference on left-side of plot. Error lines are statistical errors and error boxes are systematic errors.

The comparison is shown in Fig.5.16.

Meanwhile, I do the p+p reference work myself instead of using J.Jia's data. This time, I use the combined Run 2005 and 2006 200GeV p+p data of PHENIX. These two years' data agree with each other, but they have an excess comparing to J.Jia's $p_{Tout,N}$ work in Fig.5.17.

This difference of p+p result cancels the excess we originally observed in QM06 work. If I replace the p+p reference in Fig.5.11 to be my own work, the new result is in Fig.5.18. We can see clearly the excess of $p_{Tout,N}$, if any, is much weakened. It's still being explored the reason for this difference in the two p+p result.

5.2.2 Result of 2+1 Correlation

It's well understood that the existence of any difference of correlation function, when we compare AA collision to p+p, can be taken as proof of medium effect. However, one thing

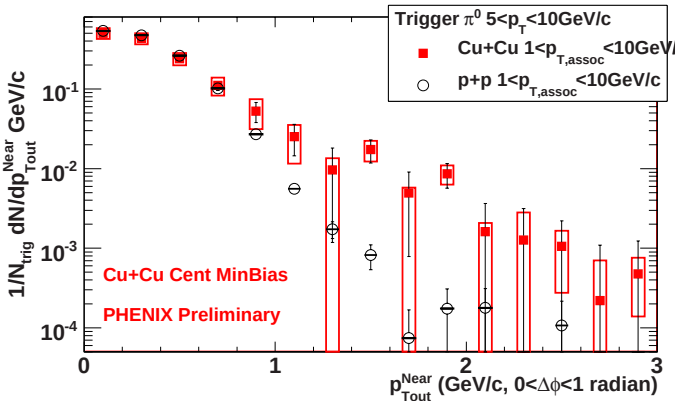

Figure 5.11 This is the near-side p_{Tout}

. Red points are of minbias Cu+Cu, black points are of p+p. Error lines are statistical, and error boxes are systematic. The p_{Tout} are calculated and summed via all associated particles within $1 < p_T < 10$GeV, and $|\Delta\phi| < 1$ radian.

important to notice, is that the opposite conclusion doesn't stand, i.e., non-difference doesn't mean no medium effect. We explained before in the introduction chapter 1, that in 2-particle correlation, the existence of surface-bias (Sec.1.2.8). This means if we don't observe any difference in 2-particle correlation, another explaination is that surface-bias is so strong, that most jets observed in AA collision come from nearby the surface, or even tangential to the surface.

That's how we came to do this "2+1" correlation. The details of physical purpose has been explained in the introduction chapter (Sec.1.2.8.1), and the experimental details are summarized in the event selection section 4.2. The following analysis work in this section contains the bulk of the most-recent results in this thesis.

Summary of sources of systematic errors:

• Error of v_2, Cu+Cu only. This include the error of reaction-plane (resolution) and the error of v2 extraction. Both the errors are given by PHENIX paper(24). The v2 error is propagated by varying the flow shape by $1-\sigma$ of v2 and re-derive the correlation function and Gaussian fitting.

• Error of ZYAM. This means we vary the foreground shape by $1-\sigma$ of its flat line and re-derive the correlation function and Gaussian fitting.

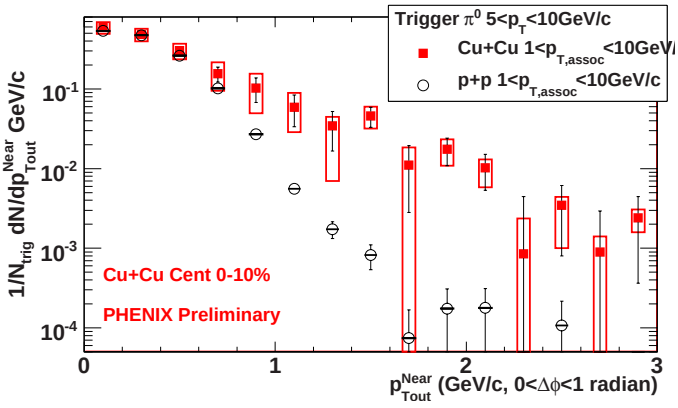

Figure 5.12 This is the near-side p_{Tout}

. Red points are of 0-10% Cu+Cu, black points are of p+p. Error lines are statistical, and error boxes are systematic. The p_{Tout} are calculated and summed via all associated particles within $1 < p_T < 10$GeV, and $|\Delta\phi| < 1$ radian.

• Error of π^0 mass. This error is 2%, and is derived by varying the invariant mass window and compare the S/B of π^0.

• Error of efficiency and centrality smearing. This is error is about 10% in the correlation function, and is propagated to the Gaussian fitting.

• In the correlation function we used 2-particle mixing acceptance. Although we required the trigger π^0 has a "conditional" away-side high-pT particle in its own real event, there was concern that this might lead to error in acceptance. This error is conservatively estimated to be 8% by calculating the ratio between acceptance in different mixing events. We propagated this error of 8% into our yields and Gaussian fitting.

• The RICH-veto cut will remove part of charged pions from our highest associated particle pT bin. This effect is estimated by comparing to PHENIX spectrum and propagated to yields.

5.2.2.1 Correlation Functions

First we reconstruct the correlation functions. In each plot of Fig.5.19 to 5.25, we compare the near-side jet correlation function of Cu+Cu to p+p. We also show the evolution of jet correlations as function of associated/conditional p_T inside each plot. It's interesting to make

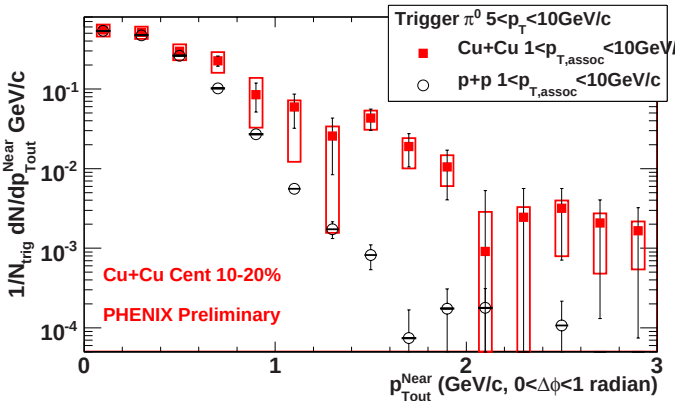

Figure 5.13 This is the near-side p_{Tout}

. Red points are of 10-20% Cu+Cu, black points are of p+p. Error lines are statistical, and error boxes are systematic. The p_{Tout} are calculated and summed via all associated particles within $1 < p_T < 10$GeV, and $|\Delta\phi| < 1$ radian.

the following observations:

• At the most central region of near-side peak $|\Delta\phi| \sim 0$, the Cu+Cu yield is higher than that of p+p in case of no "conditional" particle requirement (top row of each plot).

• However the Cu+Cu yield relatively drops below that of p+p if we have a "conditional" particle requirement, while both increase with the increasing of "conditional" particle p_T.

We shall quantify this trend in later section (Sec.5.2.2.3) and propose an explaination.

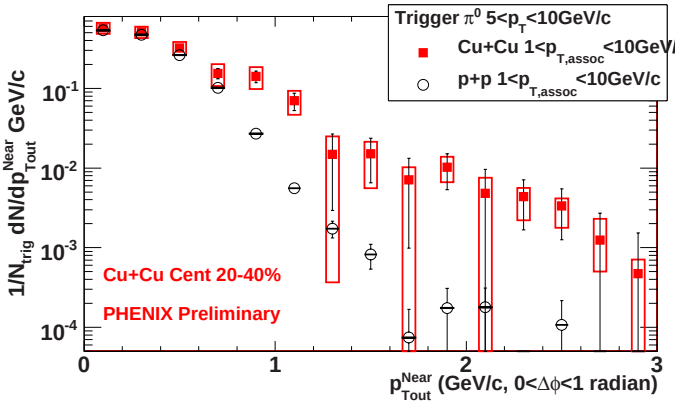

Figure 5.14 This is the near-side p_{Tout}

. Red points are of 20-40% Cu+Cu, black points are of p+p. Error lines are statistical, and error boxes are systematic. The p_{Tout} are calculated and summed via all associated particles within $1 < p_T < 10$GeV, and $|\Delta\phi| < 1$ radian.

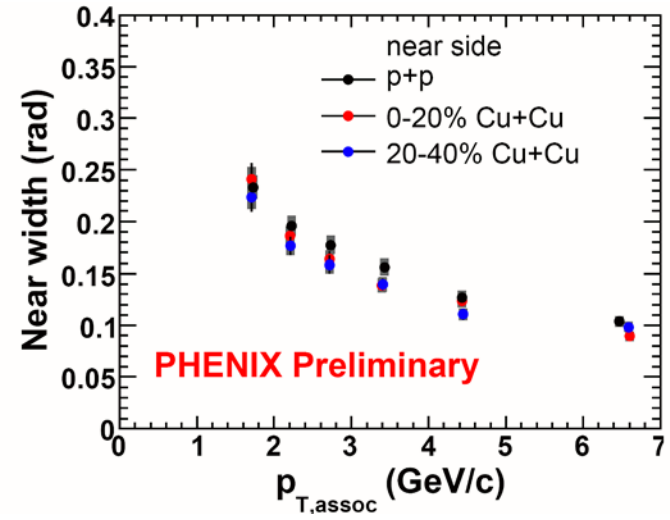

Figure 5.15 This is the near-side width σ. Error lines are statistical, and error boxes are systematic. The trigger π^0 are $5 < p_T < 10$GeV, and σs are plotted as function of centrality and assoc p_T.

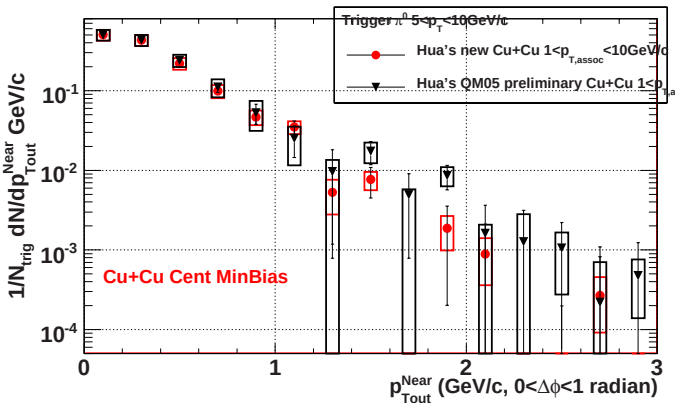

Figure 5.16 This is to compare H.Pei's 2006 analysis of Cu+Cu to his own 2005 PHENIX preliminary work. Error lines are statistical, and error boxes are systematic. The trigger π^0 are $5 < p_T < 10$GeV, and σs are plotted as function of centrality and assoc p_T. Red points are from 2006 analysis, and black points are from his own 2005 PHENIX prelimnary plots. Both analysis work on the same data set. However the main change on analysis method is the event-mixing turned from ERT-ERT mixing to ERT-minbias mixing.

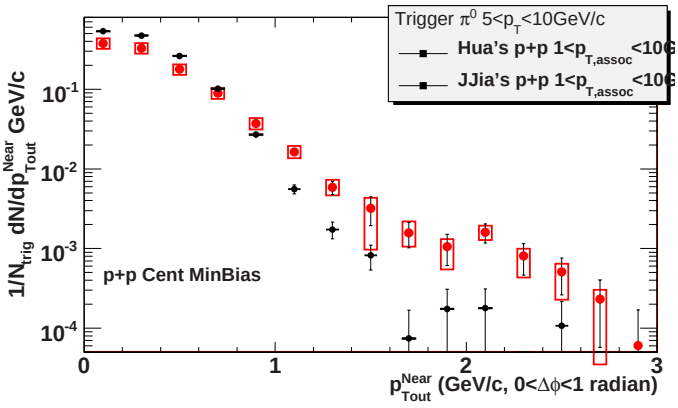

Figure 5.17 This is to compare H.Pei's 200GeV p+p near-side p_{Tout} with J.Jia's. Error lines are statistical, and error boxes are systematic. The trigger π^0 are $5 < p_T < 10$GeV, and σs are plotted as function of centrality and assoc p_T. Red points are from H.Pei (year 2005 and 2006), and black points are from J.Jia(year 2005).

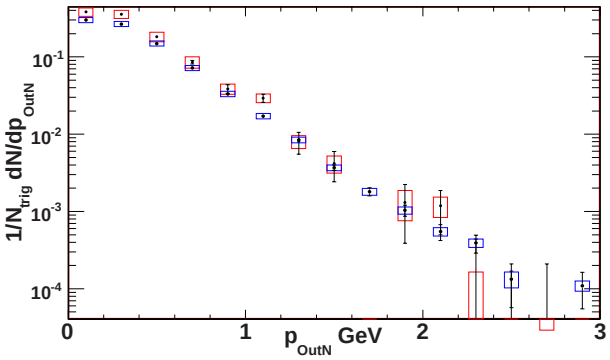

Figure 5.18 This is the near-side p_{Tout}

. Points with red boxes are of Cu+Cu, points with blue boxes are of p+p. Both come from my recent analysis after the QM06. Error lines are statistical, and error boxes are systematic. The p_{Tout} are calculated and summed via all associated particles within $1 < p_T < 10$GeV, and $|\Delta\phi| < 1$ radian.

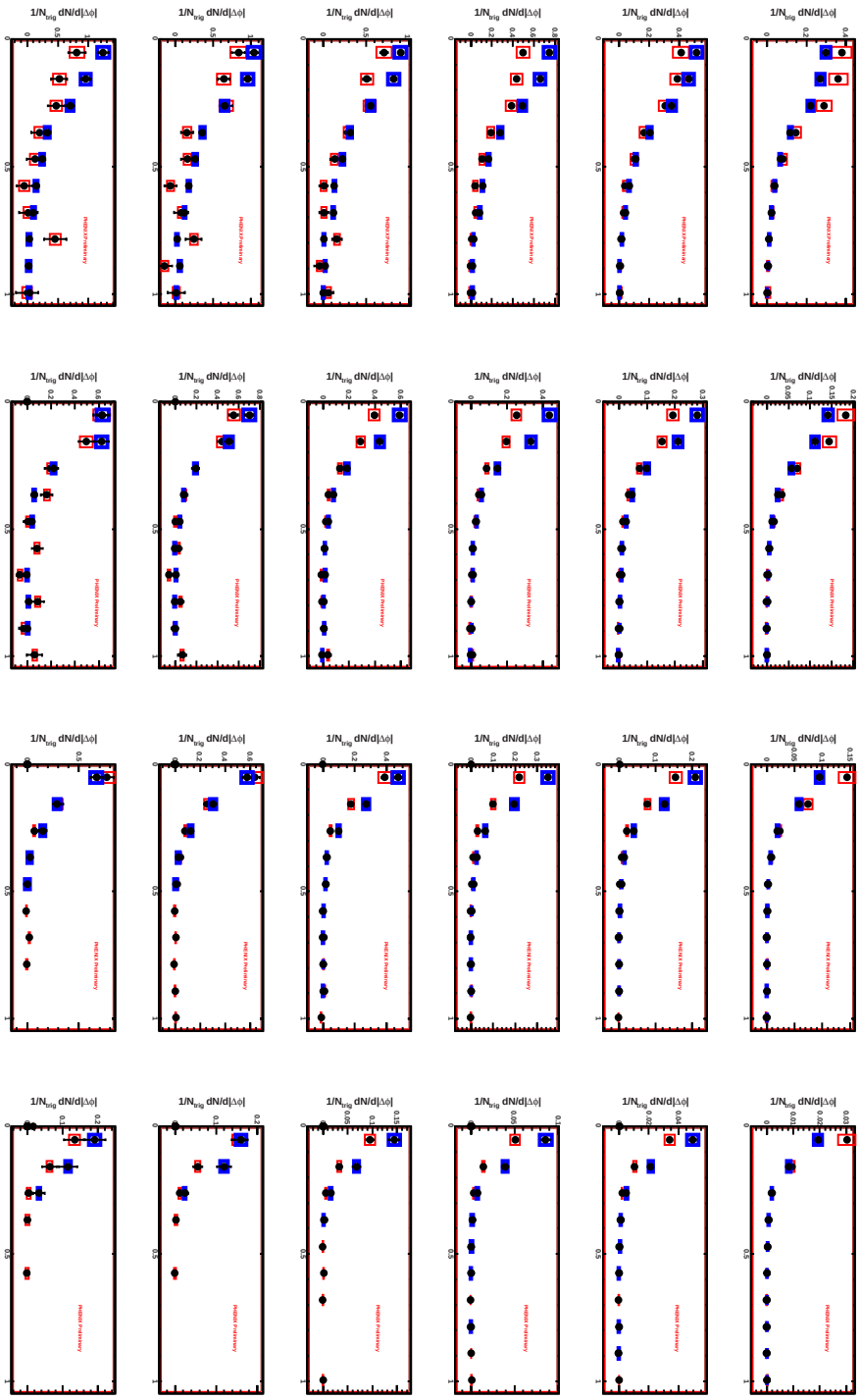

Figure 5.19 In this plot we compare the min-bias jet functions of Cu+Cu (with red systematic error boxes) to p+p (with blue systematic error boxes). This is the per-trigger yield of π^0-h correlation as a function of $|\Delta\phi|$. The trigger π^0 is $4 < pT < 10$GeV. Of all sub-panels, from left to right column the associated charged hadron pT is 1-2, 2-3, 3-5, 5-10GeV, and from top to bottom the conditional pT requirement is non-required, [1,10GeV], [2,10GeV], [3,10GeV], [4,10GeV], [5,10GeV].

We now show correlation functions from central to peripheral Cu+Cu collisions.

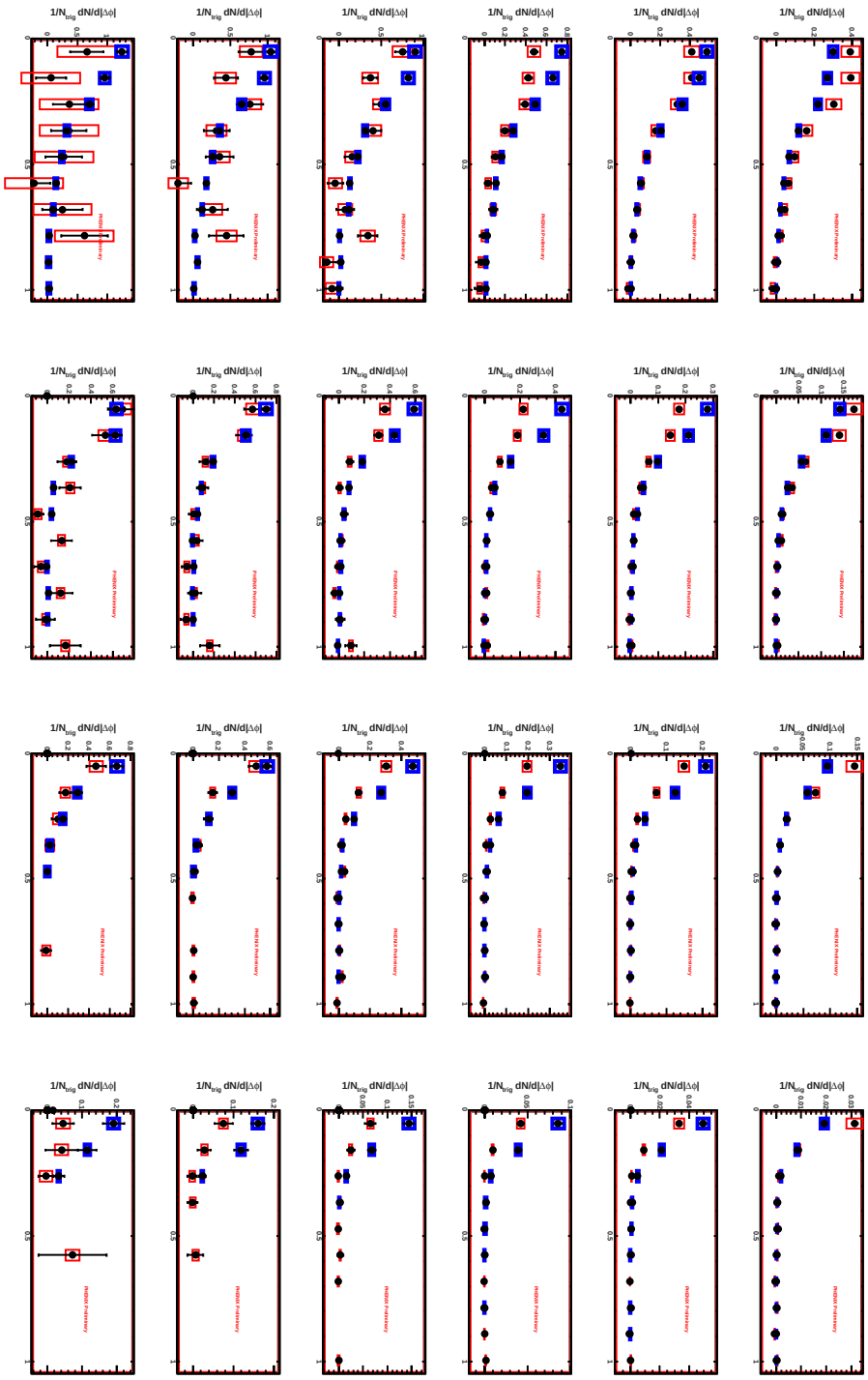

Figure 5.20 In this plot we compare the 0-10% jet functions of Cu+Cu (with red systematic error boxes) to p+p (with blue systematic error boxes). This is the per-trigger yield of π^0-h correlation as a function of $|\Delta\phi|$. The trigger π^0 is $4 < pT < 10$GeV. Of all sub-panels, from left to right column the associated charged hadron pT is 1-2, 2-3, 3-5, 5-10GeV, and from top to bottom the conditional pT requirement is non-required, [1,10GeV], [2,10GeV], [3,10GeV], [4,10GeV], [5,10GeV].

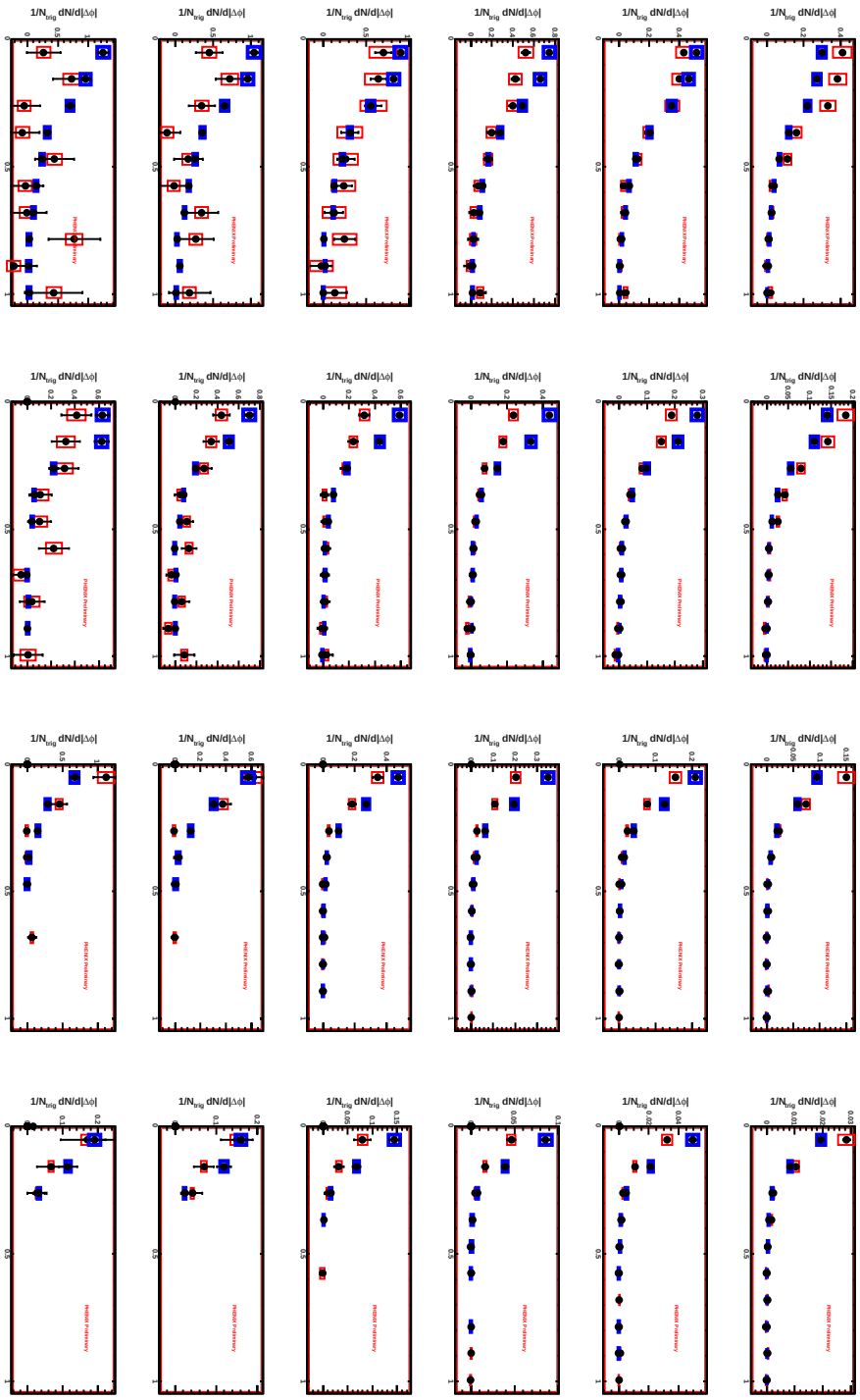

Figure 5.21 In this plot we compare the 10-20% jet functions of Cu+Cu (with red systematic error boxes) to p+p (with blue systematic error boxes). This is the per-trigger yield of π^0-h correlation as a function of $|\Delta\phi|$. The trigger π^0 is $4 < pT < 10$GeV. Of all sub-panels, from left to right column the associated charged hadron pT is 1-2, 2-3, 3-5, 5-10GeV, and from top to bottom the conditional pT requirement is non-required, [1,10GeV], [2,10GeV], [3,10GeV], [4,10GeV], [5,10GeV].

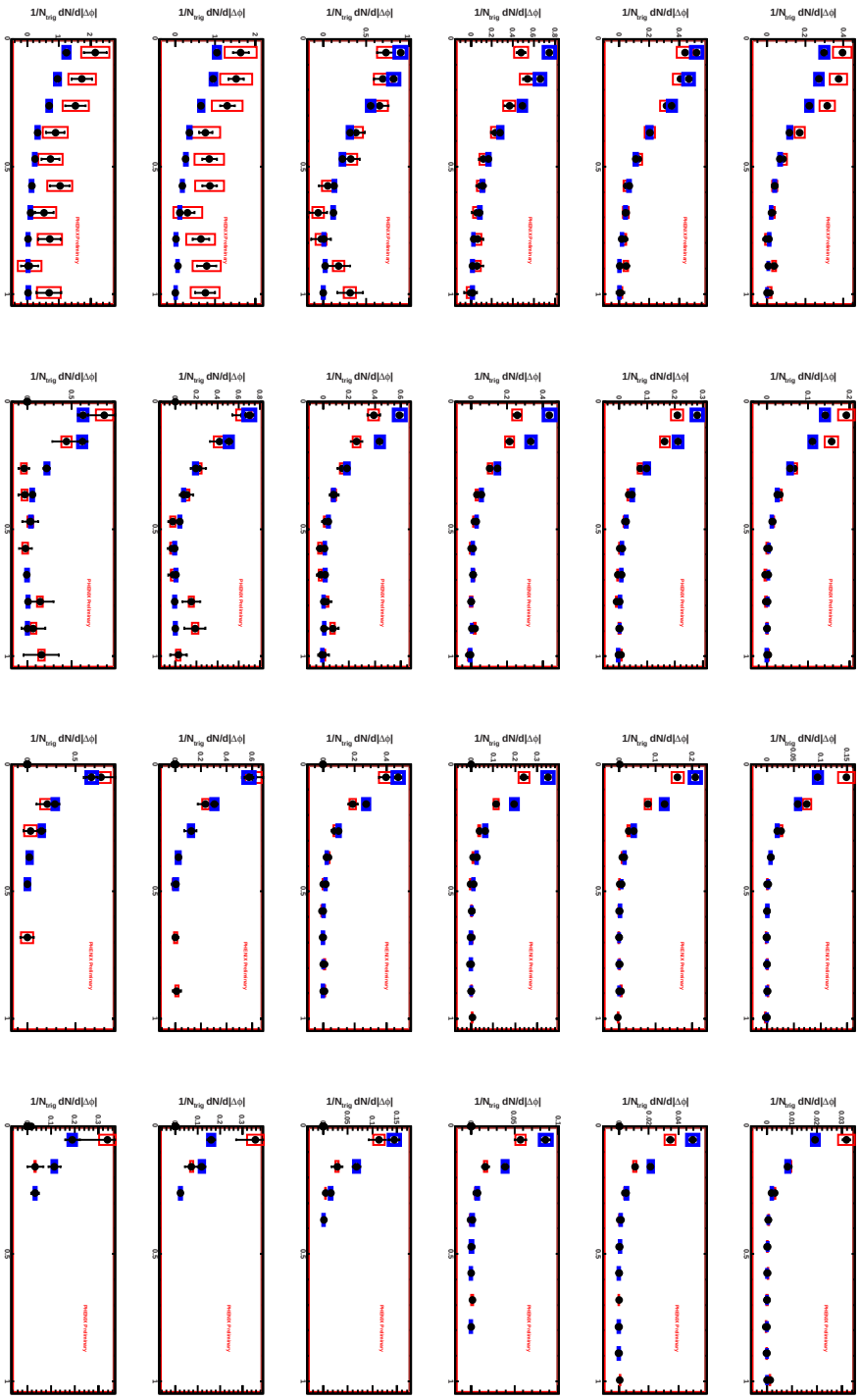

Figure 5.22 In this plot we compare the 20-30% jet functions of Cu+Cu (with red systematic error boxes) to p+p (with blue systematic error boxes). This is the per-trigger yield of π^0-h correlation as a function of $|\Delta\phi|$. The trigger π^0 is $4 < pT < 10$GeV. Of all sub-panels, from left to right column the associated charged hadron pT is 1-2, 2-3, 3-5, 5-10GeV, and from top to bottom the conditional pT requirement is non-required, [1,10GeV], [2,10GeV], [3,10GeV], [4,10GeV], [5,10GeV].

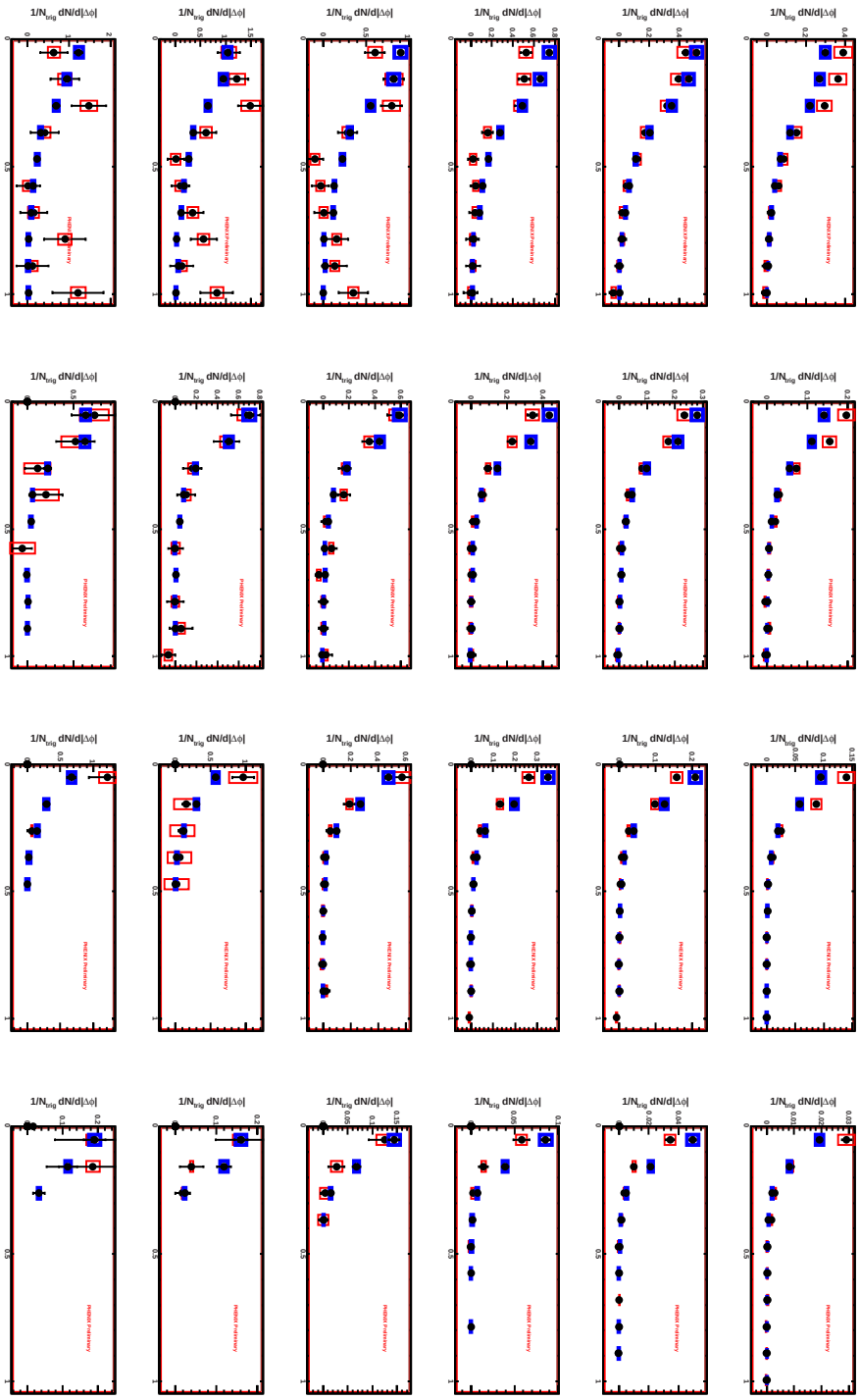

Figure 5.23 In this plot we compare the 30-40% jet functions of Cu+Cu (with red systematic error boxes) to p+p (with blue systematic error boxes). This is the per-trigger yield of π^0-h correlation as a function of $|\Delta\phi|$. The trigger π^0 is $4 < pT < 10$GeV. Of all sub-panels, from left to right column the associated charged hadron pT is 1-2, 2-3, 3-5, 5-10GeV, and from top to bottom the conditional pT requirement is non-required, [1,10GeV], [2,10GeV], [3,10GeV], [4,10GeV], [5,10GeV].

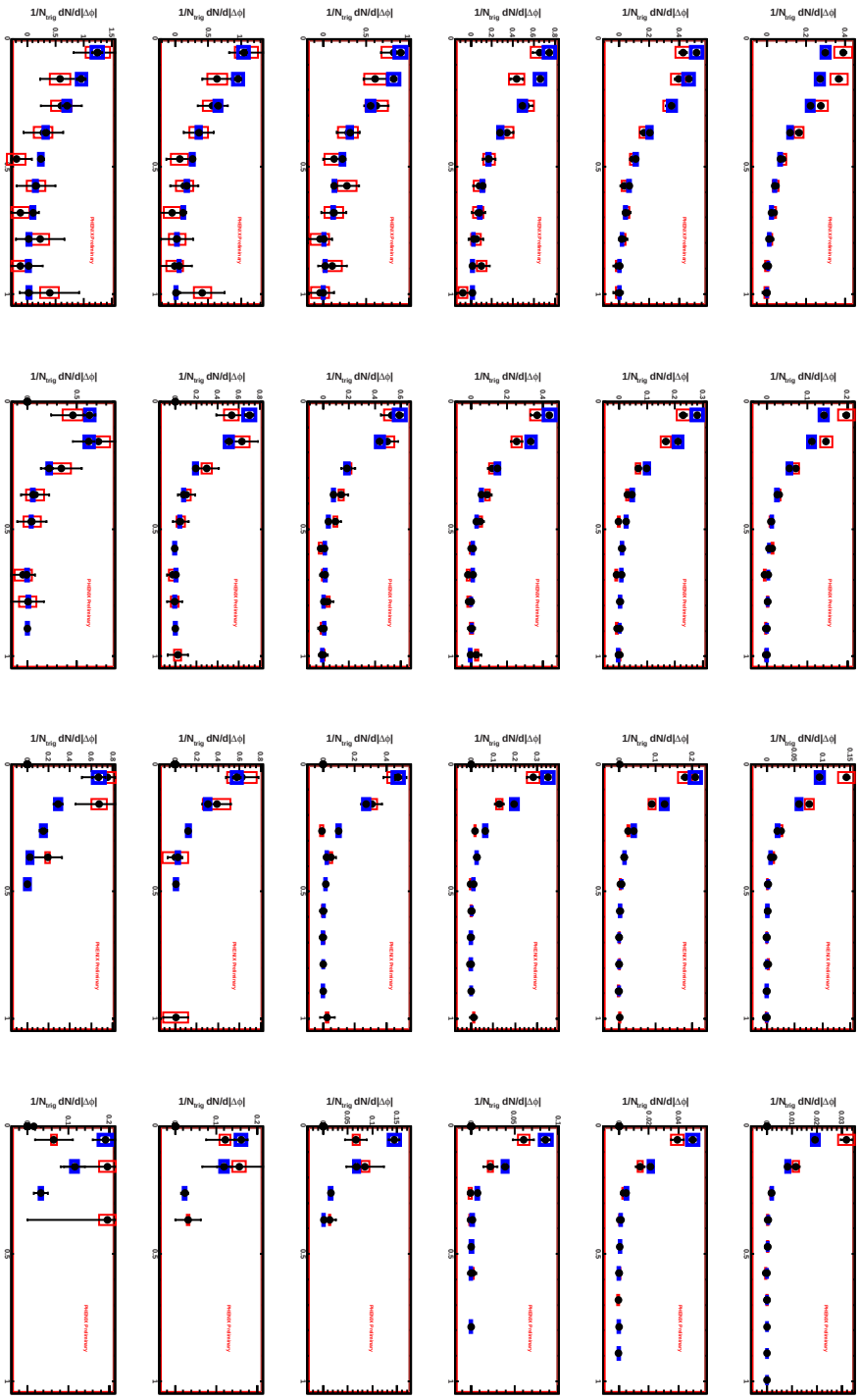

Figure 5.24 In this plot we compare the 40-50% jet functions of Cu+Cu (with red systematic error boxes) to p+p (with blue systematic error boxes). This is the per-trigger yield of π^0-h correlation as a function of $|\Delta\phi|$. The trigger π^0 is $4 < pT < 10$GeV. Of all sub-panels, from left to right column the associated charged hadron pT is 1-2, 2-3, 3-5, 5-10GeV, and from top to bottom the conditional pT requirement is non-required, [1,10GeV], [2,10GeV], [3,10GeV], [4,10GeV], [5,10GeV].

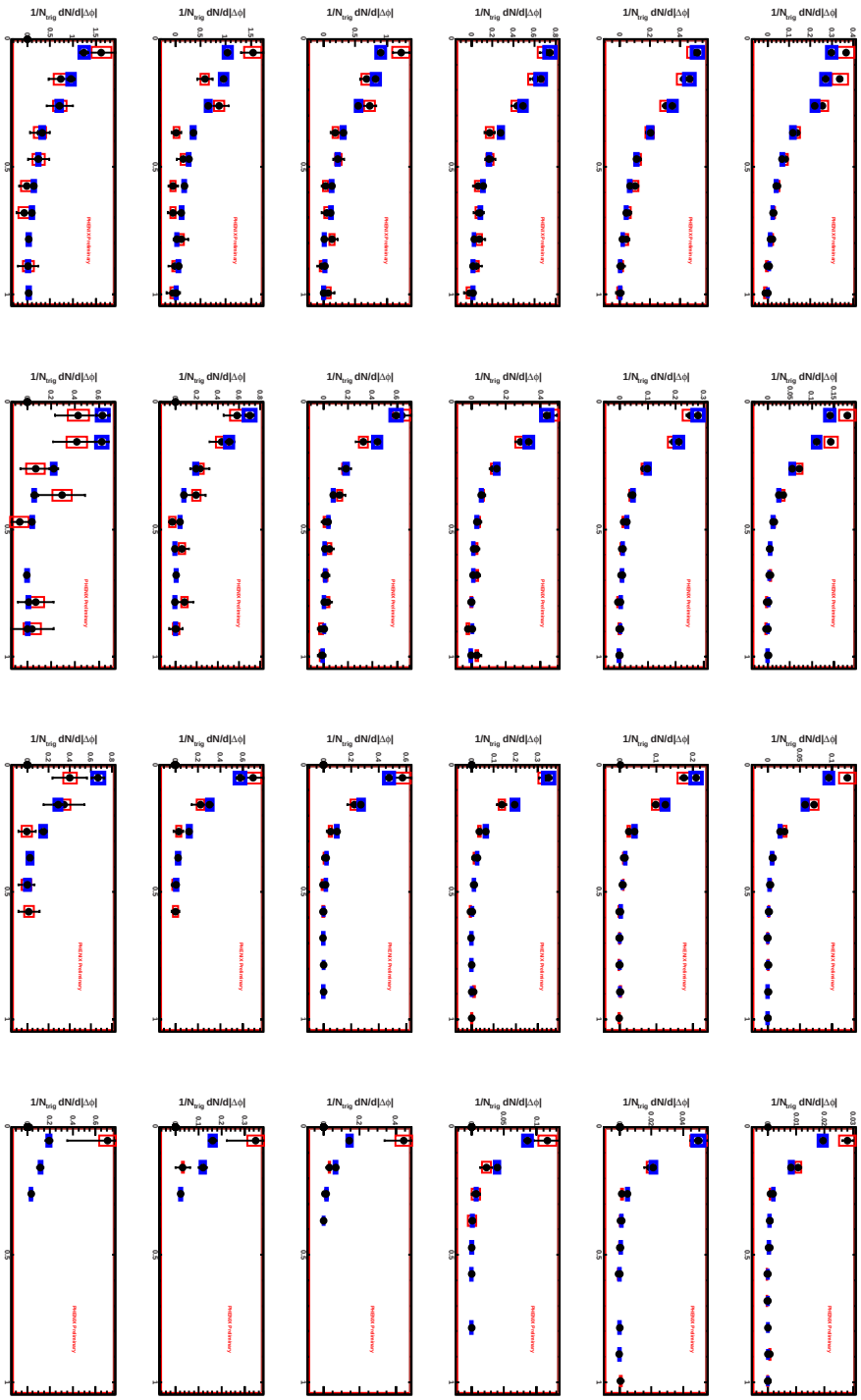

Figure 5.25 In this plot we compare the 50-92% jet functions of Cu+Cu (with red systematic error boxes) to p+p (with blue systematic error boxes). This is the per-trigger yield of π^0-h correlation as a function of $|\Delta\phi|$. The trigger π^0 is $4 < pT < 10$GeV. Of all sub-panels, from left to right column the associated charged hadron pT is 1-2, 2-3, 3-5, 5-10GeV, and from top to bottom the conditional pT requirement is non-required, [1,10GeV], [2,10GeV], [3,10GeV], [4,10GeV], [5,10GeV].

5.2.2.2 Shapes and Widths

As we did in earlier Au+Au sections, we fit the near-side shape with a Gaussian+flat function and calculate the peak width σ. In each plot of Fig.5.26 to 5.33, we compare the near-side jet peak width σ of Cu+Cu to p+p. Each panel shows a different associated p_T region. And for each associated p_T region, we first compare the minbias Cu+Cu vs. p+p, then give details on centrality dependence. Inside each plot, the near-side widths are plotted as function of conditional p_T between bins and function of centrality within bins.

The direct observation on these near-side widths σ plots is that at specific associated pT range, [3,5]GeV and possibly [5,10]GeV, the σ is broader from central Cu+Cu to peripheral Cu+Cu to p+p, with or without conditional particle requirement. This is a confirmation of what we shown earlier on 2004 Au+Au and 2005 Cu+Cu result.

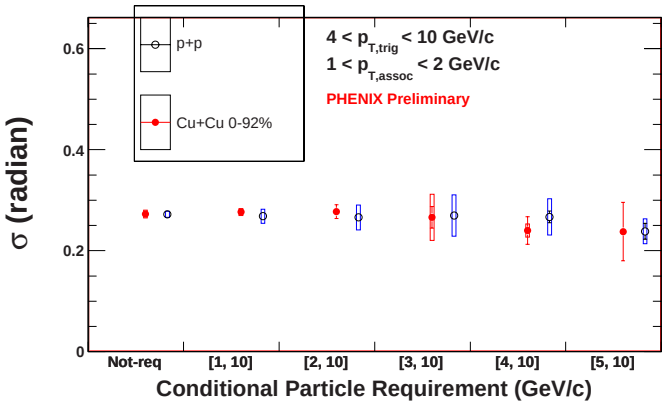

Figure 5.26 In this plot we compare the near-side peak width σ of minbias jet functions of Cu+Cu to p+p. The pT regions of trigger π^0 and associated charged hadrons are in the top-center legend. Of all bins, from left to right column the conditional pT requirement is non-required, [1,10GeV], [2,10GeV], [3,10GeV], [4,10GeV], [5,10GeV]

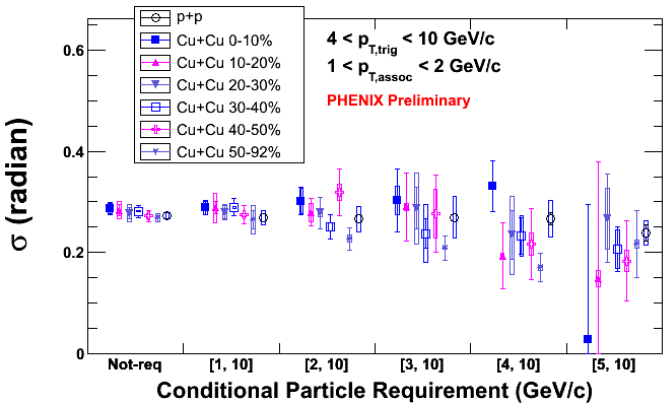

Figure 5.27 In this plot we compare the near-side peak width σ of various centrality of jet functions of Cu+Cu to p+p. The pT regions of trigger π^0 and associated charged hadrons are in the top–center legend. Of all bins, from left to right column the conditional pT requirement is non-required, [1,10GeV], [2,10GeV], [3,10GeV], [4,10GeV], [5,10GeV]. Within each bin from left to right, it's from central Cu+Cu to peripheral Cu+Cu until p+p.

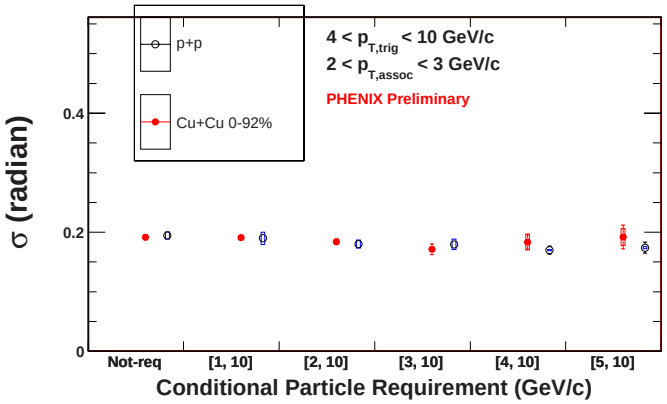

Figure 5.28 In this plot we compare the near-side peak width σ of minbias jet functions of Cu+Cu to p+p. The pT regions of trigger π^0 and associated charged hadrons are in the top-center legend. Of all bins, from left to right column the conditional pT requirement is non-required, [1,10GeV], [2,10GeV], [3,10GeV], [4,10GeV], [5,10GeV]

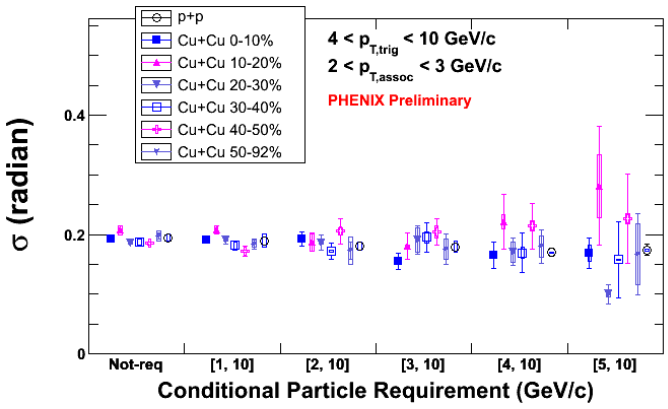

Figure 5.29 In this plot we compare the near-side peak width σ of various centrality of jet functions of Cu+Cu to p+p. The pT regions of trigger π^0 and associated charged hadrons are in the top–center legend. Of all bins, from left to right column the conditional pT requirement is non-required, [1,10GeV], [2,10GeV], [3,10GeV], [4,10GeV], [5,10GeV]. Within each bin from left to right, it's from central Cu+Cu to peripheral Cu+Cu until p+p.

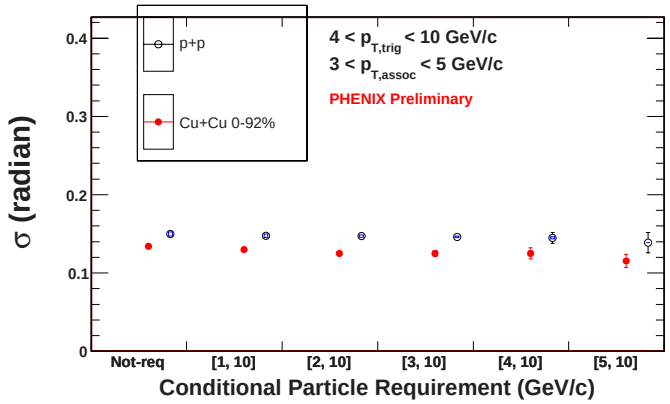

Figure 5.30 In this plot we compare the near-side peak width σ of minbias jet functions of Cu+Cu to p+p. The pT regions of trigger π^0 and associated charged hadrons are in the top-center legend. Of all bins, from left to right column the conditional pT requirement is non-required, [1,10GeV], [2,10GeV], [3,10GeV], [4,10GeV], [5,10GeV]

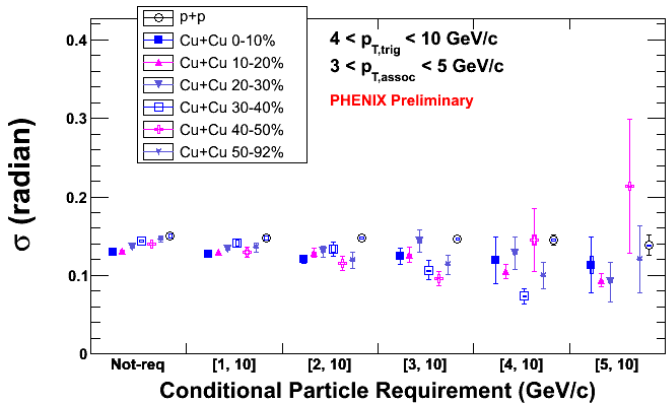

Figure 5.31 In this plot we compare the near-side peak width σ of various centrality of jet functions of Cu+Cu to p+p. The pT regions of trigger π^0 and associated charged hadrons are in the top–center legend. Of all bins, from left to right column the conditional pT requirement is non-required, [1,10GeV], [2,10GeV], [3,10GeV], [4,10GeV], [5,10GeV]. Within each bin from left to right, it's from central Cu+Cu to peripheral Cu+Cu until p+p.

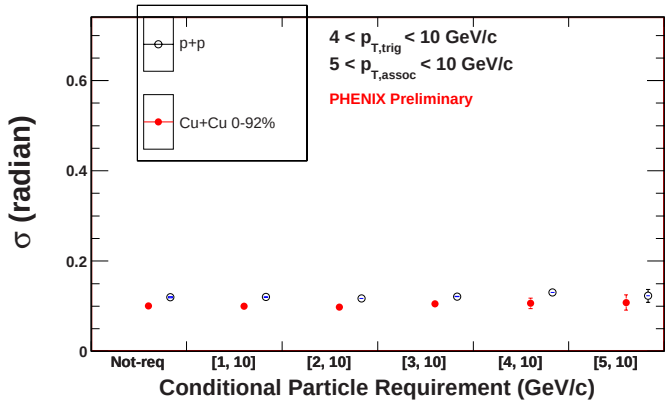

Figure 5.32 In this plot we compare the near-side peak width σ of minbias jet functions of Cu+Cu to p+p. The pT regions of trigger π^0 and associated charged hadrons are in the top-center legend. Of all bins, from left to right column the conditional pT requirement is non-required, [1,10GeV], [2,10GeV], [3,10GeV], [4,10GeV], [5,10GeV]

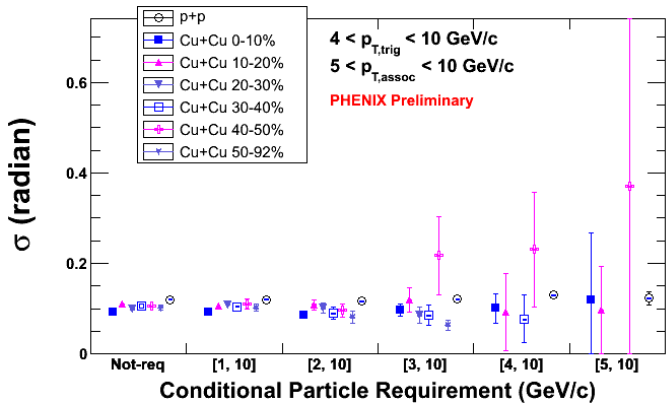

Figure 5.33 In this plot we compare the near-side peak width σ of various centrality of jet functions of Cu+Cu to p+p. The pT regions of trigger π^0 and associated charged hadrons are in the top–center legend. Of all bins, from left to right column the conditional pT requirement is non-required, [1,10GeV], [2,10GeV], [3,10GeV], [4,10GeV], [5,10GeV]. Within each bin from left to right, it's from central Cu+Cu to peripheral Cu+Cu until p+p.

5.2.2.3 Yields

Then we calculate the yield as a function of centrality and conditional p_T. As we noticed earlier in Sec.5.2.2.1, the yields of both Cu+Cu and p+p increase with the adding of "conditional" particle and pT. This increasing is stronger in p+p than in Cu+Cu. Now we quantify this observation, by doing an integral of jet correlation at $|\Delta\phi| < 1 radian$. This $|\Delta\phi|$ region is selected so that any fluctuation of ZYAM touching has the least effect, while we still keep most near-side jet contribution. In each plot of Fig.5.34 to 5.41, we compare the integrated near-side jet per-trigger yield of Cu+Cu to p+p. Each panel shows a different associated p_T region. And for each associated p_T region, we first compare the minbias Cu+Cu vs. p+p, then give details on centrality dependence. Again, inside each plot, the integrated per-trigger near-side yields are ploted as function of conditional p_T between bins and function of centrality within bins.

We have the following observations:

1) In all associated pT and centrality combinations, the integrated per-trigger yield increase with the "conditional" pT.

2) In the most left bin of each plot, where we don't require a "conditional" particle, the yield is centrality-independent. This is consistent to our previous Au+Au measurements 5.1.

3) When we fixed the trigger π^0 pT to be at a region, [4, 10]GeV in our case, then at specific regions of assocaited charged hadron pT, [2, 3]GeV and [3, 5]GeV in our result, we see a centrality dependence in the per-trigger yield. The per-trigger yield of Cu+Cu increase from most-central events to most-peripheral events and approach that of p+p. In the bins of associated and "conditional" pT regions are close or even overlapping, this centrality dependence is most evident. Note this is the "near-side" yield of associates, while our "conditional" particle is required to be on "far-side". So we automatically removed the possible bias of conditional particle contamination in our yields.

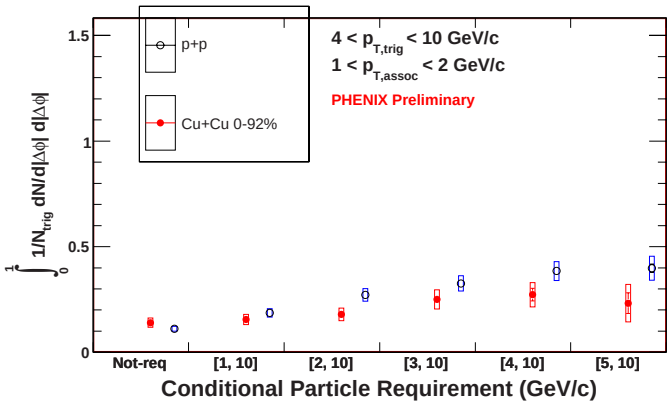

Figure 5.34 In this plot we compare the integrated near-side per-trigger yield of minbias jet functions of Cu+Cu to p+p. The pT regions of trigger π^0 and associated charged hadrons are in the top-center legend. Of all bins, from left to right column the conditional pT requirement is non-required, [1,10GeV], [2,10GeV], [3,10GeV], [4,10GeV], [5,10GeV]

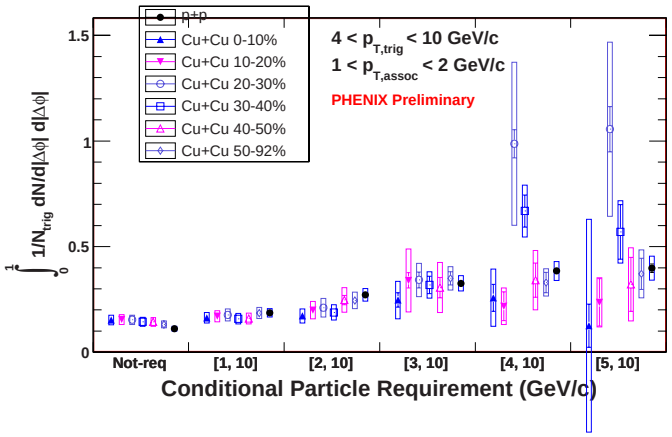

Figure 5.35 In this plot we compare the integrated near-side per-trigger yield of various centrality of jet functions of Cu+Cu to p+p. The pT regions of trigger π^0 and associated charged hadrons are in the top-center legend. Of all bins, from left to right column the conditional pT requirement is non-required, [1,10GeV], [2,10GeV], [3,10GeV], [4,10GeV], [5,10GeV]. Within each bin from left to right, it's from central Cu+Cu to peripheral Cu+Cu until p+p.

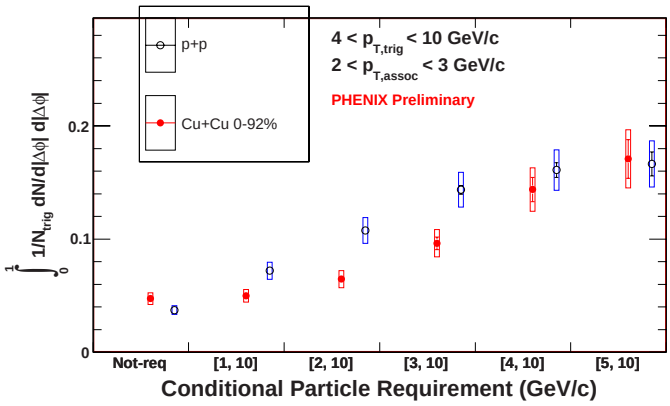

Figure 5.36 In this plot we compare the integrated near-side per-trigger yield of minbias jet functions of Cu+Cu to p+p. The pT regions of trigger π^0 and associated charged hadrons are in the top-center legend. Of all bins, from left to right column the conditional pT requirement is non-required, [1,10GeV], [2,10GeV], [3,10GeV], [4,10GeV], [5,10GeV]

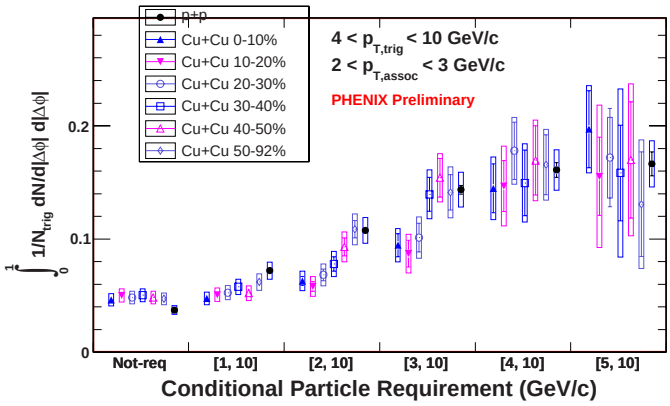

Figure 5.37 In this plot we compare the integrated near-side per-trigger yield of various centrality of jet functions of Cu+Cu to p+p. The pT regions of trigger π^0 and associated charged hadrons are in the top-center legend. Of all bins, from left to right column the conditional pT requirement is non-required, [1,10GeV], [2,10GeV], [3,10GeV], [4,10GeV], [5,10GeV]. Within each bin from left to right, it's from central Cu+Cu to peripheral Cu+Cu until p+p.

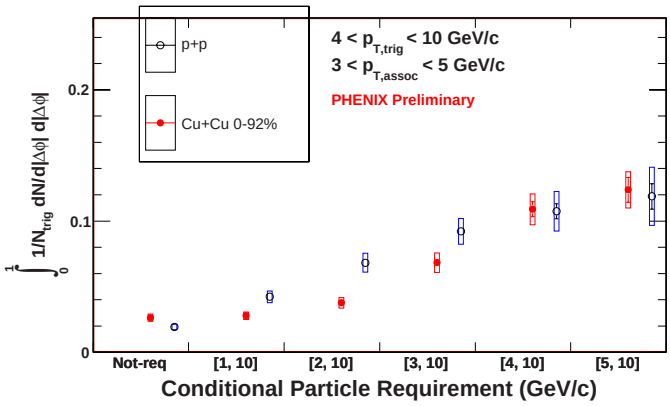

Figure 5.38 In this plot we compare the integrated near-side per-trigger yield of minbias jet functions of Cu+Cu to p+p. The pT regions of trigger π^0 and associated charged hadrons are in the top-center legend. Of all bins, from left to right column the conditional pT requirement is non-required, [1,10GeV], [2,10GeV], [3,10GeV], [4,10GeV], [5,10GeV]

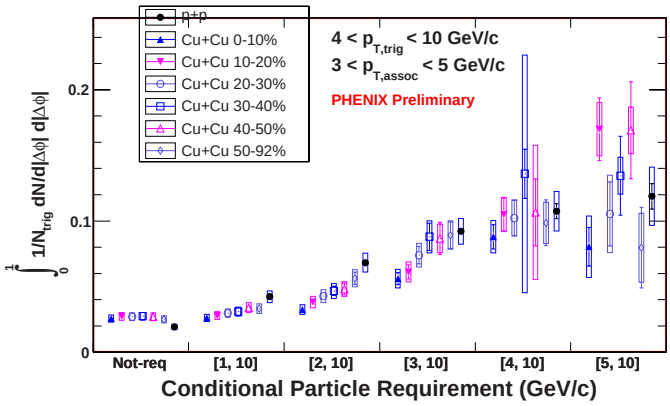

Figure 5.39 In this plot we compare the integrated near-side per-trigger yield of various centrality of jet functions of Cu+Cu to p+p. The pT regions of trigger π^0 and associated charged hadrons are in the top-center legend. Of all bins, from left to right column the conditional pT requirement is non-required, [1,10GeV], [2,10GeV], [3,10GeV], [4,10GeV], [5,10GeV]. Within each bin from left to right, it's from central Cu+Cu to peripheral Cu+Cu until p+p.

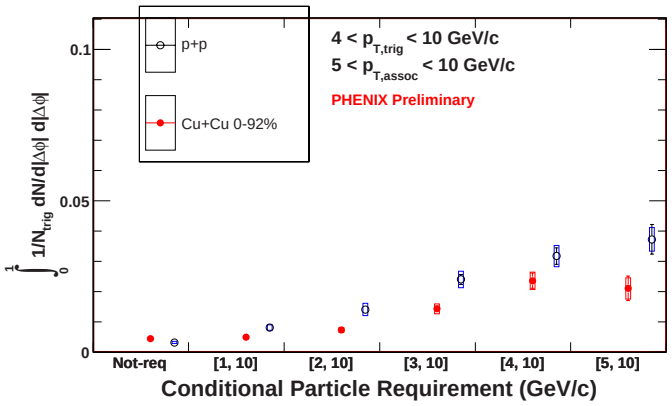

Figure 5.40 In this plot we compare the integrated near-side per-trigger yield of minbias jet functions of Cu+Cu to p+p. The pT regions of trigger π^0 and associated charged hadrons are in the top-center legend. Of all bins, from left to right column the conditional pT requirement is non-required, [1,10GeV], [2,10GeV], [3,10GeV], [4,10GeV], [5,10GeV]

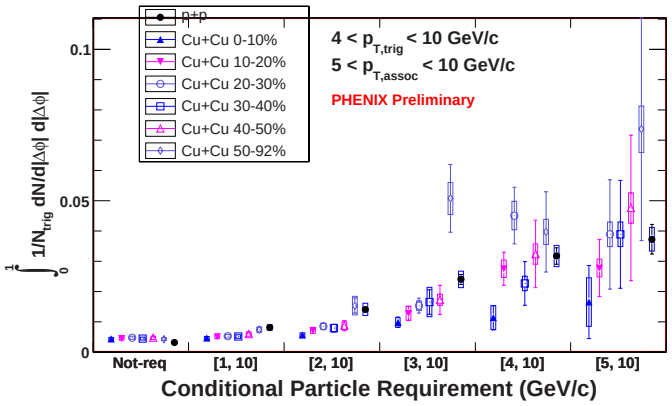

Figure 5.41 In this plot we compare the integrated near-side per-trigger yield of various centrality of jet functions of Cu+Cu to p+p. The pT regions of trigger π^0 and associated charged hadrons are in the top-center legend. Of all bins, from left to right column the conditional pT requirement is non-required, [1,10GeV], [2,10GeV], [3,10GeV], [4,10GeV], [5,10GeV]. Within each bin from left to right, it's from central Cu+Cu to peripheral Cu+Cu until p+p.

5.2.2.4 Shift the Yields

The results in this sections have been shown in QM08, via plenary talk of Achim Frantz and parallel talk of Hua Pei. The centrality and conditional pT dependence of near-side per-trigger yield are going to be discussed further in this section.

First, as we claimed in the introduction chapter (Sec.1.2.8.1), the "2+1 correlation" method should work statistically instead of a "perfectly clean" filter. Thus it's important to understand all sources of this conditional pT dependence. One claim from PHENIX publication (91) is that there exists a far-side particle bias. This claim is confirmed in p+p QCD simulation, where if we fix the trigger energy (pT) and increase the "conditional" particle energy (pT) at away-side, we actually increasing the hard-scattering energy scale Q^2. That's because if we assume the $\hat{z}$ on the away-side is independent of the near-side trigger particle, increasing the "conditional" particle pT means increasing the average away-side parton energy. Hence, we are changing the parton distribution function by sampling at different "conditonal" pT region with a fixed trigger pT. To be exact, the higher "conditional" pT will shift the $\hat{z}$ on the near-side to its lower end, i.e., the ratio of trigger pT to parton pT on near-side becomes smaller while the tigger pT is fixed. Hence we increase the average energy of near-side parton, and our near-side yield of associated particles also increases, if we assume the fragmentation function is independent of partion distribution function.

In p+p collisions this explaination is clear, but can it explain all the "conditional" pT dependence we observed in Cu+Cu, especially those in the most central collisions? Within current errors, the increase of p+p yields due to increasing conditonal pT is stronger than that of Cu+Cu. This may indicate the Cu+Cu result do include change of surface-bias. We are still working on this topic.

Second, we observe this centrality dependence of per-trigger yield. If this really means the loss of energy, i.e., shifting of surface-bias, we need to answer where the energy has gone. Possible explainations include the medium response like "ridge-effect", as both PHENIX and STAR have shown in recent Quark Matter conferences (92). However, before we can answer that question, we need to confirm our measurements of yields are exclusively from jets.

As we introduced in the definition section of v_2 (Sec. 2.1.4.1), the flow measurement are supposed to contain all effects of pure medium (24). Thus, the subtraction of flow shape by ZYAM method shall remove any correlation between trigger particle (tagging the jet) and soft particle of medium, and leave us only the pure jet correlation. This is now well accepted in 2-particle correlation. However, in case of "2+1" particle correlation, we have this "conditional" particle at the far-side of jet (tagged by the trigger π^0). While the idea of "2+1" requires this "conditional" particle is from a back-to-back jet (Sec.1.2.8.1), it is also possible that this particle comes from the underlying events Currently it's not possible in PHENIX to do identify them event-by-event. This assumption is partially confirmed at higher conditional pT bins, where even central Cu+Cu yields is relatively closer to p+p, because a higher-pT "conditional" particle is more likely from a back-to-back jet and less likely from the underlying events.

Therefore, it's importtant to derive a "pure back-to-back jet correlation" in our "2+1" method. Possible solutions have been discussed in both PHENIX and STAR.

One method we applied in the analysis work shown below, but not generally approved yet within the PHENIX, is to use the "normal 2-particle" correlation to estimate the S/B of our "2+1", i.e., how much percentage of our "conditional" particle is really from back-to-back jet. The exact method is to measure the 2-particle correlation, where the trigger threshold is the same as the "2+1", and the associated particle threshold is now using that of the "conditional" in the "2+1". By doing this, we have the normal unsubtracted correlation function, and use ZYAM to get the jet signal and flow background, just as what we did with all 2-particle correlation. But now, by comparing the jet signal and flow background on the far-side ($|\Delta\phi| < \pi/2$), we can derive the S/B of correlation function at far-side. This S/B is then used to tell us how much of our "conditional" particles are really from back-to-back jets, as shown in the equation.5.1.

$$Yield_{withcondition,inclusive} = Yield_{conditionfromrealjet} \times \frac{S}{S+B} + Yield_{conditionfromunderlying}\, times \frac{B}{S+B} \tag{5.1}$$

Here we take our previous "2+1" particle jet function as a weighted sum of those single-jet

ones and back-to-back-jet ones, and we already know what a single-jet look like in a normal 2-particle jet function. So the S/B results help us to disentangle the "true" back-to-back jet from our existing "2+1" correlation function.

The sample of our work is shown below in Fig.5.42 to 5.45. While the error-bars are now much bigger because of the S/B estimation, the comparison of the "shifted 2+1" yields to previous "unshifted 2+1" probably tells us some important facts:

1) The conditonal pT dependence of integrated yields still exists, when we fix the trigger/associated/centrality. This is particularly true at p+p or peripheral Cu+Cu centrality, where the jet signals are more clear and S/B estimations are more stable. This fact is consistent to what was originally claimed in (91), where the sampling of higher-pT "conditional" particle always increase the energy scale and thus the near-side yields, even if you fix the near-side trigger/associated pT.

2) If we look at specific pT region, such as $4 < triggerpT < 10GeV$, $3 < assocpT < 5GeV$, $3 < conditionalpT < 10GeV$, the centrality dependence still exists, but opposite to what we earlier observed in the "unshifted 2+1" correlation in Sec.5.2.2.3. This reversed trend is still being investigated while this thesis is being written. We need to have more confidence on our "shift" estimation before we can make any claim relying on the trend. However, as long as we observe anything beyond a "flatness and independence of centrality" of the yields, it's encouraging to think we may have really done something to change the surface bias.

Whenever we fix the method of getting "clean back-to-back jet" within "2+1" correlation, it will applied to the newest Run 2007 Au+Au data of PHENIX. The Run 2007 PHENIX Au+Au data has more than 3 times of its Run 2004 Au+Au, which have already produced impressive publications including (66).

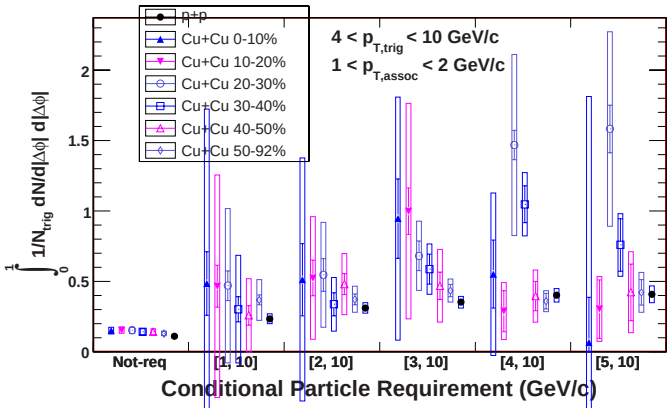

Figure 5.42 In this plot we compare the "shifted" integrated near-side per-trigger yield of various centrality of "2+1" jet functions of Cu+Cu to p+p. The "shift" is done via the S/B estimation we mentioned in Sec.5.2.2.4. The pT regions of trigger π^0 and associated charged hadrons are in the top-center legend. Of all bins, from left to right column the conditional pT requirement is non-required, [1,10GeV], [2,10GeV], [3,10GeV], [4,10GeV], [5,10GeV]. Within each bin from left to right, it's from central Cu+Cu to peripheral Cu+Cu until p+p.

5.3 Summary of Results

In this chapter I list the physical analysis I have been doing in the recent 5 years (2003-2008). I concentrated on the jet analysis, and explored the medium effect on jet correlation, via compare AA collisions to p+p. Various physical observables have been used, including width, yield, p_{Tout}. New technologies on analysis are applied into getting the result, such as "2+1" correlation, plus those well-known ones including ZYAM. By the centrality dependence of jet function "2+1" has shown us, we are probably approaching our object of understanding (and removing if possible) the surface-bias in jet reconstruction.

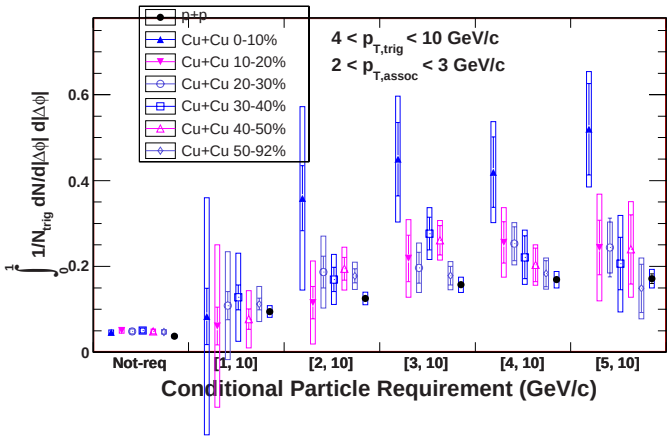

Figure 5.43 In this plot we compare the "shifted" integrated near-side per-trigger yield of various centrality of "2+1" jet functions of Cu+Cu to p+p. The "shift" is done via the S/B estimation we mentioned in Sec.5.2.2.4. The pT regions of trigger π^0 and associated charged hadrons are in the top-center legend. Of all bins, from left to right column the conditional pT requirement is non-required, [1,10GeV], [2,10GeV], [3,10GeV], [4,10GeV], [5,10GeV]. Within each bin from left to right, it's from central Cu+Cu to peripheral Cu+Cu until p+p.

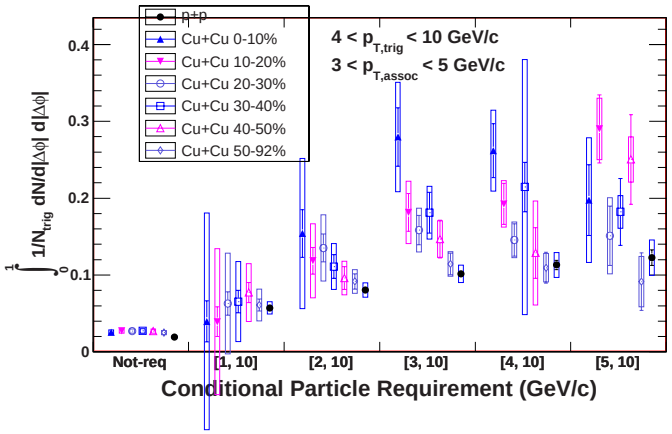

Figure 5.44 In this plot we compare the "shifted" integrated near-side per-trigger yield of various centrality of "2+1" jet functions of Cu+Cu to p+p. The "shift" is done via the S/B estimation we mentioned in Sec.5.2.2.4. The pT regions of trigger π^0 and associated charged hadrons are in the top-center legend. Of all bins, from left to right column the conditional pT requirement is non-required, [1,10GeV], [2,10GeV], [3,10GeV], [4,10GeV], [5,10GeV]. Within each bin from left to right, it's from central Cu+Cu to peripheral Cu+Cu until p+p.

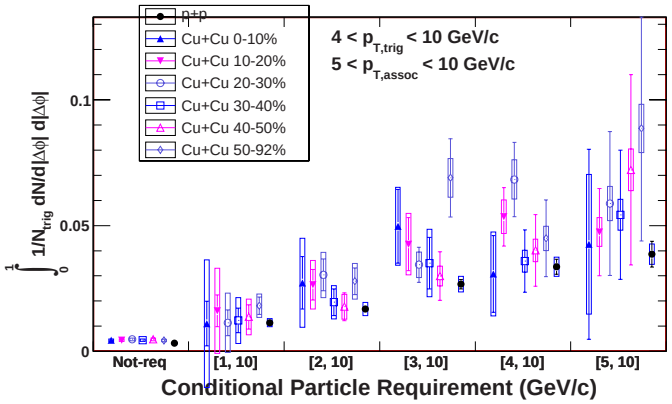

Figure 5.45 In this plot we compare the "shifted" integrated near-side per-trigger yield of various centrality of "2+1" jet functions of Cu+Cu to p+p. The "shift" is done via the S/B estimation we mentioned in Sec.5.2.2.4. The pT regions of trigger π^0 and associated charged hadrons are in the top-center legend. Of all bins, from left to right column the conditional pT requirement is non-required, [1,10GeV], [2,10GeV], [3,10GeV], [4,10GeV], [5,10GeV]. Within each bin from left to right, it's from central Cu+Cu to peripheral Cu+Cu until p+p.

CHAPTER 6. Heavy Quark Measurement and Detector Upgrade

In the previous chapters we have introduced that a jet can be used as a powerful tool in study of the medium properties. In the 2-particle or 2+1 particle correlation we have been using, these particles are either π^0 or charged hadrons, most of which are of light quark flavor, such as pion/kaon/proton. Beyond this region, heavy-flavor (open charm and beauty) production provides a wide-ranging palette of key information in broader areas of physics, especially on the high-density matter created early during the reaction.

Specifically, these measurements will determine:

• mass dependence of the energy-loss of partons in the medium, which has already been observed for light partons.

• mass dependence of the elliptic flow of quarks

• if heavy-quarks are produced only in the initial parton-parton collisions or also during the later phases of the collision.

• a firm baseline to quantify the suppression or possible enhancement of J/Ψ.

• the rate of thermal di-lepton emission quantitatively.

• quark confinement forces at larger binding energies via the yield of upsilon states.

Current experiments at RHIC cannot fully exploit the opportunities heavy-flavor production provides. Many of the necessary measurements, requiring a full azimuthal acceptance and reconstruction of heavy-flavor decay vertex, are either not possible or can be performed only with very limited accuracy. The proposed Silicon Vertex Detector (VTX) adds tracking capabilities to the central arms of the PHENIX experiment. With this detector charged particles detected in the central arms can be identified as decay products from charm or beauty carrying

particles by the displacement of their trajectories to the collision vertex. A broad pT range for charm and beauty measurements can be achieved by using different decay channels to reach different parts of phase space. The (nearly) full azimuthal acceptance of VTX detector also will improve the efficiency of single particles and jets reconstruction dramatically.

The addition of the VTX to PHENIX will provide robust charm measurement and jet reconstruction over large acceptance significantly extend the x-range of the currently possible measurements. My thesis work will be expanded greatly due to the installation of VTX.

I have been actively participating this VTX project from 2002 ever since its early stage of R&D.

My first job in this group was part of the early design work of VTX, where I did simulation of doping density of p-wells in the Strip-Pixel (Sec.6.2.3) sensor design.

Then from 2003 I have made big effort in the simulation of VTX geometry via high-pT particles. This simulation work includes the development of code, testing algorithms of track reconstruction in VTX material, and optimizing the VTX detector geometry. The optimization of detector design by checking the simulation result, including the filtering heavy-flavor meson such as D^0 using DCA (Sec.6.2.4.1) cut and Kalman Fitting (Sec.6.2.4.4), has been an important part.

Beginning from 2005, I actively took part in the testing of newly-produced strip-pixel sensors. I made contributions on the improvement of testing station at BNL. Now multiple batches of strip-pixel sensors have been tested there, and a well-written archive system has been setup.

All my work have been included in the PHENIX VTX proposal. This VTX proposal is written and includes work by the whole VTX group up to 2006. They will be introduced in the following sections of this chapter. I also cite in this chapter quite amount of content from this VTX proposal, especially in the discussion section of heavy-quark physics.

6.1 Improvement of Heavy Quark and Jet Measurements by VTX

6.1.1 Heavy Quark Improvment by VTX

The four RHIC experiments have concluded that a high density partonic matter is formed at central Au+Au collisions at RHIC(93; 94; 95; 96). Charm and beauty production, measured as yield and spectra of heavy flavor mesons, provide information about the earliest stages of heavy ion collision. Several key measurements discussed in the following sub-sections can be made with the addition of VTX detector to PHENIX. Of particular importance is the broad reach in transverse momentum, which extends PHENIXs existing capability to measure low-pT open charm. PHENIX has extracted the cross-section for open charm via inclusive electron spectra(97; 98). This method relies on the fact that a fraction of the electrons originates from decays of heavy-flavor mesons (charm or beauty). The analyzers need to subtract the large background from light-meson decays. This procedure suffers from uncertainties due to the limited knowledge of the background sources that are subtracted. In addition, one can not distinguish between electrons from charm and beauty at high pT where the contributions from the two sources become comparable. Statistical analysis have been applied in PHENIX and STAR to disentangle the electron-hadron correlation shape between charm and beauty, but this method itself requires a very precise simulation of charm/beauty jets, which is itself our goal.

The addition of a silicon vertex detector to PHENIX will allow more accurate determination of the heavy-quark component in electron spectra. Requiring the leptons to be displaced from the collision will substantially reduce the background and thus extend the range of the charm measurement to smaller pT. At moderate and high pT region, decays of beauty-flavor mesons also contribute to the single-electron spectrum. The present PHENIX detector cannot distinguish the charm from the beauty contribution and thus our ability to measure charm is limited to $p_T < 2.5$GeV/c. This is right the range where charm is the dominant source of single electrons after background subtraction. The proposed upgrade adds the capability to detect charm and beauty production separately with high accuracy, which will enable us to measure

not only the yield of open beauty production but also to extend the charm measurement to higher pT. Complementary to the measurement of inclusive electrons with displaced vertex, at high pT we can also measure exclusive decays such as $D \rightarrow K\pi$.

With the extended capability of heavy quark measurement with the VTX detector, we can address the following critical questions.

6.1.1.1 Energy-loss of heavy-quarks

Colored high-pT partons are predicted to lose energy as they propagate through the dense nuclear medium. As we claimed in the introduction chapter.1, there are two competing energy-loss mechanisms. The traditional one is the medium-induced gluon radiation (99)(100), while recently the elastic collisions with lower-energy partons has been suggested to also play an important role. This predicted parton energy loss has been observed at RHIC as strong suppression of high pT hadrons in central Au+Au collisions (101)(102). The absence of such suppression in direct photon production (103) has confirmed that it is a medium effect. In Fig.6.1 we show nuclear modification factor data for π^0, π, and direct photon measured by PHENIX (104). For light hadrons, strong suppression of a factor of $\sim$5 at a broad p_T range is observed, while direct photon is not suppressed. This quenching effect is the key evidence of formation of dense partonic matter at RHIC.

However, the gluon radiation and energy-loss are exquisitely sensitive to interference effects, since the gluon formation time is comparable to the time between successive collisions. Hence we need to be confident that the interference effects in the model calculations are well tested by a broader range of data. One powerful strategy is to change the amount of gluon-interference by using heavy-quarks instead of light quarks. Heavy-quarks are predicted (105) to lose less energy in the plasma because of the "dead-cone effect". Qualitatively the large quark mass eliminates the favored collinear gluon bremsstrahlung. It also shortens the gluon formation time and leads to a distinctly different destructive interference around the heavy-quark's trajectory.

In previous calculations, the ratio of jet quenching factor QH/QL for heavy quarks (QH) and light quarks (QL) as function of the pT of the quark calculated in reference (105). The

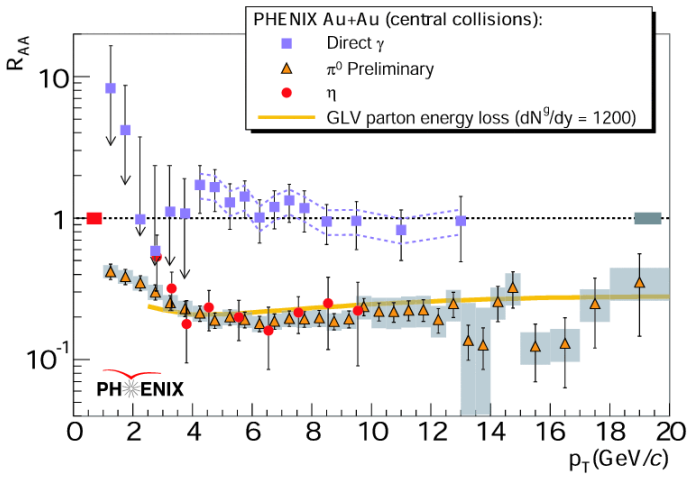

Figure 6.1 Nuclear modification factor of π^0, π and direct photon in central Au+Au collisions

smaller energy loss due to the "dead cone" effect leads to a factor of 2 less suppression of high pT charm quarks compared to light quarks. But more recent theoretical studies suggest that the magnitude of the dead-cone (106)(107)(108) may be smaller than anticipated in (105), which would lead to an energy-loss for heavy quarks closer to that for light quarks. Djordjevic and Gyulassy (106)(107) have proposed that the energy-loss for heavy-quarks is further reduced due to a plasmon frequency cut-off effect in a thermalized medium. As a result precise measurement of heavy-quark energy loss through open charm may enable a measurement of partonic effective thermal masses in the medium.

The heavy-quark measurement in PHENIX has been done through non-photonic electrons (109; 110). The PHENIX data of nuclear modification factor of high-pT single electrons are

shown in Fig.6.2. The observed suppression at central Au+Au collisions is surprisingly strong and comparable to that of light hadrons. The data provide strong constraints on the energy loss models. It is particularly remarkable that the suppression is strong at high pT $> 3GeV/c$, where the contribution from beauty decay is expected to be dominant, since in most energy loss models little or no energy loss of beauty is expected in the dense matter created at RHIC. The present PHENIX can not distinguish single electrons from charm decay and from beauty decay in Au+Au collisions. Thus we can not determine the suppression factor of charm accurately, nor we can determine if beauty also suffer significant energy loss or not. That's why we need the VTX detector to measure the single electrons from charm and beauty separately. Since beauty has a larger lifetime (B0: 462 μm, B+: 502 μm) than charm (D0: 123 μm, D+: 317 μm), we can accurately split the beauty component of single electron from the charm component, once we have the ability of a precise displaced vertex measurement from the VTX. The VTX detector will also allow us to measure the high-pT spectra of charm directly via the hadronic decay channels, e.g. $D \rightarrow K/\pi$. From these measurements, we will be able to determine the energy loss of charm and beauty in the medium. This will be a decisive measurement to understand the energy loss mechanism in the dense matter at RHIC.

The improved open charm production measurement by VTX also works as a reference to J/Ψ suppression and enhancement. It is better if we can compare J/Ψ production to open-charm production, where the initial-state effects are probably the same. This comparisons of open and closed charm help to test different theoretical models. For example it's predicted in paper(113) that the effective gluon distributions are process dependent, and leads to different for e.g. open- and closed-charm production.

6.1.1.2 Elliptic flow of heavy quarks and its mass dependence

As we claimed in previous chapters, the event anisotropy is one of the most important observables in nucleus-nucleus collisions at RHIC. The large anisotropy amplitude, v_2, provides key evidence of the formation of a hot and dense partonic matter in Au+Au collisions at RHIC. Along with the discovery of jet quenching, the observation of large v2 in Au+Au collisions is

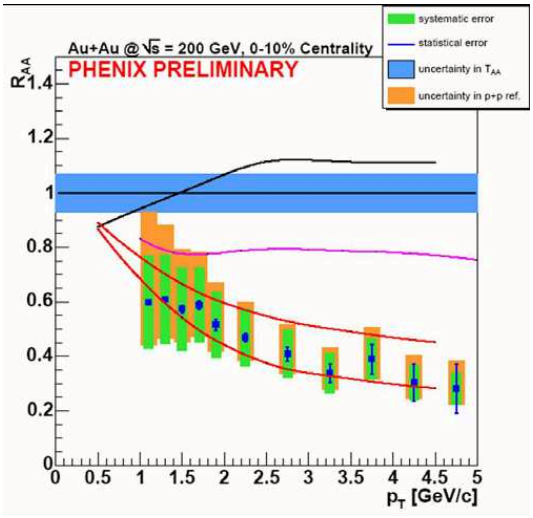

Figure 6.2 Nuclear modification factor of single electrons measured by PHENIX is compared with the theoretical predictions. The black curve is the theoretical prediction with no charm energy loss. The two red curves are prediction by N. Armestro (111) , and the magenta curve is prediction by M. Djordjevic (112) . The latter includes the contribution from beauty, which reduces the suppression at high pT.

the basis of the conclusion in the RHIC white papers (115) that a high density partonic medium is formed. In early RHIC runs, the measurements of v2 were mainly focused on that of light hadrons in low pT $< 2 - 3GeV/c$. In this dynamic region good agreement between the data and theory predictions of ideal hydrodynamic models indicate that the produced dense matter thermalizes very rapidly, and that the produced matter behaves almost as an ideal fluid.

Recently, we have observed that event anisotropy is not limited to light hadrons. A large v2 of single electrons from heavy quark decay is measured as in Fig.6.3 This is a surprising discovery, showing that even heavy quarks participate in the collective motion of the produced matter. The data pose a challenge to the theories of energy loss and thermalization mechanism of heavy quarks in the dense matter. Any theory on the heavy-quark production and energy-loss has also to explain the source of v_2.

From experimental point of view, the present PHENIX detector can not distinguish single electrons from charm and beauty. Therefore, we can not determine v2 of charm and beauty contributions separately. For example, the data shown in Fig.6.3, it is very intriguing that the

v2 strength seems to be reduced at high pT $> 2.5 GeV/c$, where significant B decay contribution is expected. Because the v2 of the beauty quark is expected by theorists to be small due to its large mass, separation of charm and beauty components by the VTX detector will enable us to measure v2 of charm and beauty separately and test this assumption. Such measurements will be the key to understand the interaction between the medium and the partons in the medium, together with the v2 data of light mesons,

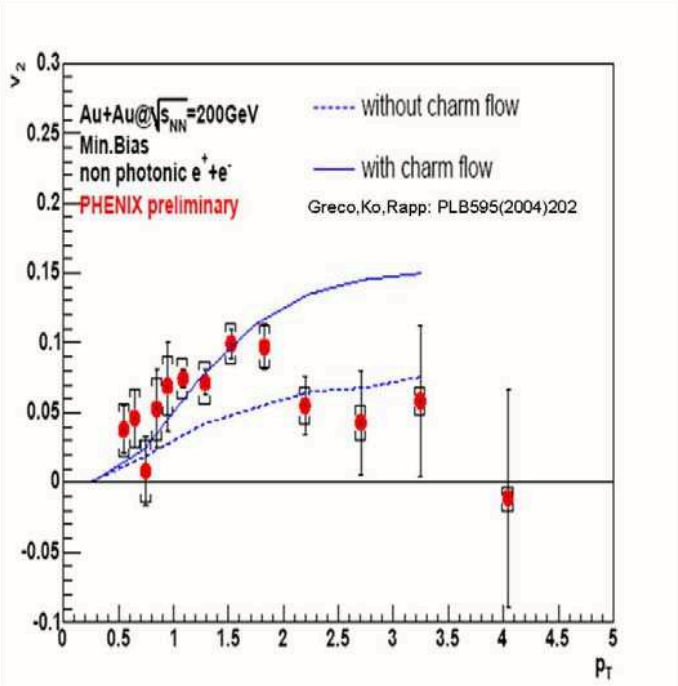

Figure 6.3 Elliptic flow strength, v2, of single electrons from heavy flavor decay measured by PHENIX. A strong elliptic flow is evidence for strong coupling QGP.

6.1.2 Di-jet Correlation and Gamma-jet Correlation Improvement by VTX

Another benefit of the VTX detector is measurement of di-jet correlation of two high-pT particles, and direct photon-hadron correlation. As we claimed in previous chapters, a strong

modification of di-jet correlations of two high pT particles is observed in (104)(114) including a mach-cone effect. This was shown in Fig.1.10. And I also told the details of near-side jet modification in AA collisions in my results chapter 5.

However, my jet analysis is still limited by the PHENIX acceptance. The VTX detector provides a large solid angle coverage that is ideal for di-jet hadron correlation measurement. Although the momentum resolution by the VTX detector alone is limited to be about 20% in $\delta p/p$, the resolution is sufficient for selecting high pT hadrons from the recoil jets. The large pseudo-rapidity coverage ($|\eta| < 1.2$) of the VTX is in particular essential for the measurement. Similarly, we will be able to utilize the VTX detector in direct photon-hadron correlation measurement in heavy ion collision. This measurement is very important, since one can directly measure the modification of parton fragmentation by the dense medium.

6.1.3 Summary of VTX Advantage

In summary, the silicon vertex barrel, which covers the existing PHENIX central arm mid-rapidity range ($|\eta| < 0.35$), addresses the following physics in AA collisions :

• Charm and beauty cross-section at high pT and mid-rapidity via high-pT electrons and also exclusive decays such as $D \rightarrow K/\pi$.

• Charm measurements at mid-rapidity as a baseline for J/Ψ production, i.e. for comparisons of open and closed charm which should share the same initial-state effects in nuclei.

• Accurate measurement of nuclear dependence of charm cross section.

• Comparison of light and heavy-quark pT distribution to determine differences in energy loss and Cronin effects.

• Full di-jet and gamma-jet reconstruction with better coverage and resolution.

Other advantages of VTX not discussed in this thesis include:

• A gluon structure measurement in the anti-shadowing region as a baseline for shadowing measurements at small x.

• Low-mass electron pairs and anti-quark shadowing at small x values.

• Beauty cross sections at mid-rapidity as a constraint on the contributions of $B \rightarrow J/\Psi$ to J/Ψ production.

6.2 VTX Detector and Physics Measurements

This section tells the technical details of VTX detector. The R&D of VTX is still going on, and the parameters in this section mainly come from the VTX proposal to Department of Energy. My work relates to this section are mainly on the strip-pixel detector (design and testing) and Monte-Carlo simulation (design optimization, via DCA and KalmanFit).

6.2.1 Overview of VTX Geometry

The VTX detector system is composed of 4 layers of silicon detectors: two inner layers with silicon pixel hybrid detectors and two outer layers with silicon strip detectors. A 3-D view of the detectors is shown in Fig. 6.5 and its cross sectional views are shown in Fig. 6.4 in the previous chapter. The current design proposal of geometrical dimensions of the pixel layers and the strip layers are summarized in tables 6.6 and 6.7, respectively.

6.2.2 Pixel Detector

For the inner two layers we use silicon pixel detectors. The inner two layers of the vertex tracker will be built based on silicon pixel devices designed for the ALICE experiment at CERN. A full telescope with 16 detector planes was installed and operational in the NA60 experiment during the physics run with high-energy Indium beams in Fall 2003, and the first physics results from the experiment have been reported in 2005. We are developing and building the inner two layers for PHENIX in close collaboration with ALICE. The technology is the ALICE1LHCb sensor-readout hybrid, which was developed at CERN for the ALICE and LHCb experiment. The 200 μm thick silicon sensor holds 32X256X4 cells, or pixels, each with an active area of 50X425 μm^2. The sensor is bump bonded to four matching readout chips of 150μm thickness,

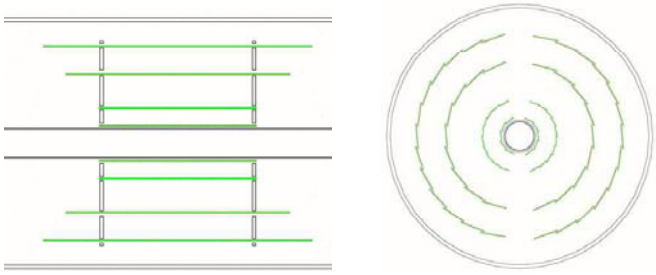

Figure 6.4 (left) Cross section of the silicon vertex tracker (VTX) along the beam axis. The inner pixel hybrid layers are located at a radial distance of 2.5 cm and 5 cm from the beam, and they extend over 22cm in beam direction. The silicon strip outer layers are located at 10 and 14 cm. The length of the 3rd and 4th layer is 32cm and 38cm, respectively, in beam direction. The Be beam pipe with 2 cm radius is also shown. (right) Cut through the silicon vertex detector in the xy-plane transverse to the beam axis. The VTX is assembled in two half shells with small acceptance gaps at top and bottom. Each half shell has 5 and 10 pixel ladders and 9 and 13 strip ladders.

and each of the read-out chips has 32X256 individual amplifier discriminator channels. The readout chip also holds the electronics to pipeline the data flow.

For PHENIX, 4 pixel read-out chip bump-bonded on a sensor chip forms a sensor module. Two sensor modules, a pixel bus and a bus extender form a half ladder, which is the basic read-out unit of the pixel detector. This sub-detector is read-out by an electronics module, Silicon Pixel Intermediate Read-Out (SPIRO) module. The SPIRO modules are placed outside of the detector acceptance. They provides all service voltages, control and timing signals, and reads out the pixel data. They process the incoming control signals and transmit the outgoing data of a pixel half ladder. A SPRIO module carries analog Pilot chips for the power and reference voltage supplies of the pixel readout chips, digital Pilot chips for their controls and readout, and an optical link chips and transmitters for the data transfer. The SPIRO modules

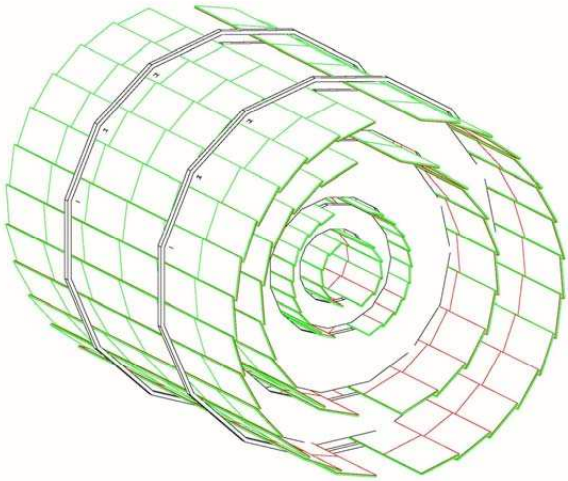

Figure 6.5 GEANT model of the VTX detector. It consisted of the inner–most pixel layer and three outer strip layers.

are then connected to pixel Front End Modules (FEMs) outside of the PHENIX IR. The FEMs work as interface to the PHENIX DAQ system. The read-out scheme of the pixel system is illustrated in Fig. 6.8.

Mechanically, two half ladders are supported on a mechanical stave, which provides mechanical support as well as cooling of the system. Two half ladders mounted on a mechanical stave form a full ladder which spans approximately 22 cm in beam direction. Five such ladders on each side of the beam pipe result in almost full azimuthal coverage. A total of 10 ladders or 20 half ladders complete the inner-most layer. The second layer is composed of 20 ladders or 40 half ladders. The combined materials of silicon sensors, readout chips, readout buses and mechanical structure including cooling add up to about 1.5% per layer of a radiation length. Table 6.6 summarizes the main parameter of the two pixel layers.

6.2.3 Silicon Strip Detector

The two outer layers employ silicon strip sensors. The sensor, developed by the BNL Instrumentation Division, allows stereoscopic readout on a single sided sensor. Each sensor is about 3.43X6.36 cm^2, with 2X384 of X-strips of 80μm width and 3.1 cm length in beam direction and the same number of U-strips at an angle of 4.60 to the beam direction. Due to

VTX	Layer	R1	R2
Geometrical dimensions	R (cm)	2.5	5
	Δz (cm)	21.8	21.8
	Area (cm^2)	280	560
	Sensor maxtrix size	1.28 cm × 1.36 cm	
	Pixel size	50 × 425 μm^2	
Channel counts	Pixels per ROC	32 × 256 = 8192	
	ROCs per sensor module	4	
	Sensor modules per half-ladder	2	
	Half-ladders per ladder	2	
	Ladders	10	20
	Readout chips	160	320
	Readout channels	1,310,720	2,621,440
Radiation length (X/X0)	Sensor (200 μm)	0.22 %	
	ROC (150 μm)	0.16 %	
	Bus	0.28 %	
	Mechanical stave	0.70 %	
	coolant	0.08%	
	Total	1.44 %	

Figure 6.6 Summary of main parameters of the inner 2 pixel layers.

the stereoscopic readout the effective pixel size is 80X1000μm. Five (for layer 3) or six (for layer 4) sensors are mounted in a ladder. The full length of a ladder in the beam direction is 31.8 cm (for layer 3) or 38.2 cm (for layer 4). A total of 44 ladders are required to cover the azimuth acceptance as shown in Fig. 6.5.

Each strip sensor is wire-bonded to and read-out by twelve read-out VTX4 ASICs, six per orientation, and there are 128 channels on each VTX4 chip. FNAL and LBNL have developed these chips for other silicon vertex detectors. The twelve VTX4s servicing each sensor are mounted on a readout cards (ROC) and are readout by a custom, digital ASICs (RCC). These chips compress and parallelize the data sufficiently to meet PHENIX readout speed requirements. Power, serial control, timing and readout for a ladder are all carried on the ROC's, which are bussed together via wire-bonding at their edges (one bus per orientation). This bus runs the length of a ladder and out of the acceptance to a Front End Module (FEM), which transmits the data via an optical fiber for further processing. The present estimate is that the mechanical support, ROC's and sensor add up to about 2.1% of a radiation length.

VTX	Layer	R3	R4
Geometrical dimensions	R (cm)	10	14
	Δz (cm)	31.8	38.2
	Area (cm^2)	1960	3400
	Sensor size	3.43 cm × 6.36 cm	
	Strip size	80 μm × 3 cm	
	Effective pixel size	80μm × 1000 μm	
Channel count	strips per sensor	384 × 2 strips × 2	
	# of channel per SVX4	128	
	SVX4 per sensor	12 (= 3 × 2 strips × 2)	
	Sensors per ladder	5	6
	# of Ladders	18	26
	# of Sensors	90	156
	SVX4	1080	1872
	Readout channels	138,240	239,616
Radiation length (X/X0)	Sensor (625 μm)	0.67 %	
	ROC	0.64 %	
	Mechanical stave	0.70 %	
	coolant	0.08%	
	Total	2.1 %	

Figure 6.7 Summary of main parameters of the 2 strip layers.

6.2.3.1 New Strip Sensor Design

We have developed an improved design of the strip-pixel sensor as in Fig.6.9, which matches the strip ladder detector design including the ROC described below. This spiral-structure design has the x-strip (x-axis) and u-strip (y-axis) on the same level of sensor.

As you see in Fig.6.9, in each pixel the x-strip and u-strip doping spiral around each other, and each goes to their own next pixel and later on their own read outpads by metal (aluminum). Each half-sensor contains 384 x-strips and 384 u-strips. The two half-sensors are 180-degree rotating-symmetric. By this design, we keep the x- and u- strips on the same horizontal level of sensor and we have a better space resolution, comparing to the "traditional" design where x- and u- strips are on two vertical neighboring pixels.

The readout pads are located in the longer-edge of the sensor in Fig.6.10, so as to make a room for RCC in the center of the sensor and for bus connections between ROCs in the 2nd aluminum layer. To eliminate dead space, the 30 U-strips in the upper-side of the half-sensor is connected to the U-strips in the lower-side, also in the 2nd aluminum layer. Aluminum lines connected to the inner guard ring are added around the readout pads to make the sensor tests easier. The modified design is developed with Hamamatsu.

The strip-pixel structure of 80μm X 1000μm pixel with 5μm width and 3μm gap p+ line

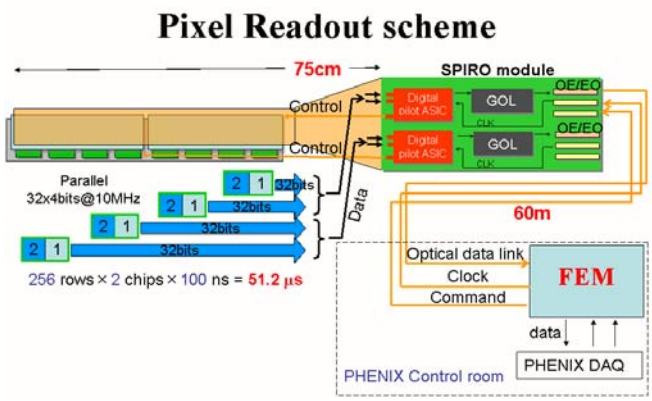

Figure 40 Schematic diagram of pixel electronic system

Figure 6.8 Read-out Scheme of Pixel Detectors in VTX

was kept. The production of sensors with this improved design was done by Hamamatsu as a part of the preproduction process described below. The first new sensor of the preproduction was delivered in 2005.

6.2.3.2 Strip Testing

Testing facilities have been set up at Brookhaven National Laboratory (BNL), Stony Brook University (SBU) and University of New Mexico (UNM) to perform Quality Assurance (QA) tests on the strip-pixel sensors. Each of the laboratories is equipped with a clean room containing a probe station. The UNM and SBU testing facilities were previously devoted to silicon testing for the CDF and DO experiments, respectively. I joined the testing work at BNL since 2005, and helped in both testing-station setup and the actual strip wafer/sensor testing. I also joined the work of primary strip ROC testing at Oak Ridge National Lab in 2006.

The testing procedures have been developed in the process of testing several rounds of test production sensors. Two vendors, Hamamatsu (HPK) and SINTEF were chosen to produce the prototypes. This test production involved two different designs that we have designated "old" and "new". The new design incorporates several features optimized for present design of the strip read-out card (ROC). The old design sensors were ordered from both SINTEF and

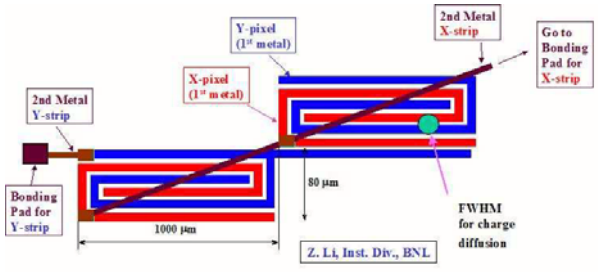

Figure 6.9 A schematic view of p+ cathode structure of the strip-pixel sensor.

HPK, but only HPK was able to produce new design sensors. Fig.6.11 shows the old design sensors on the left panel, the new design sensors on are presented in the middle panel and the diced wafer on the right panel. The dicing was done at the instrumentation division at BNL.

In the first preproduction delivery, a total of 3 new design prototype wafers (9 sensors) with thickness of 625μm were delivered by HPK. Upon request HPK produced 3 wafers (9 sensors) of 500μm wafers by thinning a subset of the 625μm wafers. The dicing of the first wave of the preproduction was done at the instrumentation division at BNL. Dicing of a second delivery of the preproduction was split between BNL and HPK, and had 14 new design 625μm thick sensors. All of the 625μm and the majority of the 500μm have been subjected to a battery of QA tests. Each sensor underwent a visual inspection. Digital images of each section of the sensor were stored for future reference. On each sensor detailed I-V and C-V measurements were performed for the guard ring and a number of strips. Examples of such measurements are shown in Fig.6.12

The 500 um sensors were found to have a significantly higher leakage current (for example, the Guard Ring current was 6 uA at VDF=120 Volts) than the 625 um sensors (Guard-Ring current: 300 nA at VDF = 120 V). Similarly, strip current measurement show high leakage current for the 500 um sensors, which saturates the limit imposed by the VTX4 chips

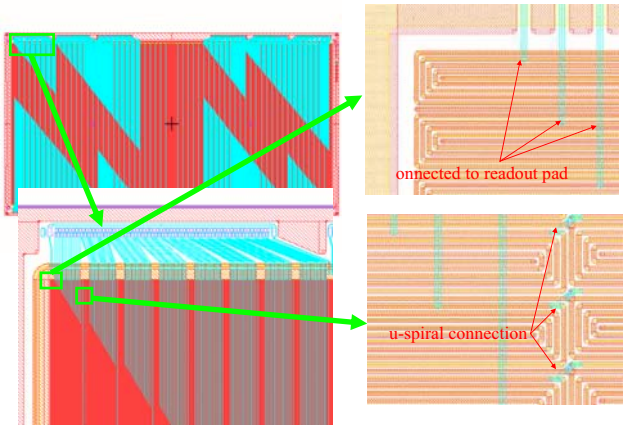

Figure 6.10 Design layout of the HPK preproduction batch of Si strip-pixel sensor.

(15nA/strip). The 625 um new design sensors bonded to the VTX4 have lower measured strip leakage current (0.4 nA/strip) and have been chosen for the detector. A more detailed test in which the current and capacitance were tested for each strip were performed at 200V. These tests are shown in Fig.6.13. The testing results are planned to be stored in a database and the results are accessible on the internet. The majority of the tests were performed at BNL and SBU. The UNM facility has performed more specialized test on irradiated sensors which are not included in current thesis design.

The test production sensors have been categorized into 4 classes. Sensors are classified based on bulk characteristics whether or not the sensor demonstrates a clear full depletion region and high breakdown voltage and strip measurements the number of strips that show abnormal current and capacitance. Class definitions have been used to determine which type of tests each sensor is appropriate for. For example, the telescope tests in which the sensors are bonded to ROCs required the highest quality sensors (class I) but irradiation tests only required sensors with at least partial functionality (class I-III). For the upcoming production round QA criteria may be modified based on sensor performance in the full read-out chain.

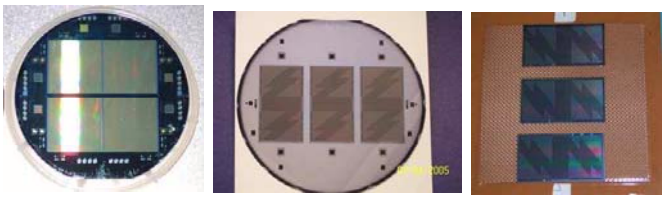

Figure 6.11 Left: A SINTEF wafer containing two "old" design sensors. Middle: A Hamamatsu wafer before dicing containing three "new" design sensors. Test diodes are seen along periphery of the wafers. Right: A Hamamatsu wafer diced at the Instrumentation division at BNL.

6.2.4 Simulation of Physics Measurements with the VTX Detector

The proposed VTX detector provides us the tool to measure new physics observables that are to date not accessible at RHIC or available only with very limited accuracy. These include a precise determination of the charm production cross section and transverse momentum spectra, particularly at high pT, a measurement of beauty, and the detection of recoil jets in direct photon production. In this section, we discuss how the proposed VTX detector makes these measurements possible, or significantly improves our capability to address these observables.

Simulation work is done mainly through a GEANT4-based PHENIX software called PISA. . This software PISA accepts most available simulation input format, and particles go through all existing PHENIX detector volumes.

My simulation is done by PISA, on DCA and KalmanFit of high-pT pions and heavy-flavor mesons D and D^0. The effect of DCA resolution and KalmanFit is used to optimize the VTX layout design.

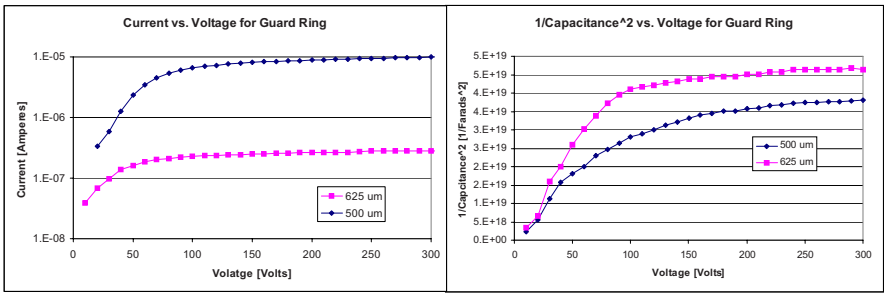

Figure 6.12 Left panel: I-V curves of Guard Ring obtained from two sensors with different thicknesses(500 um and 625 um). Right panel: C-V curves obtained from the same sensors used for I-V tests.

6.2.4.1 Design Considerations and the VTX detector geometry

A variety of simulations and first principle calculations have shown that the displacement resolution is dominated by the position accuracy of the two inner most detector layers and by the amount of multiple-scattering between the collision point and the two position measurements. Assuming that the multiple scattering occurs at the location of the first layer, the Distance to the Closest Approach (DCA) of a trajectory to the beam axis in the main bend plane can be measured with a resolution given approximated by the r and ϕ resolution and radial position of the first and second layer, respectively. The average multiple-scattering angle, denoted by θ_{ms}, is given by the beam pipe thickness and the first detector layer. The calculation of DCA quantifies both the contribution due to the finite position resolutions and the effect of the multiple scattering. Given standard silicon detector segmentation of 50 to 100 um in rϕ and a typical thickness of 1 to 2% of a radiation length, both terms of DCA

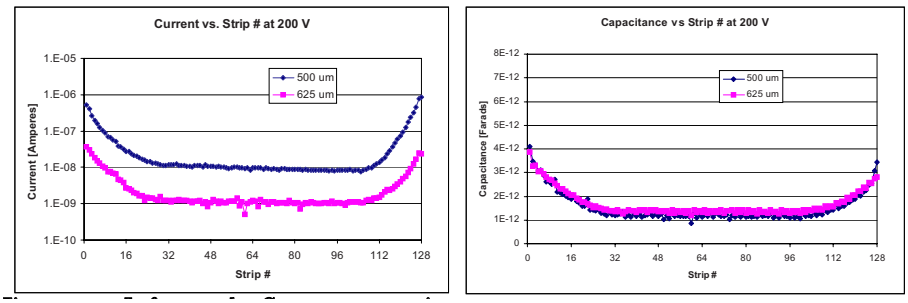

Figure 6.13 Left panel: Current vs. strip obtained from two sensors with different thicknesses (500 um and 625 um). Right panel: Capacitance vs. strip obtained from the same sensors presented in left panel. Rises on edges of both plots is due to edge effects of the grounding scheme when measuring with a probe card.

contribute to the final resolution. We tested the VTX design with a "straw man" layout in simulation software, which is discussed below. The typical DCA resolution from this estimate is $\sim 40\mu$m: a value confirmed by detailed simulations. In order to minimize the DCA resolution, the hard-scattering from the beam-pipe and first layer is to be minimized. Hence the first layer should be as close to the collision point as is practical, which at RHIC is about 2 cm (requiring a modification of existing beam-pipe by the proposal), and the first layer plus beam-pipe should be as thin as possible.

6.2.4.2 Central Track VTX matching

In order to make full use of the VTX capabilities, tracks reconstructed in the central arms have to be matched to hits or track segments in the VTX. We use the known magnetic field to project central arm tracks to each of the layers in the VTX. Fig.6.14 shows the residual

between the track projection of 2 GeV/c pions and the hit location in ϕ and z for the inner-most pixel layer. The hit positions in the VTX detector have not been used at this stage of the track and hit matching. The distributions are centered at zero and have a width of 5 mrad and 0.05 cm. Similar residual distributions are found for each of the four VTX layers.

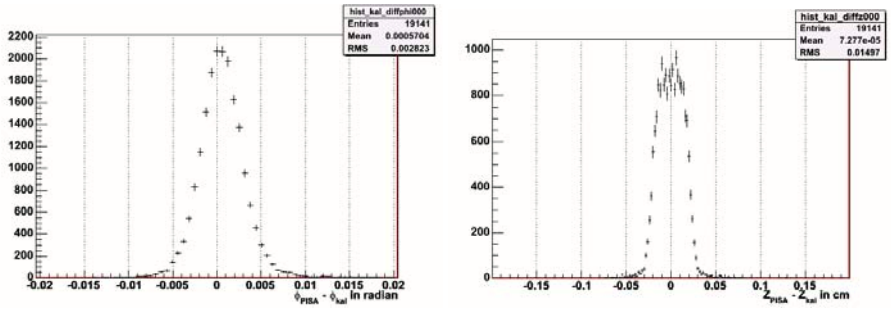

Figure 6.14 The residual between track projection and hit location in ϕ and z for the innermost pixel layer. This simulation is for 2 GeV/c pions.

For tracks from $D \rightarrow K/\pi$ decays the residual distribution is expected to be broader, since the central arm tracking assumes the track originated at the collision vertex. This is verified in Fig. 6.15, which shows the residuals for tracks from $D \rightarrow K/\pi$ decays, again the inner-most layer of the VTX. The residuals are significantly larger than for primary tracks. It is important to choose the matching criteria for hits to central arm tracks to be broad enough to include also the tracks from open charm and beauty decays. For each VTX layer the hit-association assigns to each central arm track the hit closest to the track projection within a certain window. Currently the size of the window is taken to be 30 mrad in ϕ and 0.15 cm in z for the pixel layers, i.e. several times the widths of the residuals found in the $D \rightarrow K/\pi$ decay shown in Fig.

6.15. The window size is changed to 30 mrad in ϕ and 0.45 cm in z for the strip layers. A future improvement of the algorithm will be based on momentum dependent matching window.

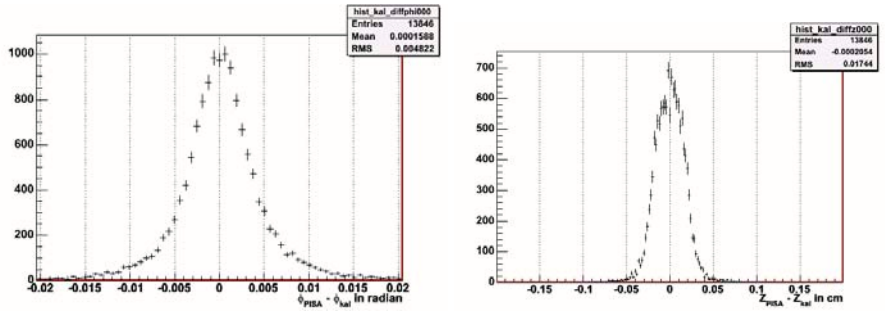

Figure 6.15 The residual between track projection and hit location in ϕ and z for the innermost pixel layer. The VTX hits are not included in the fit. This simulation is for $D \rightarrow K/\pi$ at pT = 2 GeV/c.

The number of random charged particles inside of the initial matching window is about 0.1 for the most central Au+Au collisions. The matching window size can be further reduced after the track fitting using the hits in the VTX, eliminating most accidental matches. The residual distribution between the track fit and the VTX hit position in the inner-most pixel layer is shown in Fig. 6.16 for prompt pion and in Fig. 6.17 for particle from $D \rightarrow K/\pi$ decay. The RMS width in ϕ and z are reduced to 1.6 mrad and 126μm for prompt pion at 2 GeV/c. For tracks from $D \rightarrow K/\pi$ decays, which have lower momentum in average, the RMS width of the residual is 2.2 mrad and 150μm. The solid angle of the 3σ matching window is then reduced to about 0.1 mstr and the occupancy in the window is about 1% for the most central collision.

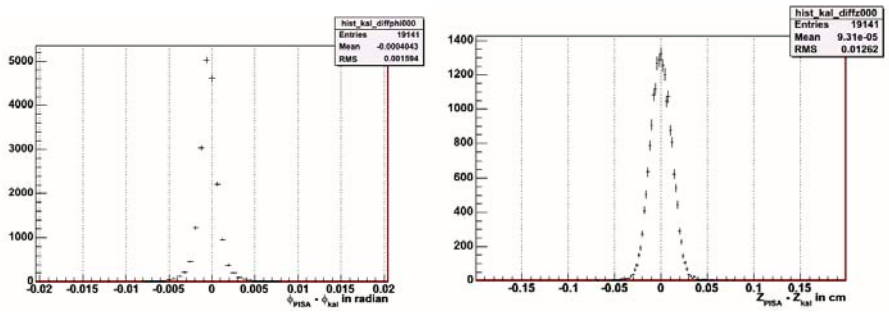

Figure 6.16 The residual between the track and the hit location in ϕ and z for the inner-most pixel layer after the hits in the VTX are included. This simulation is for 2 GeV/c pion.

6.2.4.3 DCA measurement by the inner two layers

After the hits in the VTX detector are associated with the track, the distance of closest approach of the track to the primary event vertex (DCA) is calculated in the plane transverse to the beam. We base this calculation on the inner-most two pixel layers. Fig. 6.18 shows the DCA distribution for pions at pT = 2 GeV/c. A DCA resolution of 36μm is achieved, which is consistent with the 50μm pixel width of the detector.

We have also evaluated the effect of the hit occupancy expected in central Au+Au collisions on the matching resolution. The statistics of this simulation is limited, but the result shows that the resolution only slightly deteriorates. For example, for the inner most pixel layer, the RMS of the residual in ϕ increases from 2.2 mrad to 2.5 mrad, and the RMS of the residual in z increase from 150μm to 230μm.

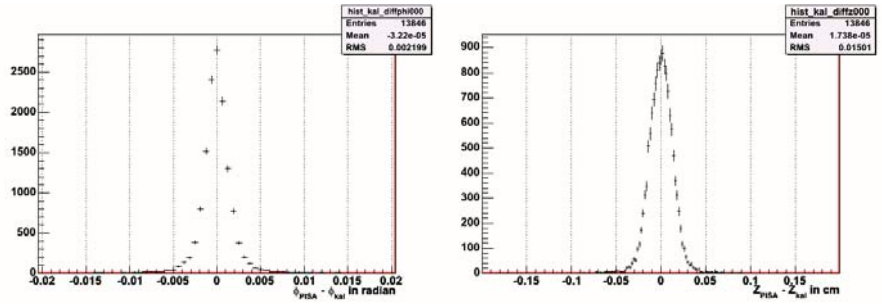

Figure 6.17 The residual between the track and the hit location in ϕ and z for the inner-most pixel layer after the hits in the VTX are included. This simulation is for $D \rightarrow K/\pi$ at pT = 2 GeV/c.

6.2.4.4 Central Au+Au simulation — Kalman fitting

A track fitting code using a Kalman filter technique has been developed for the VTX detector by Iowa State University group.

This code is commit now into PHENIX CVS, at /offline/packages/KalmanFit.

In this code, a track reconstructed from the PHENIX central arms is projected on the VTX detector and is associated with the hits on the silicon detector layers. Then the distance of the closest approach (DCA) of the track to the primary collision vertex is calculated. This Kalman code performed a global fit of the hits in VTX tracker and the track reconstructed in the PHENIX central arms. The effect of the multiple scattering is taken into account in the global fit. Each hard-scattering with material is a matrix multiplied on the fitting process. The final out of Kalman code is a 7-element vector, the 3-D position, 3-D momentum, and beginning time of one particle at its origin. The χ^2 of Kalman fitting is also recorded as a

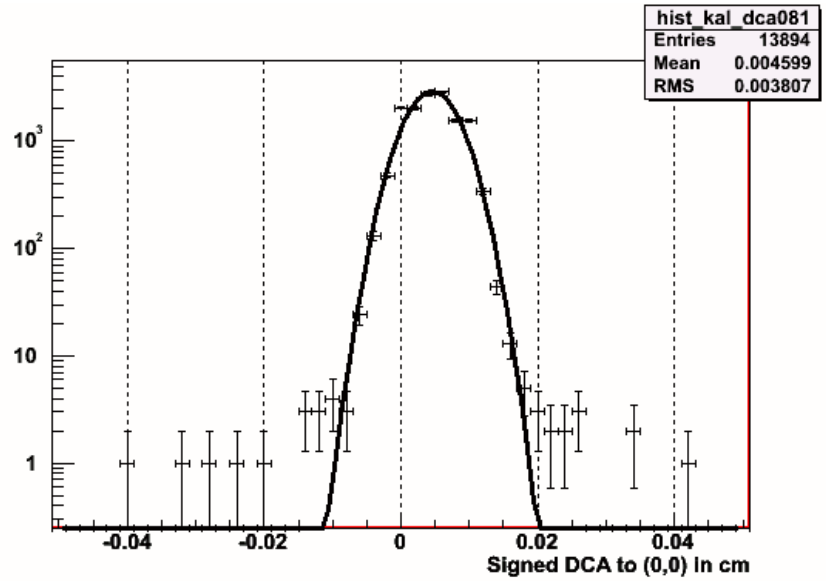

Figure 6.18 The DCA distribution for 2 GeV/c pions in the PISA simulation of the VTX detector. The DCA resolution of $\sigma = 36\mu$m was achieved using the two inner-most two pixel layers.

quality cut.

The code is evaluated using the simulated events from a GEANT simulation of VTX detector in PHENIX. The simulated tracks are reconstructed by the standard PHENIX reconstruction program, and then they are connected with the VTX detector using the Kalman fit program. Results from the simulation are shown in Fig. 6.19. In both panels of the figure, the black histograms show the DCA distribution of the tracks from the primary vertex in simulated central Au+Au collision events, and the red histograms show that of charged tracks from simulated $D \rightarrow K/\pi$ decays. In the right panel, very loose chi-squares cut ($\chi^2 < 999$) is applied, and the DCA distribution of the primary tracks has a very long tail caused by high multiplicity of the event. This long tail would prevent clear separation of charm decay tracks from background tracks. In the left panel, the tail is cleaned up by a tight chi-squares cut, and the primary vertex has a Gaussian DCA distribution. The simulation demonstrates that VTX detector can clearly separate charm decay tracks and background tracks.

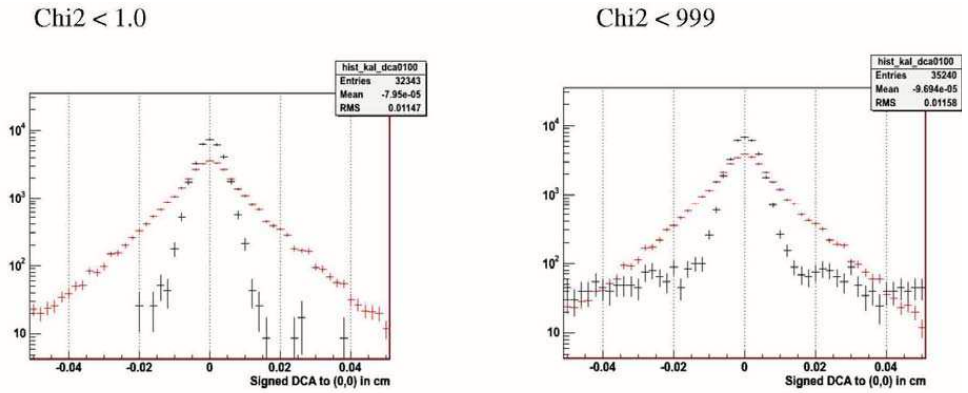

Figure 6.19 DCA distribution of tracks from D0 decays (red) and that from primary vertex (black) from simulation. In the right panel, a very loose chi-squares cut is applied, while a tight chi-squared cut is applied in the left.

6.2.4.5 Improved momentum resolution and pT resolution

In the present PHENIX detector, drift chambers that are located outside of the central magnet measure the momentum of the charged particles. Since there is little magnetic field at the location of the drift chambers, charged particles traverse them on almost straight trajectories. The momentum p of a particle is related to the bending angle α measured at the drift chamber approximately as $\delta p/p \sim 87$ mrad/p (p in GeV/c). The momentum resolution of the central detector will be much improved with the VTX detector. This is because in the present PHENIX central arm spectrometers the effective field kick of 87 mrad GeV/c is only about 40% of the total angular deflection $\Delta\phi$ in the magnetic field. The field integral at the location of the drift chamber is about 0.7 Tm, which gives $\Delta\phi = 210$ mrad /p. Since the VTX measures the initial direction of the particles the full value of $\Delta\phi$ is measured rather than the angle α at

the edge of the magnetic field. In addition, a second field coil, which has been installed in 2003, allows increasing the field integral to roughly 1 Tm. With this field integral the total field-kick increases to 300 mrad GeV/c. The improvement in momentum resolution is calculated by the ratio of the field kicks $\Delta\phi/\alpha \approx$ 200mrad / 87mrad $\sim$ 3. The higher momentum resolution with the VTX detector will improve the high pT measurements. At present, a momentum resolution of about 1%/p has been achieved. With the VTX detector, the resolution of a 30 GeV/c track can be reduced from 30% to about 10%. In addition, the track confirmation close to the vertex provided by the VTX will eliminate the decay and conversion background, which currently limits the pT reach of the PHENIX charged particle tracking to $p_T < 10$GeV/c.

CHAPTER 7. Conclusions and Future Measurements

7.1 Summary of Physical Measurements

The main goal of analysis work in this thesis is to utilize jet modification as a probe to study the properties of medium in RHIC high-energy AA collisions. To achieve this purpose, 2-particle correlation was measured. We selected high-pT π^0 as trigger to tag the jets, since it's the highest-energy identified particle accessible in PHENIX. And charged hadrons are used as associated particles.

We studied the near-side jet function via multiple physical observables, including width, yield, p_{Tout}. Both PHENIX 200GeV Au+Au and Cu+Cu data have been studied, and compared to p+p with the same PHENIX detectors. The width study of Au+Au and Cu+Cu indicate a narrower near-side width at central AA collisions compared to 200GeV p+p. The near-side p_{Tout} of Cu+Cu shows a possible broadening at higher p_{Tout} compared to p+p, but the p+p data needs to be finalized before we can make further claims.

To gain further control on the path-lengths partons travel through the medium and remove possible surface-bias, we applied several methods in our analysis.

One method is the well-known reaction-plane method, where we select trigger within different azimuthal region relative to the reaction plane. Then we study the near-side jet shape as a function of this relative angle, comparing those of in-plane to out-plane, plus p+p/d+Au as a reference. This reaction-plane analysis was applied to Run 2004 Au+Au data. Within current statistical/systematic errors, we did not observe reaction-plane dependence of near-side jet shapes in their widths.

Then we concentrated on a new technology called "2+1" correlation, where we required one extra "conditional" high-pT charged hadron on the far-side, besides the high-pT trigger

π^0 and associated charged hadrons on the near side. Since this "2+1" method will statistically remove those events that have their back-to-back jets traveling most of the medium and get absorbed, we hope to partially remove the surface-bias by shifting the hard-scattering position toward the center of medium. This "2+1" method was applied to PHENIX Run 2005 Cu+Cu 200GeV data, together with Run 2005/2006 p+p 200GeV as reference. As summarized in 5, we observe centrality-dependent yields in specific bins of associated/conditional pT combination, when we fix the trigger pT region. This centrality dependence is mostly evident when the associated/conditional pT regions are close to each other. The increase in yields can possibly come from the radiated gluon of parton in medium. On the contrary, we don't observe this centrality dependence of jet yields when we don't require a "conditional" particle. This is consistent to what we observed on jet widths in Au+Au data. We have begun to work on statistically separate the "conditional" particle between those come from real back-to-back jet and those come from underlying events. Thus, the "2+1" correlation work is improving our understanding (and removing if possible) the surface-bias in jet reconstruction, so that we can have a more direct and un-biased study of medium properties.

7.2 Future Measurements

7.2.1 Existing Data

We have more work to finalize the existing analysis in order to publish the Cu+Cu data.

From experimental point of view, all analysis steps need to be confirmed. These include the finalization of warn/dead maps of EMCal, single-particle efficiencies, propagation of systematic errors such as ZYAM.

From physical point of view, the new "2+1" method still needs improvement although encouraging results have been shown. We need to better understand the centrality/conditional-pT dependence of near-side jet yields. How much of them are from the previously-suggested Q^2 shifting (91), and how much are from the shift of surface-bias we expect? We have been testing new technology on this topic in Sec.5.2.2.4, and new trend of centrality dependence has been observed. However, more work needs to be done before this technology becomes convincing.

And when methods are finalized, we will also apply them to the new Run 2007 Au+Au data, where PHENIX has more than 3 times data compared to the 2004 Au+Au 200GeV run. With the improved statistics, the systematic errors such as that of ZYAM shall also be improved. This will allow us to also include the far-side correlation shape in our analysis.

Another reason we can't do the "2+1" now on far-side shape is because the natural bias introduced by this "conditional" particle. Whether or not we include this particle into the correlation function, we are producing a strong bias to the far-side yields. This may also be solved with improved statistics, if we have a better understanding of the S/B of back-to-back jets.

7.2.2 New Observables by Detector Upgrade

All my existing correlation work are using π^0 as trigger, since this is the highest-energy identified particle PHENIX can measure currently. However, as we claimed in the chapter "Heavy Quark Measurement and Detector Upgrade" (chapter.6), it's important to tag the jets using heavier flavor particles. The comparison of jets tagged by particles of different mass/lifetime shall provide us much better probe on medium properties. This will require the direct reconstruction of heavy-flavor mesons in PHENIX, instead of the semi-lepton measurements being done. This job can't be done until the upgrades of PHENIX detectors are installed.

Of these near-future upgrades, my work have been concentrated on the Silicon-Vertex-Detector (VTX). It will greatly help the heavy-flavor meson measurement, doing direct measurement via hadron decay channel.

To achieve this object, this VTX needs a very good DCA (Sec.6.2.4.1) resolution plus a low noise level, as is shown in my work at chapter.6 New technologies including a strip-pixel design have been applied in the R&D of VTX. The VTX is planned to install into PHENIX in summer 2009.

The much bigger azimuthal and pseudo-rapidity coverage improved by VTX will also greatly help the high-pT tracking in PHENIX. So the existing charged-hadron correlation and semi-lepton cross-section measurement will also benefit from the VTX upgrade.

BIBLIOGRAPHY

[1] "Formation of dense partonic matter in relativistic nucleus-nucleus collisions at RHIC: Experimental evaluation by the PHENIX Collaboration" PHENIX QGP white paper, Nuclear Physics A Volume 757, Issues 1-2 , 8 August 2005, Pages 184-283, 2005-05-24

[2] T. D. Lee, cU-TP-170, Published in Trans.N.Y.Acad.Sci.Ser.2 v.40 1980:0111. (1979).

[3] E. V. Shuryak, Phys. Rept. 61 (1980) 71.

[4] F. Karsch, Lect. Notes Phys. 583 (2002) 209.

[5] K. Rajagopal, Acta Phys. Polon. B31 (2000) 3021.

[6] S. S. Adler, et al., Phys. Rev. C69 (2004) 034909.

[7] K. Adcox, et al., Phys. Rev. C69 (2004) 024904.

[8] E. Schnedermann, J. Sollfrank, U. W. Heinz, Phys. Rev. C48 (1993) 2462.

[9] G. Rai, Nucl. Phys. A681 (2001) 181.

[10] H. Dobler, J. Sollfrank, U. W. Heinz, Phys. Lett. B457 (1999) 353.

[11] C. Alt, et al., J. Phys. G30 (2004) S119.

[12] T. Peitzmann, Eur. Phys. J. C26 (2003) 539.

[13] M. M. Aggarwal, et al., Phys. Rev. C67 (2003) 014906.

[14] J. Adams, et al., Phys. Rev. Lett. 92 (2004) 112301.

[15] P. F. Kolb, J. Sollfrank, U. W. Heinz, Phys. Rev. C62 (2000) 054909.

[16] S. S. Adler, et al., Phys. Rev. Lett. 91 (2003) 182301.

[17] C. Adler, et al., Phys. Rev. Lett. 87 (2001) 182301.

[18] S. S. Adler, et al., nucl-ex/0411040 (2004).

[19] C. Alt, et al., Phys. Rev. C68 (2003) 034903.

[20] G. Agakichiev, et al., Phys. Rev. Lett. 92 (2004) 032301.

[21] G. Martinez and T. Vissonneau "Evaluation of centrality in Au+Au reaction classes. Glauber Model calculation including Ncoll bias for hard probes signatures.", PHENIX analysis note 242

[22] C.Y. Wong, Introduction to High-Energy Heavy-Ion Collisions, World Scientific

[23] D. Teaney, J. Lauret, E. V. Shuryak, nucl-th/0110037 (2001).

[24] *Scaling properties of azimuthal anisotropy in Au+Au and Cu+Cu collisions at* $\sqrt{s_{NN}} =$ 200 GeV **Phys. Rev. Lett. 98, 162301 (2007) , 2007-04-16**

[25] J. F. Owens, Rev. Mod. Phys. 59 (1987) 465.

[26] G. Bunce, N. Saito, J. Soffer, W. Vogelsang, Ann. Rev. Nucl. Part. Sci. 50 (2000) 525.

[27] R. Cutler, D. W. Sivers, Phys. Rev. D17 (1978) 196.

[28] S. S. Adler, et al., Phys. Rev. Lett. 91 (2003) 241803.

[29] F. Aversa, P. Chiappetta, M. Greco, J. P. Guillet, Nucl. Phys. B327 (1989) 105.

[30] B. Jager, A. Schafer, M. Stratmann, W. Vogelsang, Phys. Rev. D67 (2003) 054005.

[31] S. S. Adler, et al., nucl-ex/0409015, accepted in Phys. Rev. C (2004).

[32] J. D. Bjorken, fERMILAB-PUB-82-059-THY (1982).

[33] M. Gyulassy, M. Plumer, Phys. Lett. B243 (1990) 432.

[34] X.-N. Wang, M. Gyulassy, Phys. Rev. Lett. 68 (1992) 1480.

[35] X.-N. Wang, M. Gyulassy, M. Plumer, Phys. Rev. D51 (1995) 3436.

[36] R. Baier, Y. L. Dokshitzer, S. Peigne, D. Schiff, Phys. Lett. B345 (1995) 277.

[37] R. Baier, Y. L. Dokshitzer, A. H. Mueller, S. Peigne, D. Schiff, Nucl. Phys. B483 (1997) 291.

[38] R. Baier, Y. L. Dokshitzer, A. H. Mueller, D. Schiff, Phys. Rev. C58 (1998) 1706.

[39] M. Gyulassy, P. Levai, I. Vitev, Phys. Rev. Lett. 85 (2000) 5535.

[40] M. Gyulassy, P. Levai, I. Vitev, Nucl. Phys. B594 (2001) 371.

[41] A. Kovner, U. A. Wiedemann, hep-ph/0304151 (2003).

[42] M. Gyulassy, I. Vitev, X.-N. Wang, B.-W. Zhang, nucl-th/0302077 (2003).

[43] K. Adcox, et al., Phys. Rev. Lett. 88 (2002) 022301.

[44] K. Adcox, et al., Phys. Lett. B561 (2003) 82.

[45] C. Adler, et al., Phys. Rev. Lett. 89 (2002) 202301.

[46] S. S. Adler, et al., Phys. Rev. Lett. 91 (2003) 072301.

[47] S. S. Adler, et al., Phys. Rev. C69 (2004) 034910.

[48] J. Adams, et al., Phys. Rev. Lett. 91 (2003) 172302.

[49] B. B. Back, et al., Phys. Lett. B578 (2004) 297.

[50] M. Gyulassy, M. Plumer, M. Thoma, X. N. Wang, Nucl. Phys. A538 (1992) 37c.

[51] E. Wang, X.-N. Wang, Phys. Rev. Lett. 89 (2002) 162301.

[52] I. Vitev, M. Gyulassy, Phys. Rev. Lett. 89 (2002) 252301.

[53] S. S. Adler, et al., Phys. Rev. Lett. 91 (2003) 072303.

[54] I. Arsene, et al., Phys. Rev. Lett. 91 (2003) 072305.

[55] B. B. Back, et al., Phys. Rev. Lett. 91 (2003) 072302.

[56] J. Adams, et al., Phys. Rev. Lett. 91 (2003) 072304.

[57] R. Baier, D. Schiff, B. G. Zakharov, Ann. Rev. Nucl. Part. Sci. 50 (2000) 37.

[58] M. Gyulassy, P. Levai, I. Vitev, Nucl. Phys. B571 (2000) 197.

[59] P. Levai, et al., Nucl. Phys. A698 (2002) 631.

[60] I. Vitev, M. Gyulassy, P. Levai, hep-ph/0109198 (2001).

[61] M. Gyulassy, I. Vitev, X.-N. Wang, P. Huovinen, Phys. Lett. B526 (2002) 301.

[62] C. Adler, et al., Phys. Rev. Lett. 90 (2003) 032301.

[63] C. Adler, et al., Phys. Rev. Lett. 90 (2003) 082302.

[64] J. Rak, J. Phys. G30 (2004) S1309.

[65] M. Chiu, Nucl. Phys. A715 (2003) 761.

[66] *Dihadron azimuthal correlations in Au+Au collisions at* $\sqrt{s_{NN}}$ *= 200 GeV* **arXiv:0801.4545**

[67] C. Adler et al., Phys. Rev. Lett. 90 032301 (2003); C. Adler et al., Phys. Rev. Lett. 90, 082302 (2003).

[68] V. Greco et al., Phys. Rev. Lett. 90, 202302 (2003) and Phys. Rev. C68, 034904 (2003).

[69] R. C. Hwa and C.B. Yang, Phys. Rev. C70 024905 (2004), and J. Phys G30 (2004) S1117-S1120.

[70] R. Fries et al., nucl-th/0407102 (2004).

[71] A. Majumder, E. Wang, X. N. Wang, nucl-th/0412061 (2004).

[72] N. Armesto, C. Salgado, U. A. Wiedemann, Phys. Rev. Lett. 93 242301 (2004)

[73] J. Casalderrey-Solana, E. V. Shuryak, D. Teaney, hep-ph/0411315 (2004).

[74] H Stöcker, Nucl. Phys. A750 121 (2005).

[75] J. Ruppert and B. Muller, hep-ph/0503158 (2005).

[76] Banner M et al. 1982 Phys. Lett. B118, 203-210

[77] G. J. Alner, et al., Phys. Lett. B160 (1985) 193.

[78] *Transverse momentum and centrality dependence of dihadron correlations in Au+Au collisions at* $\sqrt{s_{NN}}$ *= 200 GeV: Jet-quenching and the response of partonic matter* **Phys. Rev. C77, 011901 , 2008-01-07**

[79] Jia, J. J. Phys. **G31** (2005) S521-S532

[80] Adams, J. *et al.* (STAR collaboration) nucl-ex/0411003

[81] **PHENIX Collaboration,** A. Adare *et al.* **nucl-ex/0608033**, *Scaling properties of azimuthal anisotropy in Au+Au and Cu+Cu collisions at* $\sqrt{s_{NN}}$ *= 200 GeV/c*

[82] nucl-ex/0311007

[83] S. S. Adler *et al. Phys. Rev. Lett.* **97**, 052301 (2006)

[84] Field, R. D. and Feynman, R. P. Phys. Rev. **D15** (1977) 2590-2616

[85] Feynman, R. P., Field, R. D., and Fox, G. C. Nucl. Phys. **B128** (1977) 1

[86] Feynman, R. P., Field, R. D., and Fox, G. C. Phys. Rev. **D18** (1978) 3320

[87] *Jet Structure from dihadron correlations in d+Au collisions at* $\sqrt{s_{NN}}$ *=200 GeV* **Phys. Rev. C 73, 054903 (2006), 2006-01-26**

[88] Della Negra, M. *et al.* (CCHK collaboration) Nucl. Phys. **B127** (1977) 1

[89] The complete volume Edited by M. Harrison, T. Ludlam and S. Ozaki, Volume 499, Issues 2-3, Pages 235-880 (1 March 2003) The Relativistic Heavy Ion Collider Project: RHIC and its Detectors

[90] D. Morrison "Number of binary collisions and total cross section in d+Au at $sqrts_{NN}$ = 200,GeV", PHENIX analysis note 165

[91] *"Jet Properties from Di-Hadron Correlations in p+p Collisions at* $\sqrt{s}$ *= 200 GeV"* **Phys. Rev. D 74, 072002 (2006), 2006-10-05**

[92] QM06 proceedings, Journal of Physics G: Nuclear and Particle Physics, volume 34, issue 8

[93] K. Adcox et al., Nucl. Phys. A757, 184 (2005).

[94] I. Arsene et al., Nucl. Phys. A757, 1(2005).

[95] B. B. Back et al., Nucl. Phys. A757, 28 (2005).

[96] J. Adams et al., Nucl. Phys. A757, 102 (2005).

[97] K. Adcox et al., Phys. Rev. Lett. 88, 19203 (2002).

[98] S. S. Adler et al., Phys. Rev. Lett. 96, 032301 (2006).

[99] U.A. Wiedemann, Nucl. Phys. B 588, 303 (2000)

[100] M. Gyulassy et al., Nucl. Phys. B594, 371 (2001)

[101] K. Adcox et al., Phys. Rev. Lett. 88, 022301 (2002).

[102] S. S. Adler et al., Phys. Rev. Lett. 91, 072301 (2003).

[103] S. S. Adler et al., Phys. Rev. Lett. 94, 232301 (2005).

[104] Y. Akiba (for PHENIX), nucl-ex/0510008 (2005)

[105] Yuri L. Dokshitzer, D.E. Kharzeev Phys.Lett.B519:199-206 (2001)

[106] M. Djordjevic and M. Gyulassy, Phys. Rev. C68, 034914 (2003)

[107] M. Djordjevic and M. Gyulassy, Phys. Lett. B.560, 37 (2003)

[108] B. H. Zhang, E. Wang, X-N. Wang, Phys. Rev. Lett 93, 072301 (2004)

[109] S. S. Adler et al., Phys. Rev. Lett. 96, 032301 (2006).

[110] S. Butsyk (for PHENIX), nucl-ex/0510010 (2005).

[111] N. Armestron et al., Phys. Rev D71, 054027 (2005).

[112] M. Djordjevic et al., Phys. Lett. B632, 81 (2006).

[113] B.Z. Kopeliovich and A.V. Tarasov, Nucl. Phys. A710, 180 (2002); J. Raufeisen private communication.

[114] S. S. Adler et al., nucl-ex/0507004 (2005).

[115] "Formation of dense partonic matter in relativistic nucleus-nucleus collisions at RHIC: Experimental evaluation by the PHENIX Collaboration" PHENIX QGP white paper, Nuclear Physics A Volume 757, Issues 1-2 , 8 August 2005, Pages 184-283, 2005-05-24